ANALYSIS, DESIGN AND TEST OF A JET VANE BASED THRUST VECTOR CONTROL FOR TACTICAL MISSILES

A THESIS SUBMITTED TO
THE GRADUATE SCHOOL OF NATURAL AND APPLIED SCIENCES
OF
MIDDLE EAST TECHNICAL UNIVERSITY

BY

OĞUZ EREN

IN PARTIAL FULFILLMENT OF THE REQUIREMENTS
FOR
THE DEGREE OFMASTER OF SCIENCE
IN
AEROSPACE ENGINEERING

NOVEMBER 2017

Approval of the thesis:

ANALYSIS, DESIGN AND TEST OF A JET VANE BASED THRUST VECTOR CONTROL FOR TACTICAL MISSILES

submitted by **OĞUZ EREN** in partial fulfillment of the requirements for the degree of **Master of Science in Aerospace Engineering Department, Middle East Technical University** by,

Prof. Dr. Gülbin Dural Ünver
Dean, Graduate School of **Natural and Applied Sciences** _____

Prof. Dr. Ozan Tekinalp
Head of Department, **Aerospace Engineering** _____

Assoc. Prof. Dr. Sinan EYİ
Supervisor, **Aerospace Engineering Dept., METU** _____

Examining Committee Members:

Assoc. Prof. Dr. Utku KÂNOĞLU
Aerospace Engineering Dept., METU _____

Assoc. Prof. Dr. Sinan EYİ
Aerospace Engineering Dept., METU _____

Assoc. Prof. Dr. Ercan GÜRSES
Aerospace Engineering Dept., METU _____

Asst. Prof. Dr. Ali Türker KUTAY
Aerospace Engineering Dept., METU _____

Asst. Prof. Dr. Sıtkı USLU
Mechanical Engineering Dept., TOBB ETU _____

Date: 13.11.2017

I hereby declare that all information in this document has been obtained and presented in accordance with academic rules and ethical conduct. I also declare that, as required by these rules and conduct, I have fully cited and referenced all material and results that are not original to this work.

Name, Last name: Oğuz EREN

Signature :

ABSTRACT

ANALYSIS, DESIGN AND TEST OF A JET VANE BASED THRUST VECTOR CONTROL FOR TACTICAL MISSILES

EREN, Oğuz

M. S., Department of Aerospace Engineering

Supervisor: Assoc. Prof. Dr. Sinan EYİ

November 2017, 136 pages

In this thesis, a design effort for a jet vane based Thrust Vector Control (TVC) in the scope of mechanical design, computational analysis and validating test process is executed to be able to find an optimum CFD approach to this kind of work. To do that, a preliminary design phase is initiated with an already optimized geometry which provides an aerodynamic surface to be worked on. After mechanical design approach to the geometry with system requirements, some of the unverified aspects of the design are tested such as validating the materials and assembly connections. From the conclusive design, testing phase of TVC on multi-axis test stand has carried out. For this matter, design criteria of such test stand, calibration procedure, validation and corrective factors for measuring such as alignment, noise filtering has been investigated and conducted. A computational analysis survey has been performed that consisting couple CFD variable parameters which they are mesh dependency and turbulence models. According to collected data, the optimum CFD approach is determined by the error amount between them. As a result, a comparison of the experimental and computational data has been examined to find the loose ends and area of improvements for increasing the accuracy of data.

Key-words: Jet Vane based TVC, CFD Analysis, Mesh Dependency, Turbulence Models,Multi-axis Test Stand, Test Stand Calibration, Signal Processing

ÖZ

TAKTİK FÜZELER İÇİN JET KANADI BAZLI İTKİ VEKTÖR KONTOLÜNÜN ANALİZİ, TASARIMI VE TESTİ

EREN, Oğuz
Yüksek Lisans, Havacılık ve Uzay Mühendisliği Bölümü
Tez Yöneticisi: Doç. Dr. Sinan Eyi
Kasım 2017, 136 sayfa

Bu tez kapsamında taktik füzeler için jet kanadı bazlı itki vektör kontrolünün bir tasarım çalışması, mekanik tasarım, hesaplamalı akışkanlar dinamiği (HAD) analizleri ve test ile doğrulanması çerçevesinde yapılmış olup; daha sonra gerçekleştirilecek çalışmalar için uygun bir analiz modelinin belirlenmesi amaçlanmıştır. Bu amaçla önceden eniyilenmiş bir aerodinamik geometrinin mekanik tasarımının sistem gereksinimleri ile beraber, önceden kestirilemeyen özelliklerinin (malzeme seçimi, bağlantı arayüzleri v.b.) test edilmesi ile yapılışı anlatılmaktadır.Buradan çıkan nihai tasarım, çok eksenli itki ölçüm sistemi ile performans ölçümüne tabi tutulmuştur. Bu amaçla bu tip bir test standında ölçüm yapımını etkileyen tasarım, kalibrasyon, doğrulama ve düzeltici faktörler (hizalama, sinyal işleme v.b) gibi özellikleri incelenmiş ve uygulanmıştır. Buna ek olarak bir HAD analiz süreci, çözüm ağı ve türbülans modeline göre incelenerek en uygun modelin bulunması hedeflenmiştir. Bu amaçla çözümlerin uygulanabilirliğine, toplanan data ile ne kadar farklılaştığına bakılarak karar verilmiştir. Sonuç olarak deneysel ve hesaplamalı yöntemler karşılaştırılarak süreç içerisinde bulunan eksik ve hatalar daha doğru bir sonuç için değerlendirilmiştir.

Anahtar Kelimeler: Jet Kanadı bazlı İtki Vektör Kontrolü, HAD Analizi, Çözüm Ağı Bağımlılığı, Türbülans Modelleri, Çok Eksenli İtki Ölçüm Sistemi, Test Standı Kalibrasyonu, Sinyal İşleme

At long last…

ACKNOWLEDGMENT

I would like to express my gratitude to Assoc. Prof. Sinan EYİ for his great help to my work. I also would like to state that this study can not be accomplished without the support and guidance of my colleagues, Mr. Yusuf ATA, Mr. Halil Ünay, Mr. Onur Ozan KALKAN, Mr. Can ÇITAK and Mr. Mustafa AKDEMİR. I thank them all. I especially thank to my friends, Mr. Coşku ÇATORİ, Mr. Burak ÖZKAHYA, Ms. Ezgi ERDAL, Mr. Burak KIZILKAYA, Mr. Eren DOĞAN, Ms. Lütfiye ÇAĞAN and Mr. Tuğrul AKPOLAT for always being there for me and for giving me a life full of beautiful moments and happiness.

Above all, I would like to offer the most and my sincere gratitude to my family as for sure I can not come this far in this journey without them.

TABLE OF CONTENTS

LIST OF TABLES

LIST OF FIGURES

LIST OF SYMBOLS

τ : Shear stress on cross section area

F : Shear force applied on cross section area

d : Diameter of the cross section area

C_x : Calibration load cell on x-axis

C_y : Calibration load cell on y-axis

C_z : Calibration load cell on z-axis

M_x : Measuring load cell on x-axis

M_y : Measuring load cell on y-axis

M_z : Measuring load cell on z-axis

R_x : Reaction force on x-axis

R_y : Reaction force on y-axis

R_z : Reaction force on z-axis

C_{x_c} : Calibration force on x-axis (compression state)

C_{y_c} : Calibration force on y-axis (compression state)

C_{y_t} : Calibration force on y-axis (tension state)

C_{z_c} : Calibration force on z-axis (compression state)

C_{z_t} : Calibration force on z-axis (tension state)

R_{xx} : Reaction force on x-axis in x-axis calibration

R_{xy} : Reaction force on y-axis in x-axis calibration

R_{xz} : Reaction force on z-axis in x-axis calibration

R_{l_m} : Reaction force error on side axes due to moment

a : Upper or lower boundary of correlation steps regarding to previous firings

e_{lt} : Moment arm due to laser tracker measurement error

b : Moment arm to y-axis or z-axis

$R_{l_{fx}}$: Reaction force error on x-axis due to force misalignment

$R_{l_{fy}}$: Reaction force error on y-axis due to force misalignment

$R_{l_{fz}}$: Reaction force error onz-axis due to force misalignment

L : Length of data array

F_s : Sampling frequency

AS : Amplitude Spectrum

CHAPTER 1

INTRODUCTION

1.1 Objective of the Thesis

The aim of this study is examining jet vane based Thrust Vector Control (TVC) design by experimental and computational analysis in order to validate initially optimized geometry via captive firing test and determine the optimum CFD approach prior to a mechanical design task for such component.

An optimized geometry by weight which forms the aerodynamic surfaces has been selected for this study which leads to a starting point of mechanical design phase of the task that will be covered in following chapter. Mechanically designed and manufactured model shall be tested on a stand that is constructed especially for it and the readings of lift generated by the TVC shall be compared with the CFD analysis. This study also covers the aspects of test stand to ensure the validity of test efforts.

1.2 Thrust Vector Control on Tactical Missiles

TVC is a way of missile orientation adjustment in 3-dimensional space that uses the generated nozzle flow which enables a considerable improvement on flying capabilities of the air vehicle. Various TVC methods have been in service for decades, the earliest example dates back to WWII era V-2 strategic missiles where the aim is to achieve the guided flight trajectory with a jet vane based TVC.

Regardless of the type of TVC application, the technique conducts a moment variation around center of gravity of the air vehicle where TVC is deflecting the primary thrust

vector from the vehicle's centerline. An example of flexible joint method which is used in both solid propellant rockets and fighter jet aircrafts is given to provide the idea behind the TVC approach in Figure 1.1. As it is shown, diverting the nozzle centerline generates deflected thrust vector direction which creates an angle between nozzle and missile centerline. Moment arm and missile thrust then provide the turn needed for the desired trajectory. As it is similar to aircraft tail, the maximum distance between the TVC point and center of gravity ensures smaller deflection on nozzle which will ease the design of a dynamic action in an extremely conditioned environment.

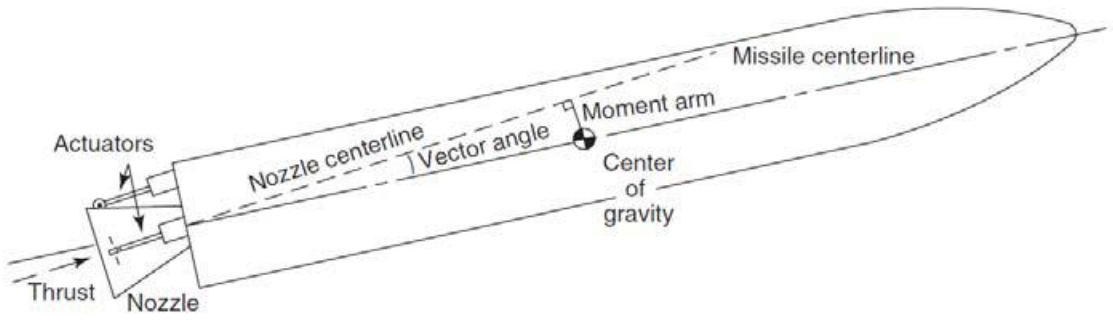

Figure 1.1: Working principle of TVC [Mark, 2003]

Classification of TVC as shown in Figure 1.2 can be summed up based on nozzle applications as moveable nozzle, fixed nozzle and reaction nozzle where generally moveable and fixed nozzle types are in use. These types are either directly diverting the plume or diverting it by a mechanical interference where a jet vane based TVC can be placed. Its most important role on determining which type of TVC should be applicable is the simplicity of the mechanisms that should be work under high temperature. Jet vane based TVC applied on various platforms such as anti-tank missiles, air defense missiles, anti-submarine missiles even on a space launch vehicle due to this matter.

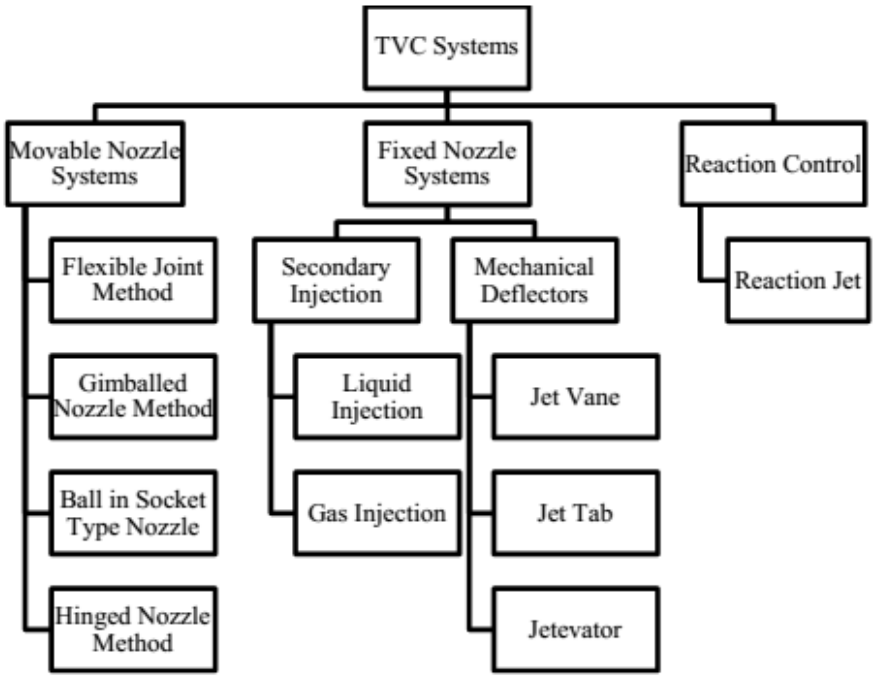

Figure 1.2: TVC applications with respect to nozzle types [Çelik, 2014]

TVC based on jet vanes is highly effective and easily adapted solution for an air defense missile as it aims to find and eliminate even low altitude and rapid inbound missiles. Jet vane based TVC is quite efficient way to maneuver at subsonic speed during initial launch sequence since the force generated by TVC provides enough moment around the center of gravity and this force is enough to make a vertical launched missile turn to even horizontal trajectory. This phenomenon is a successful outcome for being free of positioning the missile launch vehicle to the direction of incoming target as this action contains substantial time penalties [Facciano et al., 2002]. Figure 1.3 shows an example of countermeasure missile deployment against targets and expresses the importance of response time. Regardless of the launch platform, the flight trajectory with absence of TVC demonstrates altitude gaining response to threat whilst a 3 axis TVC is a better solution for a low altitude cruise missile where the system capable of pitch, roll and yaw motions. Because of this fact, a 3 axis TVC based on jet vanes is examined for this study

since almost all aspects of the system can be either computed or experimented and it can be easily manufactured, a clear indication of a quick rise on technological readiness level. It has to be stated that the reduced effectiveness of jet vanes when flight mach number increases and the complete ineffectiveness of them after engine burnout are the greatest disadvantage of jet vane based TVC configuration. [Riddle, 2007] Despite the disadvantage, packaging and cost of this configuration makes it a valuable solution for TVC.

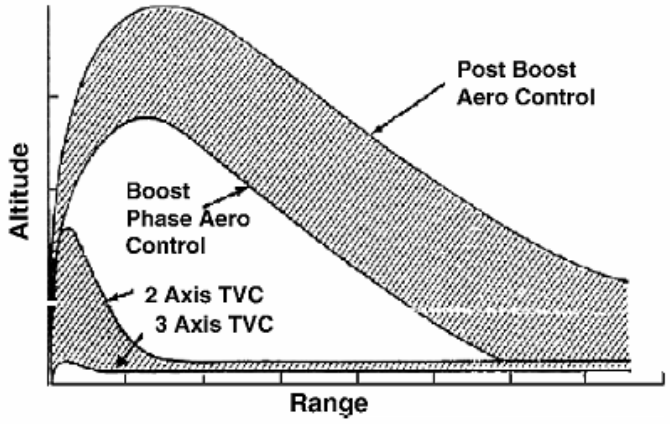

Figure 1.3:Vertical launch trajectories against low-altitude targets [Facciano et al., 2002]

An example and illustration of jet vane based TVC are shown in Figure 1.4(a) and Figure 1.4(b). The TVC assembly is formed by an aerodynamic surface, an insulation component and a shaft in basic. The aerodynamic surface is the geometrical interface with the nozzle plume which will divert the exiting flow. This will lead to creation of pressure side and suction side as it will be on an aircraft wing. The pressure difference between two sides will generate lift which is going to change the direction of flight. In Figure 1.4(b), the horizontal jet vanes positioned with a negative AoA, that means the lift is on negative direction which creates a pitch moment for missile. Behind or surrounding the jet vane, there shall be an insulation material which will mitigate the heat transfer onto cascade of the missile. The position and shape of insulation material is generally determined by the dimensions and life cycle of the missile. The shaft is the

mounting interface between the aerodynamic surface and the cascade to be coupled with the transmission arm which is commanded by missile control system.

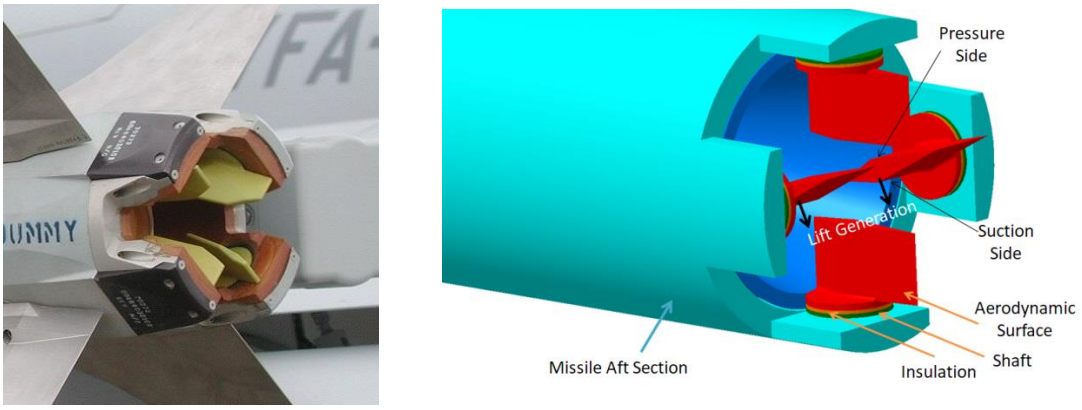

(a) (b)

Figure 1.4: (a) Jet vane based TVC on AIM 9X AAM
(b) Illustration of jet vane based TVC

Further information about the physics on thrust generation and TVC phenomenon, also their related area of utilizations can be found in reference section [Schaefermeyer, 2011][Babu and Prasad, 2012][Simmons, 2000].

1.3 Experimental Design for Jet Vane Based TVC

Forming a production model of a design requires both mechanical designing and testing approach to ensure the optimum outcome. In this study, a mechanical design process on a beforehand optimized aerodynamic geometry shall be conducted with respect to system requirements such as weight, generated lift, packaging, assembly error margin as well as possibility of transformation to end product according to the cost and availability of materials. Although each design aspects are carefully selected, testing phase can bring up some unforeseen problems on a preliminary design therefore this study is aimed to show an approach to find a valid candidate design prior to test phase via mechanical design and experimental design optimization.

To experiment on TVC system requires 3-dimensional measurement tool as the system generates forces on 3 axes or their product or their moments. As driven by the requirements, the testing instrument (i.e. test stand) shall be formed in order to measure lift of jet vane based TVC for this study since an engine coupled TVC test is an expensive combination to examine a missile system. Figure 1.5 represents an example of thrust stand in CE-22 Advanced Nozzle Test Facility which aims to determine the characteristic of thrust vectoring with flexible nozzle geometry. To create such a test stand, a design, calibration and validation approach shall be carefully selected and these are explained in the following chapter. Additionally, a data reduction process of measurements will be covered in order to compare with computational analysis results.

Figure 1.5: Six-component thrust stand in NASA Test Facility [Wong, 2003]

1.4 CFD Analysis Coupled with Turbulence Models

It is a known fact that, test is an expensive option compared to performing CFD analysis and it is so desired that a design shall be close to its final form via CFD approach to prevent further tests. For this study, extensive CFD analysis with different turbulence models have been performed for the sake of validation and reduce recent cost and future

costs of designing new thrust vectoring system while optimizing the current design regarding aerodynamic parameters as well as the mechanical ones.

Different turbulence models and varying numbers of mesh have been utilized to obtain the maximum accuracy. All of the results have been compared in terms of accuracy and required CPU time, following that, a trade-off has been performed for best possible accuracy with the least amount of time and results have been shared at the following sections.

Advantage of having validated CFD results, dramatically affects the future work that will be based on this study and leads the way to build a virtual database of new designs and utilization of optimization algorithms which is the state of art approach in the industry.

CHAPTER 2

DESIGN AND EXPERIMENTAL PHASE

2.1 Mechanical Design of TVC

Mechanical design process will be started with a reference design, which it is called an optimized aerodynamic geometry for this study. In order to get this optimized geometry a computational design process of a jet vane based TVC is conducted to be able to acquire the least weight and meet the predetermined criteria on lift and drag. This initial optimization where there is a CFD study is not considered in the scope of this study, where it solely defines the approach to shape a mechanical design constructed upon the optimized geometry. To be able to execute it, all mechanical and heat load constraints, additionally physical limitations will be covered over this design. Next section will explain the preliminary approach to the task.

2.1.1 Preliminary Design Process

CFD analysis for optimized geometry provided the basic dimensions of the aerodynamic surface and its position on the aft section of the missile. The analysis outputs demonstrated a symmetric diamond and trapezoid shape which is already expected as minimum drag generating one. A general view of aerodynamic surface is given on Figure 2.1.

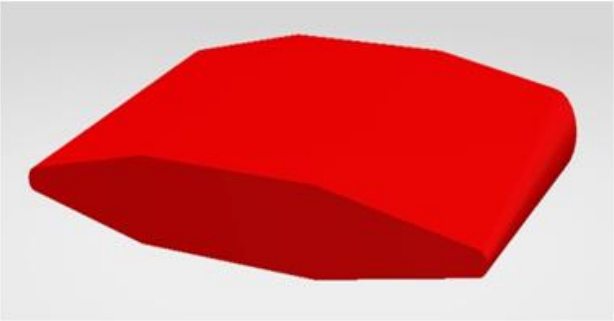

Figure 2.1: Aerodynamic geometry of jet vane based TVC

The main issue in this mechanical design process is to design a mechanical interface between the aerodynamic surface and transmission arm which is transferring the inputs to TVC while nozzle plume has a temperature over 2000 K. Moreover, TVC is obligated to mitigate the conduction heat transfer to transmission arm where there is a delicate bearing on mounting interface of the missile. An illustration of the initial concept is shown in Figure 2.2 in order to express the components in this environment such as jet vane (aerodynamic geometry), base, insulation, and shaft.

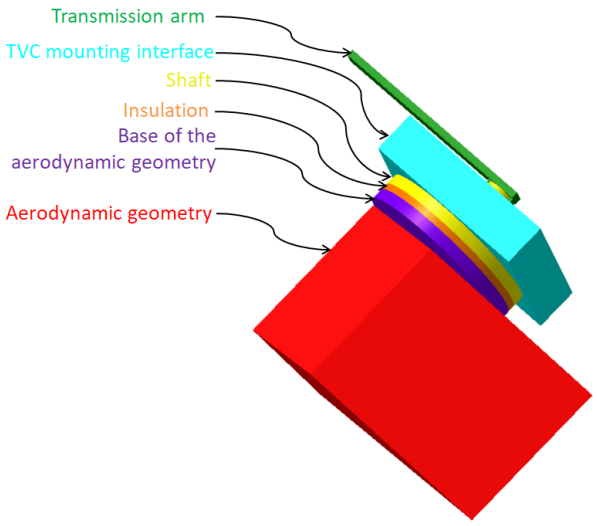

Figure 2.2: The components of the TVC and elements of the mechanism

2.1.1.1 Components based evaluation of TVC

In this section, the TVC components are investigated for mechanical design according to forced requirements and foreseen conditions that can pose problems on assembly.

- **Jet Vane (Aerodynamic geometry)**

Jet vanes are the components that are immersed into the plume which means there is a selection of material about either that should be a durable one or an erosive one. The most beneficial feature of an erodible jet vane is the reduced drag over time in missile life cycle. Since there are tail fins on tactical missiles that are the main control surface after launch sequence, the significant force amount is generated by them. Therefore the jet vane effective operating duration is less than 10% of the life cycle. This clearly indicates that carrying the obsolete assembly just causes reduced thrust of missile. A reduced thrust has a great impact on range of tactical system, thus it should be the first thing to consider on earlier design phase. Allowable drag force that is proportional to missile thrust is always a parameter and a strict requirement for designer. For this study, the downside of drag force is overcome by the propellant design and since an erodible jet vane requires enormous amount of static firing test in order to prove that it can generate required lift. The material that can be used as ablative design concept can be reinforced carbon-carbon / carbon fiber-reinforced carbon however; it has poor mechanical strength over a temperature of 1000 K. This aspect will also present a mechanical design problem that will also require captive tests in great number to find a solution. Conclusively, the safer way to seek a solution is to get a durable material for the task.

A durable material that can be used as jet vane is considered to be made of refractory metals. These materials or their alloys express high service temperature, great creep resistance and they have applications as being nozzle material for air and space vehicle therefore, this makes these metals ideal candidate for a jet vane. Since the reference

point is to choose the least ablative material for this design, two alternatives came up and they are going to be stated as refractory metal 1 and refractory metal 2 due to privacy concerns. These two materials are put on a comparison test with 6” test engine to investigate the amount of ablation. The test engine is often used for propellant characterization analysis by checking the thrust and combustion pressure levels of sampled propellant in captive firing. A controlled experiment that contains series of identical test engines and two candidate materials is conducted and it is found that first alternative has 7.8% less surface ablation, therefore it is selected as jet vane material.

A pre-requisite condition is defined as a boundary for mechanical design process which states the zero AoA of TVC has to be known prior to full assembly of missile. This requirement caused by the single actuator concept for tail fins and jet vanes which they are connected by a transmission arm in order to control them together. To zero in the TVC assembly with tail fin, aerodynamic geometry has to be assembled in the last step and the adjacent part should contain the zero marks. It is done so, because the aerodynamic surface does not have a plain surface to get measurements and non-availability of a laser tracker in hand. As a result, a mating interface between the jet vane and adjacent part (it is called base of aerodynamic surface) has been designed. The interface on the jet vane is shown in Figure 2.3. The shape of the interface is like so created that the thickest area will mate with the base and less thick area will let the material elongation to ensure component integrity.

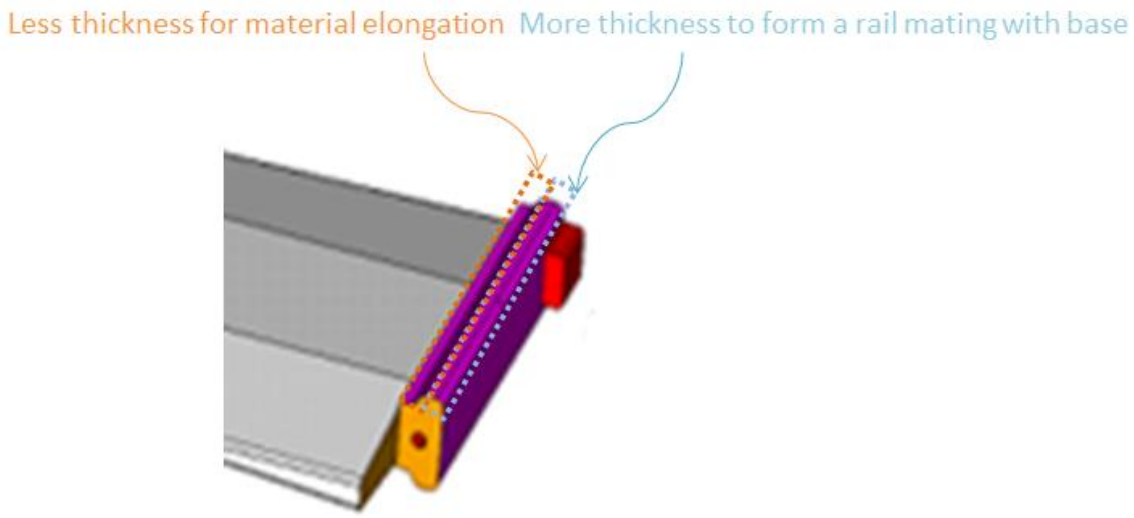

Figure 2.3: Interface between aerodynamic surface and base

- **Base of the aerodynamic geometry**

The base of jet vane is aimed to be anchorage geometry basically while holding the jet vane in position and holding the rest of components together. Additionally, this component will be faced the nozzle exhaust as there is flow expansion onto it. Therefore, it will act as a heat shield for the assembly. The refractory metal 2 is an ideal material to execute these two combined task.

- **Insulation**

Insulation is required in this assembly because of the bearings on TVC mounting interface on the rear section of missile. The bearings have specific operational temperature and they are in contact with the shaft extension radially. To ensure not to exceed desired temperature on bearings has to be satisfied with mitigating the conduction heat transfer from the base to the shaft. The insulation is considered to be made of polymer based material which is already in use on nozzle insulation applications.

❖ **Shaft**

The shaft is primarily used because of the limited bearings temperature. In fact, geometry in one piece includes aerodynamic surface, base and shaft combination can form a TVC assembly however; requirement of maximum temperature falls base and shaft apart and places insulation in between. Since the insulation is used on assembly for conduction heat transfer and convection heat transfer onto shaft is at minimum, a steel alloy can be employed. The steel alloy is also reinforced by heat treatment to increase its strength over higher temperatures to a maximum 1200 MPa UTS. As it is already known that the increased strength by heat treatment will present better material behavior under elevated temperature. That is a beneficial outcome if the convective heat transfer rate is greater than assumed as it can cause failure of connection bolts before the heat energy reaches the bearings.

❖ **Connection bolts**

Up to this point, the crucial components that form an assembly, an aerodynamic surface for generating lift, a heat shield for mitigating convection heat, insulation for mitigating conduction heat and a shaft for assembly interface are explained. The final component is the connection bolt to hold these elements in place together. The diameter of cylindrical components (base, insulation and shaft) is less than 70 mm, therefore it is problematic to fit the bolts in limited area as shown in Figure 2.4. A careful design procedure has to be executed in order to determine the sizing and placement of the bolts.

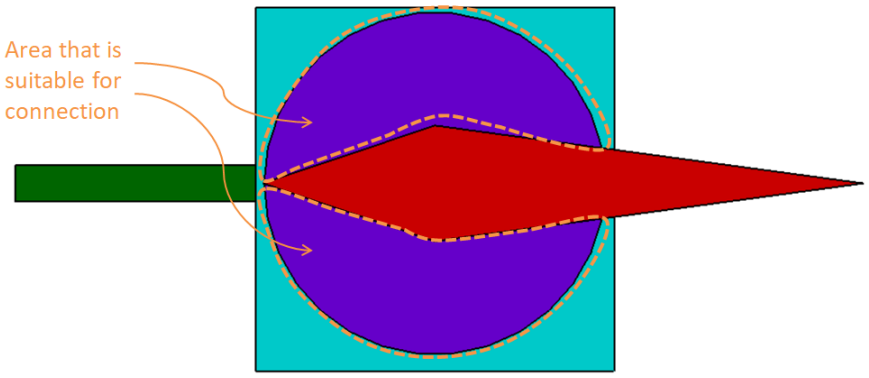

Figure 2.4: Bolt Connection Area on TVC

At first, a minimum number of bolts that required holding loaded assembly have to be determined. On this matter, the critical load onto the bolts will be shear stress which depends on the yield strength. It is obvious that lift is acting as shear force onto bolts.

The total thickness of base, insulation and shaft is less than 15 mm where the bolts maximum length should be less than this value. A quick survey reveals that a regular socket head bolts with minimum available diameter has longer length, therefore a bolt that it has reduced head thickness has to be used. That specialized bolt can be found as 10.9 class in standard, thus the yield strength is predetermined.

From this point, minimum number of bolts shall be determined by shear stress and covered area. Eq. 2.1 indicates the formula that has been used to calculate shear stress on one bolt. [Budynas and Nisbett, 2005]

$$\tau = \frac{F}{\frac{\pi d^2}{4}} \tag{2.1}$$

Here, F is the shear force and d is the minimum minor diameter of the bolt. Since the class of the bolt indicates its yield strength as 900 MPa and assumed conservative lift load on aerodynamic geometry is 3000 N; the minimum required bolt diameter is M3

with at least 1.5 factor of safety. This provides a clear statement that the combined lift and heat load will define the minimum number of bolt on the design. The heat load is unpredictable at this moment thus; it is easier to quantify via static firing test.

Important thing that left to be considered is the determining the stiffness of the assembly since such a heated environment poses problem if the plume penetrates between the components. It is obvious that, bolts will directly heated under this condition where yield strength of the bolts wane dramatically. To be able to determine the number and placement of the bolts, fixed pressure cone methodology is applied. It is also the way of approach to find stiffness and stiffness coefficient of the joint which will point out the optimality of the connection design. [Brown et. al., 2008]

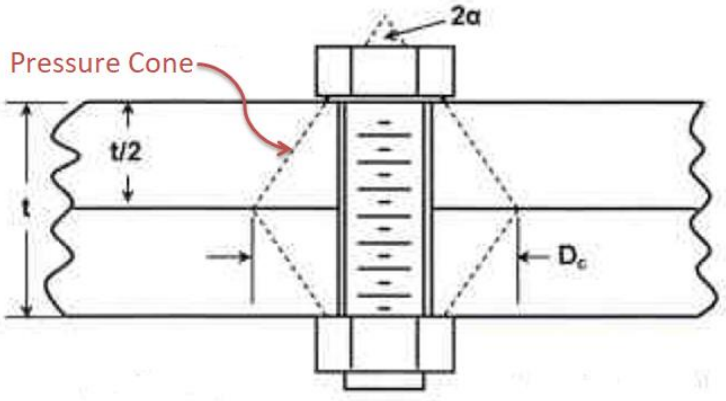

Figure 2.5: Pressure cone on bolt with nut joint [Archer, 2010]

In Figure 2.5, illustration of pressure cone on bolt with nut joint can be seen. Basically the clamped force of a joint is distributed to an area, not just under the bolt head. The diameter of the cone D_c is the maximum distance that the area can reach. If there is adjacent connection, it has to be such close to second one so that its cone diameter contacts with it. By doing so, it can be ensured that entire joint is clamped and displacement of joint surfaces is prevented. The cone is determined by two parameters; the length of joint, t and cone angle, α. The cone angle can be between 25° and 45°,

however the higher the value is greater overestimation of the area, it is suggested that it shall be 30° [Budynas and Nisbett, 2005]. With a certain cone angle, the cone is mirrored from a line which is the half distance of total grip length.

Before getting deep into the pressure cone for determining stiffness of the joint, validation of clamping area has to be conducted. For the TVC assembly, the assumption of bolt diameter and placement is made as it is easier to calculate and iterate the results by changing these two parameters on a code and CAD drawing. Assumed configuration is shown in Figure 2.6.

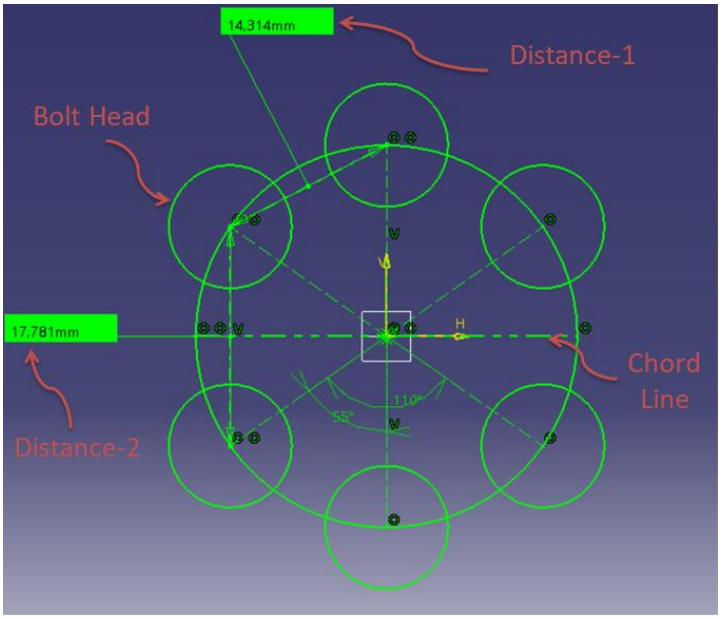

Figure 2.6: Assumed bolt configuration

The bolts are selected as to be M6, their head covering area is sketched. The bolt pattern diameter is also determined by considering the optimal distance from any feature around individual bolt. Chord line of the aerodynamic surface is also shown in Figure 2.6. The bolts on the same side with respect to chord line have an in-between angle of 55° and on the mirrored side, the angle is 70°. Distance-1 is the space between bolts' centerlines for 55° and distance-2 is the same with 70°. The total grip length is 13 mm, the members of

the grip are the base, insulation and shaft. By these parameters, the only unknown remaining is the diameter of the frustum under the bolt head. General approach indicates that the diameter shall be 50% more of the bolt diameter. The validation of distances can be computed by Eq. 2.2

$$\delta = 2x\left(\frac{t}{2\sqrt{3}} + \frac{d_w}{2}\right) - d_{ibb} \qquad for\ \alpha = 30° \tag{2.2}$$

In Eq. 2.2, t is the total grip length, d_w is the frustum diameter under bolt head and d_{ibb} is the distance in between bolts. From this perspective, the difference between cone diameter and distance in between provides the validation parameter δ which will be greater than zero in accordance with stated clamping force requirement. The cone diameter is calculated as 16.51 mm which is greater than distance-1 however less than distance-2. The second value is considered as good enough because the maximum joint displacement can be occurred while the TVC on maximum lift and the displacement will be observed around bolts with 55° angle. Additionally, the maximum joint displacement will be seen where that side of the assembly directly meets the incoming nozzle plume. The greater clamping safety is given to distance-1 because of these conditions in order to construct a proper joint.

The stiffness of the joint has same meaning with springs in serial connection. Each member of the joint has its own stiffness coefficient and overall stiffness is calculated via them. As it is obvious that the lowest stiffness coefficient is the determinative one for overall, in this case the insulation has the minimum elasticity module. Expressing the joint stiffness is a validation method of member thicknesses which is significant for achieving correct bolt connection configuration.

To apply the method, the pressure cone is divided into sections constituted by the thickness of the members. These sections are called frustum and there are at least three of them in this study's joint. The exact number is not provided to not reveal the actual

thicknesses, only the mathematical approach is given.

$$k = \frac{0.5774\,\pi\,E\,d}{\ln\left[\frac{(1.155\,h_f + D - d)\,(D+d)}{(1.155\,h_f + D + d)\,(D-d)}\right]} \qquad for\ \alpha = 30° \tag{2.3}$$

Here E is the elasticity module of the member, d is the bolt diameter, D is the frustum short diameter and h_f is the height of the frustum where the parameters are shown in Figure 2.7. The overall stiffness of the joint is given in Eq. 2.4 by the summation of inverses and stiffness of the bolt is provided in Eq. 2.5 by the cross section area, elasticity module and bolt length. Bolt stiffness is required for the joint stiffness coefficient, C; as it is an indication of the ratio about how much tensile force the bolt is capable of handling, its formula is presented in Eq. 2.6.

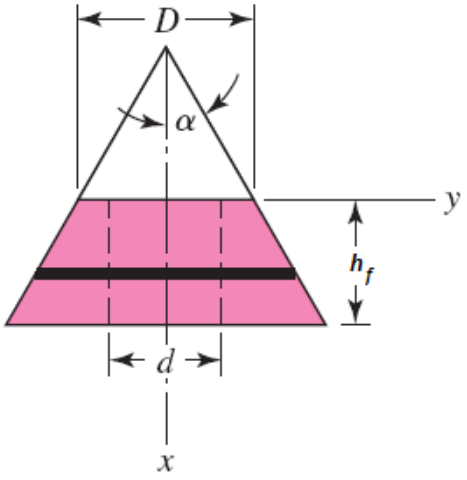

Figure 2.7: Frustum parameters

$$\frac{1}{k_m} = \frac{1}{k_1} + \frac{1}{k_2} + \frac{1}{k_3} + \cdots + \frac{1}{k_i} \tag{2.4}$$

$$k_b = \frac{A_b E_b}{L_b} \tag{2.5}$$

$$C = \frac{k_b}{k_b + k_m} \tag{2.6}$$

After parameters are put in place, joint stiffness coefficient C is found as 0.32 which is higher than recommended 0.2. This suggested value is for metal connections and since TVC joint has an insulation layer which is significantly less elasticity module, the resultant value is acceptable. This is also means 68% of the tensile force will be met by the joint which will help to keep the preloads on bolts. The displacement of the joint will be also ensured to be at minimum by keeping preload on. It is also previously found that the lift has little effect on shear stress, the amount of 6 metric bolts and presented placement is valid for preliminary design phase. The only consideration has to be the heat transfer which has substantial influences on each physical and mechanical parameter. It is not possible to calculate this effect by hand for such case, thus an experimental approach is needed which is going to be covered in the following section.

2.1.2 Preliminary Experiments on TVC

As it is stated in previous section, the unknown parameter is the heat transfer on preliminary design which can pose serious problems. To recall, two features are suspicious.

- The bolt heads are facing towards the nozzle plume where they will be directly heated. They are prone to a failure; however TVC failure may take place later than the required TVC operational duration in missile life cycle.
- Aerodynamic geometry and the base expose to extensive nozzle heat. It is undesirable but there is an interface between them which is formed as rail track mounting. The manufacturing tolerances shall be in optimum state where the elongation of components would not present a stress on each other. In such case, a definitive outcome of structural integrity failure will occur.

The first condition is the most unwanted one. Since the aerodynamic surface has non-ablative material, the main driving design aspect is to hold TVC until the end of mission cycle. The calibration of tail fins and TVC need to be done by a custom electronic device which will be used nearly end of the missile assembly. That means the missile has his solid propellant which can be ignited by static or fault current which is totally unacceptable. These two controversy matter shall be immediately tested in order to see there is a solution space to live in. Additionally, the rail mating interface should also be tested and verified. If the bolt connection can sustain, that feature can be examined. Figure 2.8 presents an actual image of TVC focusing on these two areas.

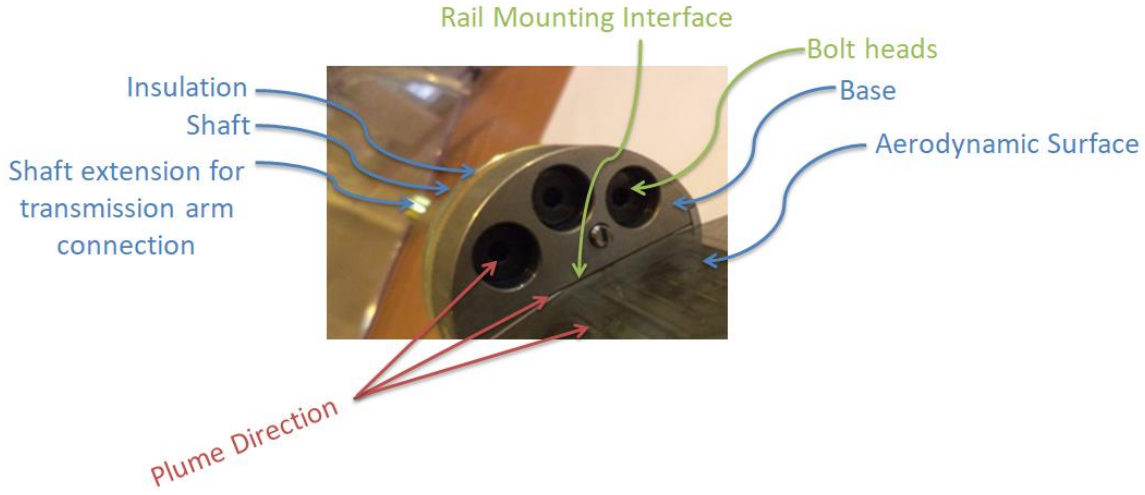

Figure 2.8: Image of assembled TVC

❖ **Investigation of bolt connections**

The preliminary design is tested for mechanical investigation purposes to check the bolt attachment position and the rail mounting interface right below them. To do so, a force balance instrument is coupled with a standard captive firing test stand. That is a simplified version of testing a TVC system because the TVC is positioned decoupled from the engine and is just mounted on the test stand. Observation of TVC-missile interactions is impossible because of this fact however force balance instrument creates

a 6 DoF measuring platform that is a viable option to investigate jet vane based TVC in earlier stages [Lauzon, 1990]. Possible failure can be cited by the decrease of bolt mechanical strength under high temperature as the yield strength at this temperature can not meet the shear force.

The bolt failure is indeed occurred during the initial phases of engine burning even before the proper collection of aerodynamic force data. The final shape of the TVC after failure can be seen in Figure 2.9. The bolts are clearly ripped apart due to this effect since the remaining parts of them can be clearly seen with the threads undamaged. The test helped to gain valuable information since the bolts amount and placement that has been chosen on previous section is valid. There is not any severe ablation on the insulation surface where it should be if there is plume penetration in between components. Small area on the insulation has been ripped off because the first bolt to break off is the lower aft one. The maximum moment arm to the pressure center of the aerodynamic force is on that bolt.

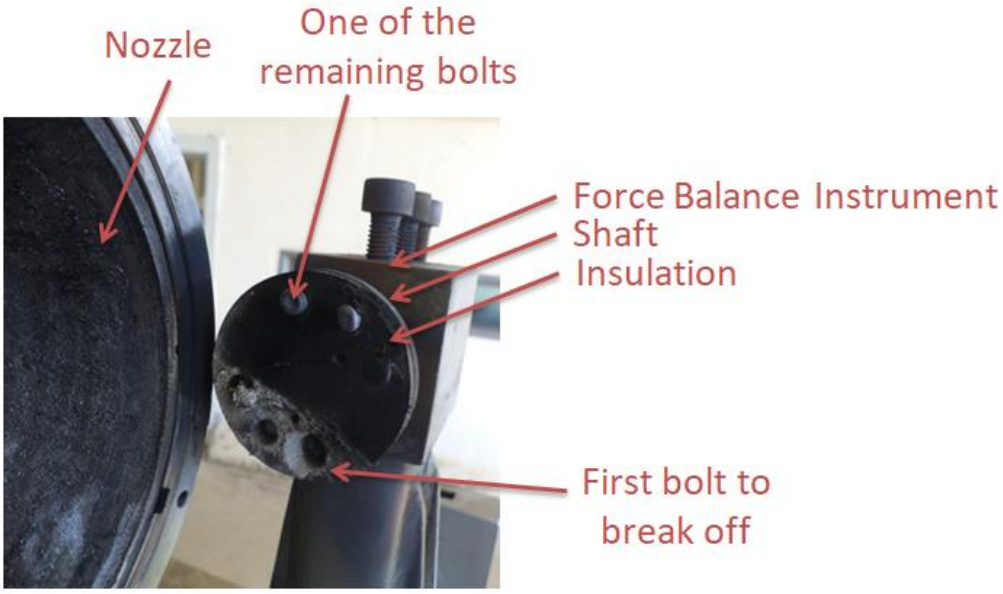

Figure 2.9: Integrity failure of the preliminary design

As it is described, the exposed bolt heads causes a failure; therefore the bolt heads are removed from the base component and they are put onto shaft. The direction of the bolts reversed, as head on the shaft and thread end on the base, so that an uninterrupted surface on the base is ensured. Additionally, temperature data gathering is planned for the next test as if there is another failure on any joints, CFD and thermo-mechanical analysis can be run in order to find the root cause.

- **Investigation of rail mating interface**

It is important to be said beforehand, modified TVC assembly is subjected to a full scale test configuration to examine the interface. Since the force balance instrument method includes only 1 instead of 4 TVC, it may alter the temperature readings; also lack of coupled connection can create the same outcome. Therefore, the test configuration is not the same with previous article so that the actual temperature can be found. The temperature data gathering is conducted on aerodynamic surface, on base and behind the insulation for all four TVC.

The rail mating interface has shown some inconsistency during these tests but before investigating the rail mating interface, there can be an important evidence for validation on bolt head replacement because the heads are close to that surface and if the temperature on that location has not increased too much during the test, it will prove the engineering judgment. Figure 2.10 shows the temperature distribution on shaft for a test that is configured as full scale. The shaft temperatures that are collected just behind the insulation clearly states a stable value is achieved during the first 10 seconds, staying below 50°C. This result presents the bolt connection adjustment will be work as designed beyond doubt. The TVC is tested repeatedly due to rail mating interface however, no further failure on bolts has been observed.

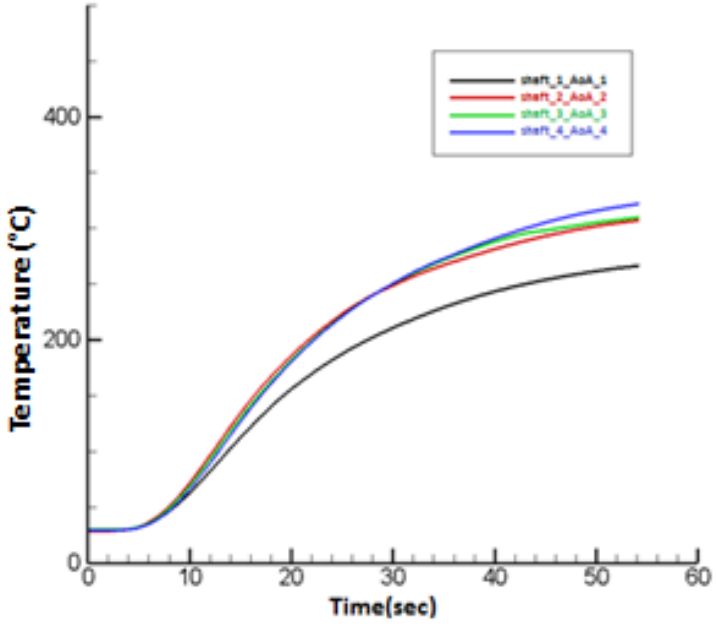

Figure 2.10: Temperature distributions for four shafts during test

The fact remains that, the mating interface has shown poor confidence on these test campaign. The aerodynamic surface is broken off from the TVC assembly arbitrarily, not at same moment in the test and not on the same position which indicates a problem caused by the material characteristics. The issue can be explained by a series of thermo-mechanical analysis and actual temperature readings.

It has to be stated that the CFD analysis in order to conduct mechanical analysis also varies because of the material itself. The refractory metals can not be easily modeled on CFD because their heat transfer mechanisms significantly deters. A study that dedicated to a refractory metal on this issue presents great temperature difference in its findings [Rainville et. al., 2004]. As it is same in this study, temperature distribution has risen up to 2800 K approximately which is not logical since the production of the material is conducted close to this temperature. Figure 2.11, Figure 2.12 and Figure 2.13 indicate

the temperature difference between the gathered and computed. There is more than 100% uncertainty.

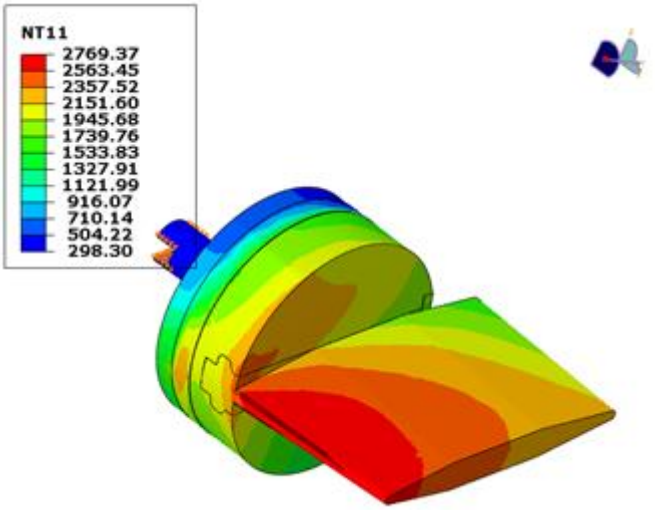

Figure 2.11: Temperature distribution in °K on TVC

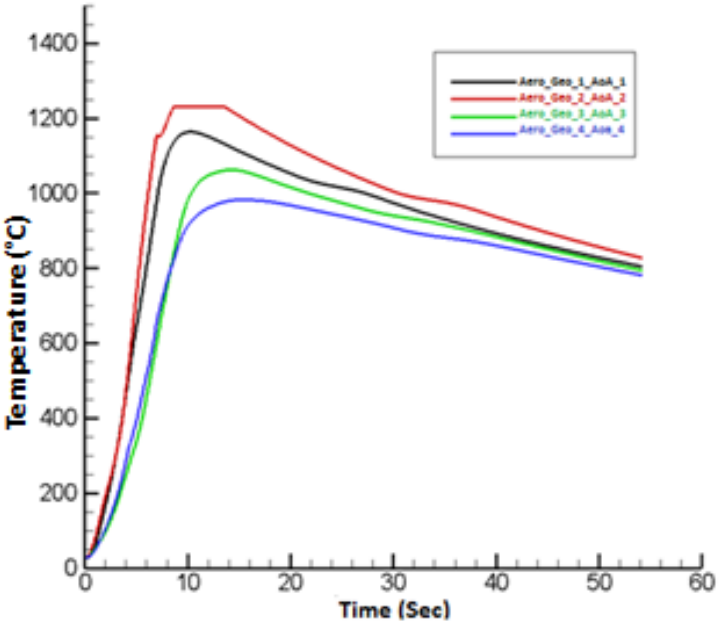

Figure 2.12: Temperature distributions for four aerodynamic geometries during test

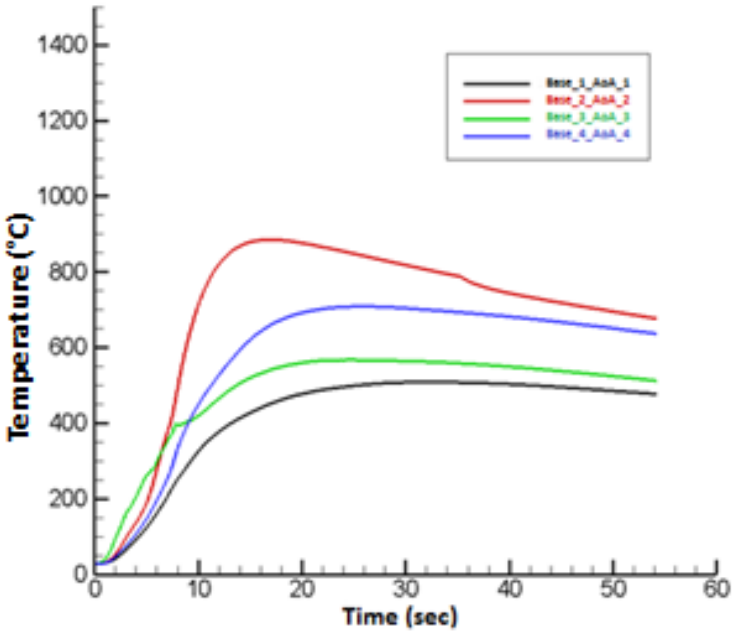

Figure 2.13: Temperature distributions for four bases during test

According to these facts, the proper way of accurate temperature distribution can be difficult to achieve. Different studies in literature show extensive works on heat transfer modeling with refractory metals [Yu et. al., 2004] [Harrisson et. al., 2003] [Nunn, 1988] [Dulke, 1987]. The main reason for unpredictable heat transfer is the surface ablation. Even though it is not substantial in this case, the materials that are used in this study are alloys and increased temperature presents physical changes on them; for instance vaporization of some ingredients in alloys because of the lower evaporation temperature comparing to others. This uncompleted ablation creates a change on composition of the material which expresses a lowered mechanical strength because the main purpose of the expelled ingredient is to decrease brittleness of the main ingredient. Since a case study is not trustworthy, a comparison can be made by omitting the rail mating interface out of the TVC design. It is obvious that, relieving the interface from the design definitely

improve the integrity of assembly, therefore it is considered. A thermo-mechanical analysis survey conducted due to these facts.

The analysis is executed by Abaqus 6.13-1 version which is finite element software. The software generally uses the Newton's method as computational technique to solve nonlinear equilibrium equations where this study requires the same approach. Basically, the algorithm uses discretization of the virtual work equation, trying to solve the output parameter conjugated to the force component in iterative way. This method is often used due to its convergence rate. The following Eq. 2.7 and Eq. 2.8 present the mathematical notation.

$$\int_{V^o} \beta_N : \tau^c \, dV^0 = \int_S N_N^T \cdot t \, dS + \int_V N_N^T \cdot f \, dV \tag{2.7}$$

$$F^N(U_i^M + c_{i+1}^M) = 0 \tag{2.8}$$

Here, the first integral represents the virtual work rate per reference value conjugated with material stress and strain, second integral is the traction force on designated surface and the second integral is the body force associated within the volume. The Newton's method considers that Eq. 2.8 solved by conducting virtual work equilibrium to get U, approximate result, that differs the amount of c. If it is expanded in Taylor series, all but the first two terms can be neglected due to magnitude of each c is very small. From that point the equation is transformed into a linear system of equation. Eq. 2.9, Eq. 2.10, Eq. 2.11 and Eq. 2.12 provided to show the expansion and the linear system.

$$F^N(U_i^M) + \frac{\partial F^N}{\partial U^P}(U_i^M) c_{i+1}^P + \frac{\partial F^N}{\partial U^P \partial U^Q}(U_i^M) c_{i+1}^P c_{i+1}^Q + \cdots = 0 \tag{2.9}$$

$$K_i^{N\,P} c_{i+1}^P = -F_i^N \tag{2.10}$$

$$K_i^{N\,P} = \frac{\partial F^N}{\partial U^P}(U_i^M) \tag{2.11}$$

$$F_i^N = F^N(U_i^M) \tag{2.12}$$

Finally, the next approximation in the iteration will be found by the following Eq. 2.13.

$$U_{i+1}^M = U_i^M + c_{i+1}^M \tag{2.13}$$

Regarding with this finite element method, the pressure and thermal loads are imported into the analysis model. The pressure loads are extracted from the CFD analysis that gave the optimized aerodynamic geometry. The thermal loads are altered by gathered readings and applied onto model. Here, the most critical case of the study which is the maximum AoA at last moment of missile life cycle is to be analyzed.

Boundary conditions are applied to the model as it should be in a real operational application. The transmission arm fixing bolt and planar surfaces of the shaft extension are the support of the model. These two interfaces can be seen on Figure 2.14

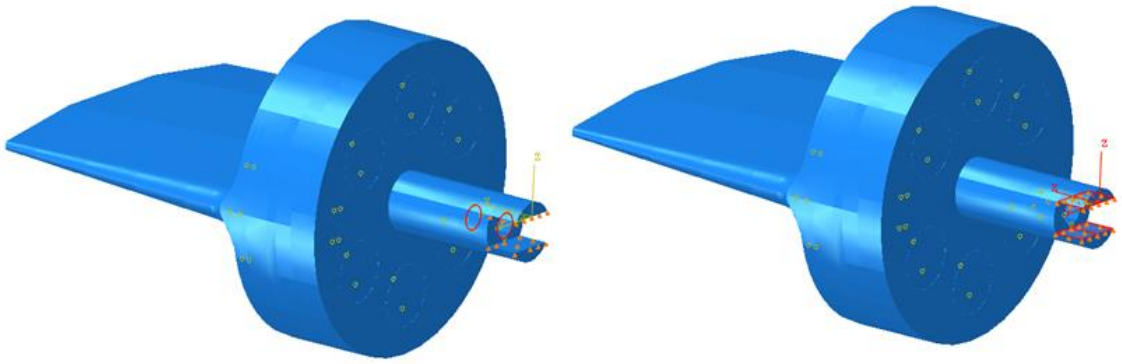

Figure 2.14: Support interfaces of the model

Analysis is completed with adding temperature distribution onto mechanically loaded structure. As a consequence, real operational environment is modeled with the pressure and thermal loads simultaneously. Pressure and temperature distributions are given in Figure 2.15.

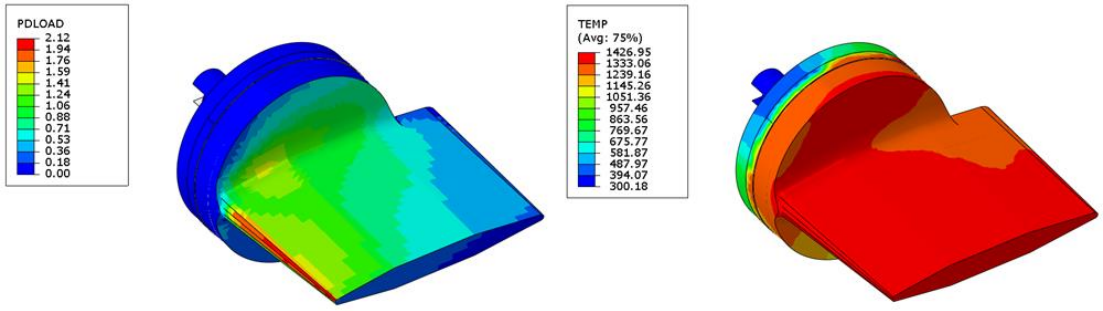

Figure 2.15: Pressure (MPa) and Temperature (K) distribution of model

The results for both model with interface and model with removed interface have been given in the following figures. The solution with the interface did not presents and failure with aerodynamic surface and the base instead bolt connections are completely overstressed and merged which means the failure is on that feature as in shown in Figure 2.16. This is a controversy with multiple test campaign which represents the unreliability of the computational analysis with heat transfer.

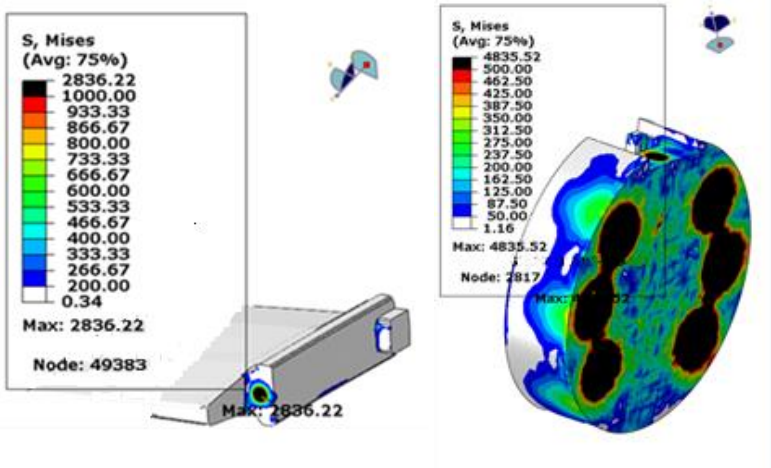

Figure 2.16: Thermo-mechanical analysis on preliminary design

On the other hand, model with removed interface has great improvement of structural integrity as it can be seen in Figure 2.17. The image presents safety factor that is scaled

from 0 to 1. It is better to show in this way due to different temperature values in the region. The safety factor is calculated according to yield strength at that temperature of each element in the model. Yield strength at specified temperature for unique element is divided by element based equivalent von Mises stress value and safety factor distribution for the finite element model is obtained. It is clear that the bolt connection stresses decreased. It is also has to be stated that the aerodynamic surface material (refractory metal 1) has almost 3 times less yield strength at elevated temperature of 1500 K while being at same thermal diffusivity. Therefore, the material is reselected for aerodynamic geometry as refractory metal 2 when unifying with the base regardless of the ablation rate problem which is more than refractory metal 1.

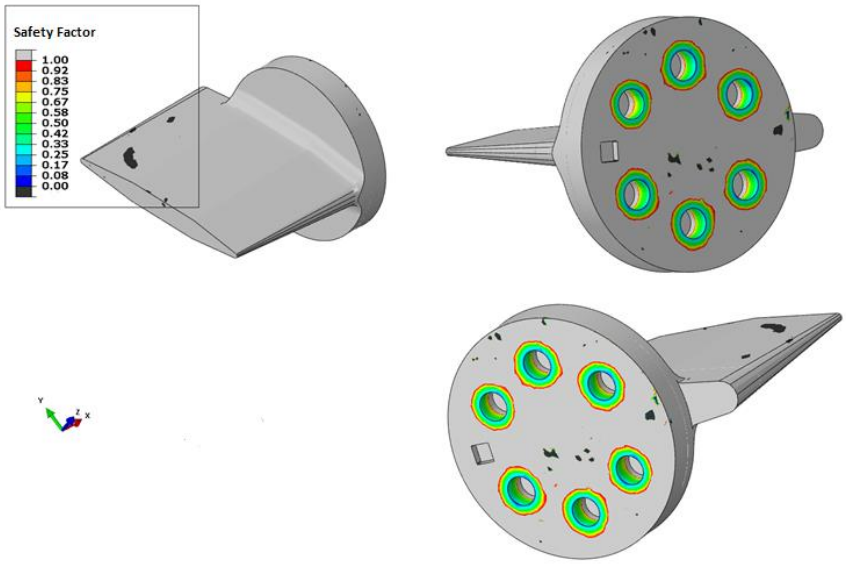

Figure 2.17: Thermo-mechanical analysis of conclusive design

TVC design that contains a unified aerodynamic surface and base, insulation, shaft and altered bolt connection did not show any failure mode in final structural integrity test; thus, to determine lift performance, the TVC is deemed to be tested on multi-axis force measuring test stand. In the following section, design of a test stand includes the

methodology of calibration and validation will be explained in order to have desired accuracy on lift measuring.

2.2 Multi-Axis Force Measuring Test Stand

Multi-axis force measuring test stand is aimed to investigate lift generation by 4 TVCs with an axis based approach. Great variability on computational fluid analysis to such chaotic flow environment causes difficulties on finding accurate results and it is better to test with such an instrument [Hamel et. al., 2003]. Therefore, the engine is captive fired and the forces acting on all axes are measured by load cells on this test stand. Since, there is more than one axis to be examined, the test stand should be designed, calibrated, validated and analyzed so that pure forces on TVC can be deduced. Following sections will cover these aspects step by step.

2.2.1 Test Stand Design

Design of a test stand is a complicated work due to having multiple parameters on modeling such as the configuration, features and calibration and all these aspects shall be incorporated and considered carefully [Runyan, Rynd Jr. and Seely, 1992]. As an example a ballistic missile requires only axial thrust measurement on the other hand a tactical missile with swift maneuverability requires all 3 axes where multi axes cause variations on these aspects greatly.

Captive firing of missile engine only is conducted by placing the engine on a platform manufactured in tight flatness margin so that the thrust vector and thrust measuring load cell axis can be aligned and by placing into several pads to hold still in non-thrust axes. The pads are connected to rail on both side of the platform so that the engine is free to move on single axis where the load cell will measure thrust by the displacement of engine. An example of single axis engine test stand can be seen in Figure 2.18. The measured force on load cell then can be calibrated by analyzing nozzle axis runout to have the actual generated force as an ideal condition of the engine thrust.

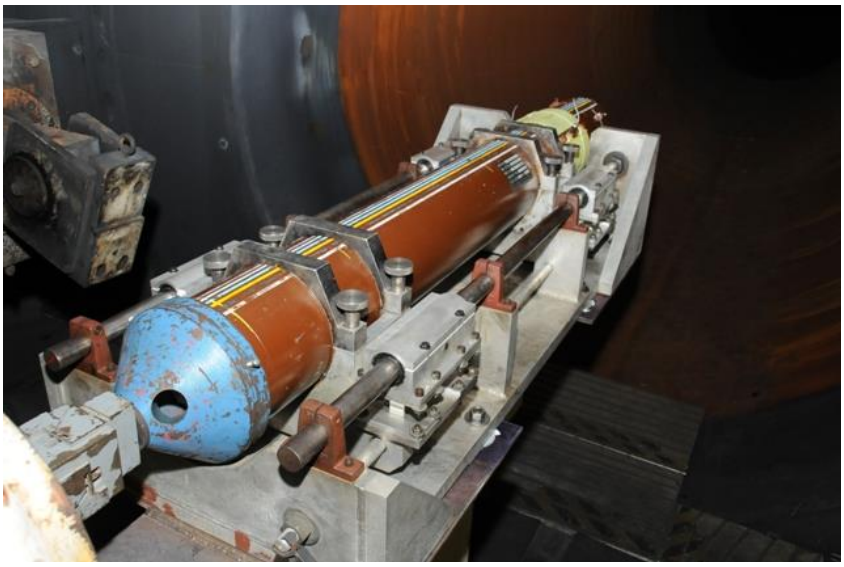

Figure 2.18: Single axis test stand in J-6 Large Rocket Motor Test Facility

While the engine is coupled by four jet vane based TVCs, the test stand requires another platform which can move freely on all axis. Therefore, the test stand has two mechanical components that one will serve as a base platform for it and the other is the moveable part which is suspended on top of the base platform by load cells. This allows the floating component to be freely in action on all axes with pitch, yaw and roll moment. This type of approach can be defined as 6 DoF for a test stand. Examples of 6 DoF test stands can be seen in Figure 2.19 and 2.20. Simplified schematic of a 6 DoF stand is presented in Figure 2.21 indicating axes and moment definition on such a stand.

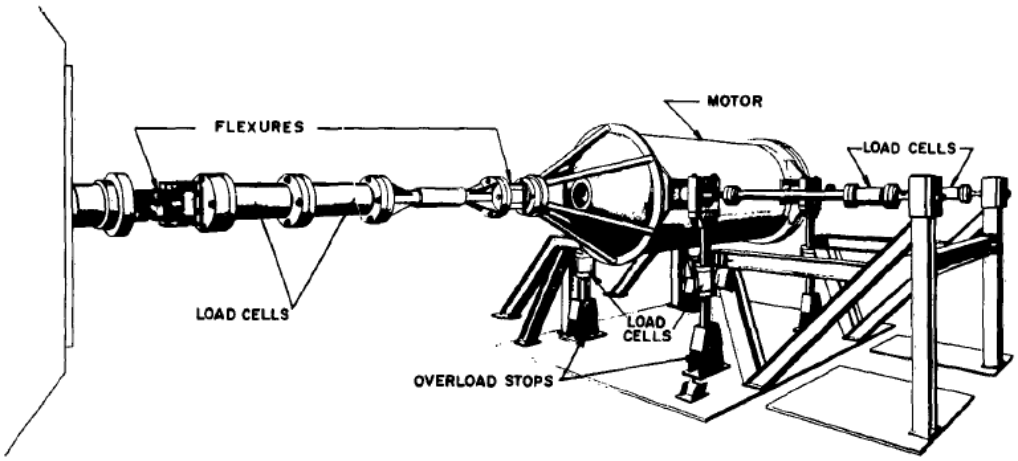

Figure 2.19: Example of 6 DoF test stand [Ankeney and Woods, 1963]

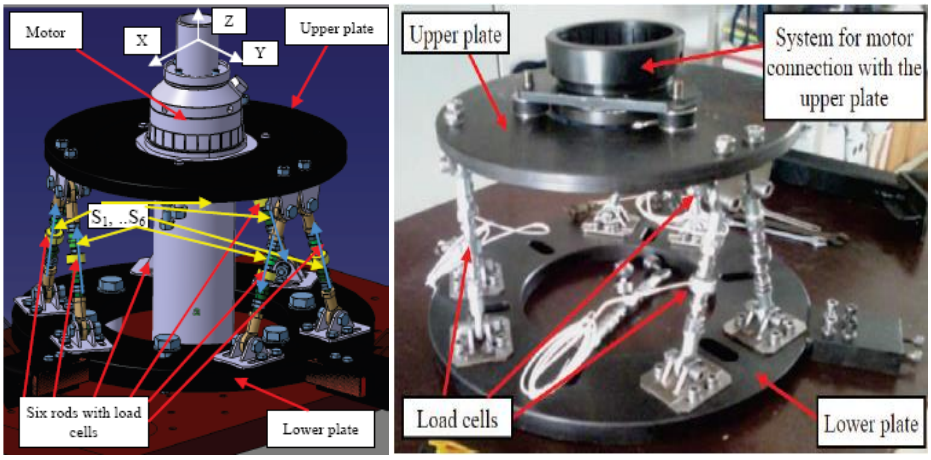

Figure 2.20: Example of 6 DoF test stand [Miloš et. al., 2015]

As it can be seen in Figure 2.20, the load cells are attached to the supporting rods between two plates in order to measure forces in Cartesian based axes and as in Figure 2.21, the axes are defined such that thrust axis became z axis, side forces became y and x axis. That approach is also used in this study but customized for the needs.

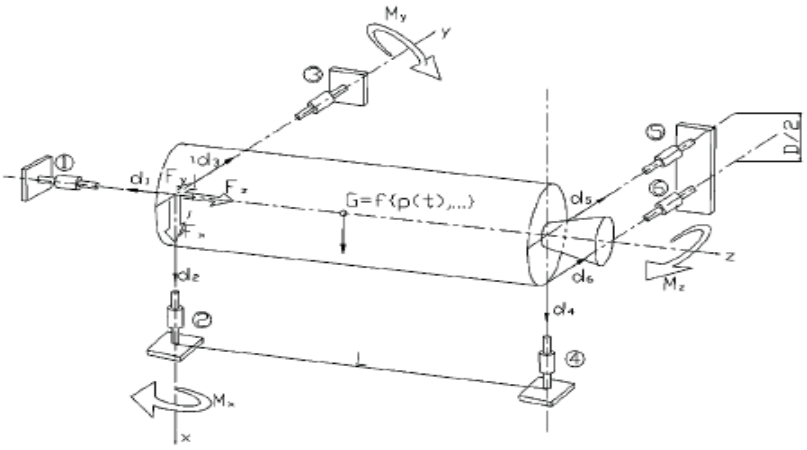

Figure 2.21: Schematic of 6 DoF test stand [Miloš et. al., 2015]

The test stand is aimed to examine jet vane based TVC and it is thought to be compatible with various missiles that will definitely have various diameter. Because of that reason, a vertical test stand that is similar to the given example is not applicable if the test engine diameter gets higher. The vertical test stand measures thrust in gravitational direction where the burned solid propellant decreases the weight of the missile that is going to be measured by the same axis. For such case, the deduction of the actual thrust is nearly impossible. The axis crossing on the center of gravity must be aligned precisely with the vertical axis of the test stand which will present difficulties. Therefore the design shall be more suitable if the approach given in Figure 2.19 is used.

As it is stated, the test stand shall be conceptually horizontal engine firing version and there will be a base frame and a suspended frame of it where load cells in between. Figure 2.22 shows the test stand CAD image where the axes, load cells and frames are designated.

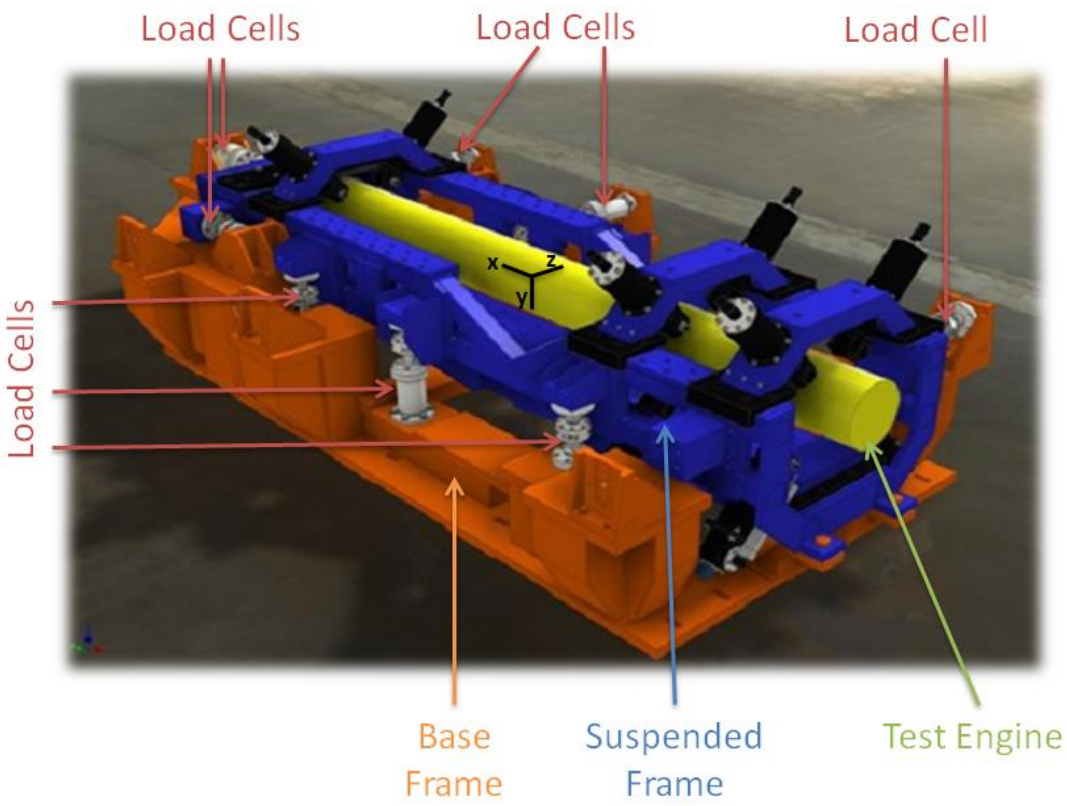

Figure 2.22: CAD image of the test stand

To sum up the important components of the test stand, Figure 2.22 shows the base frame at the bottom, suspended frame on top of it, a test specimen on the suspended frame, adjustable rollers to put test engines in different sizes and load cells around the test stand. Since the ultimate goal is to design a test stand such that it can present true values of the forces, the number and the placement of load cells have great importance. Additionally, the actuation of the load cells is also important because such a test stand in great dimensions and weight will require an on-site calibration. On-site calibration means, there are some calibration load cells on test stand which will be excited by external forces to determine the behavior of the test stand on site. Suggested approach is to hydraulically actuate the load cells because it is trustworthy and easy application which will be also used for this study [Sims and Coleman, 2003].

A true load cell calibration on site is executed by a calibration load cell coaxial with the intended load cell. If the load cell is in this position, the force generated by the calibration load cell is directly transferred to the measuring load cell. This is another standard and suggested application for load cell calibration specifically placing load cells coaxial with each other [Sims and Coleman, 2003]. An example of this case can be seen on a 6 DoF test stand for adjustable nozzle testing in Figure 2.23 where for instance CX1 calibration load cell and RX1 measuring load cell is on same axis. That is an important feature of a test stand if it is aimed to measure the moments of the forces. For a tactical missile, these are represented by pitch, yaw and roll moments. Tactical missiles are conducting their maneuvers by two properties, their fins and TVC. It is previously stated that the TVC based on jet vanes is used in launch sequence and the tail fins are used for the trajectory adjustment during the flight. That means the moments are related to fins and primarily the lift is related to jet vanes. Thus, the moment measuring on this stand can be omitted from the design which will also affect the number and placement of the load cells. They will be no longer required to be coaxial, if it is desired to do other than deem to be suggested.

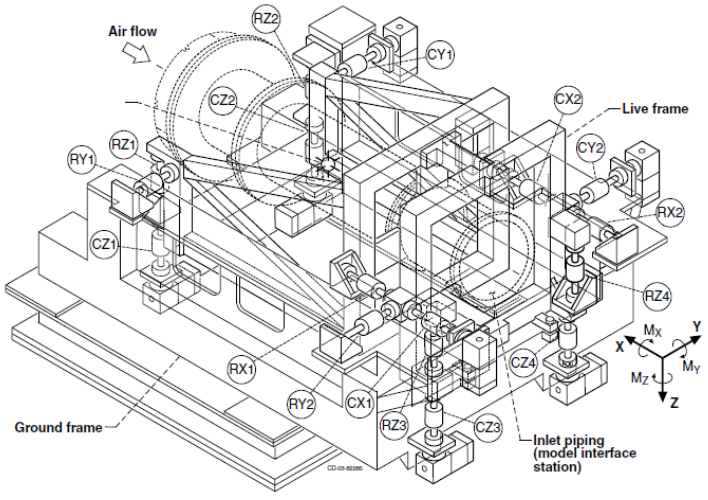

Figure 2.23: 6 DoF Test Stand [Wong, 2003]

The presented image of the test stand specified the load cells in 3D space; therewithal an illustration of the test stand is given in Figure 2.24. Here, the load cells are defined with three symbols. First one is either R or C which will represents the reaction and calibration respectively. Second one is either X or Y or Z which will represents the axes and the last one is the designated number of load cell. As it can be seen, there are 4 calibration load cells and 8 measuring load cells. These numbers and placements are determined by following considerations.

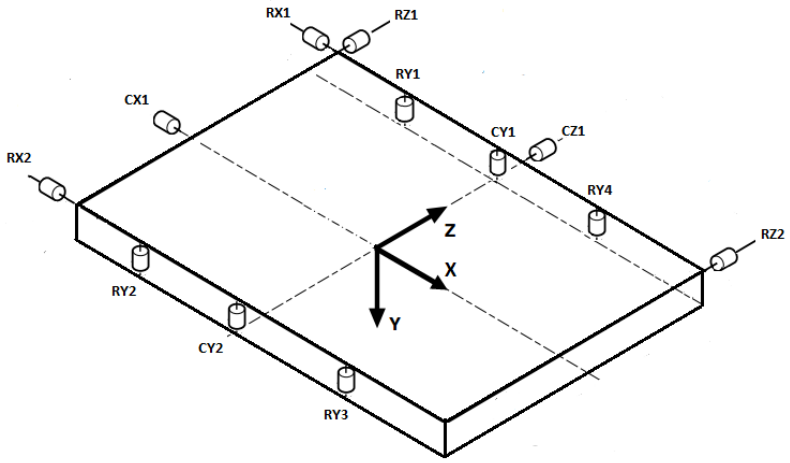

Figure 2.24: Illustration of this study's test stand

- The test stand is aimed to measure only lift, not the moments therefore the calibration of axes is required. This will allow designer mismatch the number of calibration load cell and measuring load cell. Without need to have moment calibration on test stand, the amount of calibration load cell decreased to 3 for an ideal condition, each one should be designated to one axis. The x and z axis contain one calibration load cell for each and they are placed on their respective central axis line.
- The x axis is measuring the missile thrust while the z and y axis are measuring jet vane lift. Y axis is the gravitational one which means descending mass of the solid propellant will be measured by it. Not only the imperfection of test stand

but also the imperfection of test engine brings out the impossibility to have a stable center of gravity on every test case. Additionally, different test engines provide different center of gravity point. Thus, there will be a fluctuation of center of gravity in each test. Because of that reason, at least two calibration load cells are required in y axis. These load cells are positioned on the longer edge of the test stand as it is shown in Figure 2.24. They are not in the shorter edge because of the longer moment arm around center of gravity. If there is a case of inconsistent calibration force generation by these two load cells, undesired moment will be generated and it would affect negatively the calibration procedure.

- Measuring load cells can be placed coaxial with these four calibration load cells however to ensure the stability of the test stand, it is better to place them in the corners. Therefore on x and z axis, there are four measuring load cells and they are precisely equidistant from their respective calibration load cells. On y axis, stated center of gravitation fluctuation and desired stability of the stand require four measuring load cells. Again they are positioned equidistant from the calibration load cells for equal load distribution of the system.

Despite of the test stand design with non-coaxial load cells, the generated forces have to be transferred onto load cells without any loss. For this reason, the suspended frame of the test stand is connected to base frame by flexures keeping the generated forces aligned with the measuring load cells. Figure 2.25 is representing the coupled flexure-load cell connection. The flexures have the capability of transferring the longitudinal force directly below to the load cell without bending or buckling considerably. They are bending by 4° if there is side force to not get it into account. To accomplish these tasks, flexures are designed at specific bending coefficients on axes, while having higher values for mitigating side forces and having lower vice versa. The appropriate values for them are determined by maximum forces that will act on them.

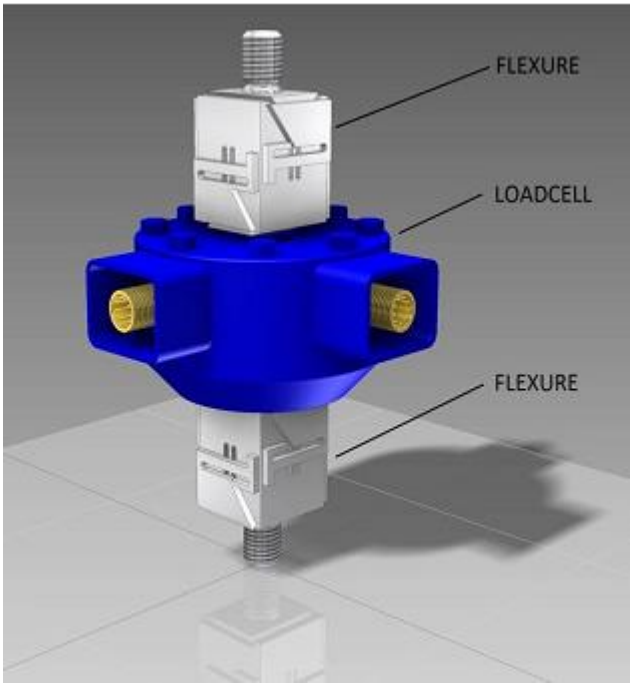

Figure 2.25: Interface between load cell and flexture

Adjustable rollers are the last important feature of the stand because the test engine has to be aligned with the stand's x axis. It is also important since unaligned thrust will generate undesired force on the other axis which will lead to incorrect lift readings. Because of that reason, the position of the engine on the test stand must be deterministic [Brimhall et. al., 2007]. Design of the engine mounting onto suspended platform is quadrant based in order to have equal load distribution on rollers. That means four rollers are in a set and at least two sets are design criteria. On this stand, there are three sets because of the shorter engine testing requirement. Since the alignment of the engine is conducted via adjusting rollers, it has to be ensured by potentiometers and laser tracker. The adjustment of rollers creates an error which will be also taken into account to determine uncertainty of the test stand.

The next section will cover the calibration procedure of such test stand where calibration and measuring load cells are positioned non-coaxially.

2.2.2 Calibration Process of Test Stand

Calibration of test stand is required due to imperfection of manufacturing and assembly, as an applied load on certain axis should only be measured on this specific axis but this is not possible in real life. By this knowledge, every axis on test stand contains one or more calibration load cells which they are already calibrated by voltage output at a certified laboratory. The calibration procedure of these load cells ensures a rated output by a third degree polynomial calibration equation and the coefficients of this equation are the inputs for load cell readouts after the load cell is commanded to apply various forces.

It has been demonstrated how the test stand is designed with load cell position considerations, it has to be expressed that the calibration procedure is also affected from this decisions such that the procedure will follow the axis based calibration. That means calibration load cell(s) will be used to calibrate its own axis rather than calibrating an individual load cell. This will form calibration force, measuring force and a total reaction force for every axis. From this viewpoint, calibration and measuring load cells and axis definitions are summarized in Table 2.1 for a better reading.

Table 2.1: Test stand axis definition

Definition (in column based order)	**Calibration Load Cell**	**Measuring Load Cell**	**Reaction Force**
Applied calibration load cell force in x-axis Measured load cell forces in x-axis Total measured force in x-axis	C_x	M_{x1} and M_{x2}	R_x
Applied calibration load cell force in y-axis Measured load cell forces in y-axis Total measured force in y-axis	C_{y1} and C_{y2}	M_{y1}, M_{y2}, M_{y3} and M_{y4}	R_y
Applied calibration load cell force in z-axis Measured load cell forces in z-axis Total measured force in z-axis	C_z	M_{z1} and M_{z2}	R_z

Calibration of the test stand is conducted so that a relation between reaction forces and calibration forces can be determined. This relation is often called as calibration matrix and it depends on how much stepwise calibration forces applied to the test stand; as the slopes between calibration and reaction forces are in better accuracy if more calibration steps are applied. [Wong, 2003] Additionally, calibration has to be conducted by zeroing the initial state of load cells to make each one in same reference. Both of these key points are used in this study's calibration procedure which is leading to a validation procedure.

Another important feature of the load cells is that each one can be in compression and tension state which they generate different reaction forces. Thus, each one should be calibrated with respect to its state. To do so, the test stand's each axis will be calibrated in compression and tension by using different calibration equation of calibration load

cells provided by laboratory. There is one exception in this methodology as x-axis is measuring the missile thrust and it will be always in compression state, therefore there is no need to calibrate that axis for tension. Following Table 2.2 represents the steps applied to each calibration load cells and their states, additionally their respective reaction forces read by measuring load cells.

Table 2.2: Test stand calibration procedure

State	**Range of Applied Force and Steps**	**Applied Calibration Force**	**Reaction Forces**
X-axis in compression	0 to 70000 N in 10 steps	C_{x_c}	$R_{xx}R_{xy}R_{xz}$
Y-axis in compression	0 to 8000 in 10 steps	C_{y_c}	$R_{yx_c}R_{yy_c}R_{yz_c}$
Y-axis in tension	0 to 8000 in 10 steps	C_{y_t}	$R_{yx_t}R_{yy_t}R_{yz_t}$
Z-axis in compression	0 to 5000 in 10 steps	C_{z_c}	$R_{zx_c}R_{zy_c}R_{zz_c}$
Z-axis in tension	0 to 5000 in 10 steps	C_{z_t}	$R_{zx_t}R_{zy_t}R_{zz_t}$

Each reaction forces are found by following set. This set defines 8 measuring load cells according to calibration axis and their reaction to that particular axis as in Table 2.3.

Table 2.3: Reaction equations of test stand

Formula	Notes
$R_{XX} = R_{XX_1} + R_{XX_2}$ $R_{Xy} = R_{Xy_1} + R_{Xy_2} + R_{Xy_3} + R_{Xy_4}$ $R_{Xz} = R_{Xz_1} + R_{Xz_2}$	Only in compression
$R_{yX} = R_{yX_1} + R_{yX_2}$ $R_{yy} = R_{yy_1} + R_{yy_2} + R_{yy_3} + R_{yy_4}$ $R_{yz} = R_{yz_1} + R_{yz_2}$	Equation set is same for compression and tension
$R_{zX} = R_{zX_1} + R_{zX_2}$ $R_{zy} = R_{zy_1} + R_{zy_2} + R_{zy_3} + R_{zy_4}$ $R_{zz} = R_{zz_1} + R_{zz_2}$	Equation set is same for compression and tension

To acquire calibration matrix, each reaction forces versus applied calibration force for all axis and state forms respective linear regression line which can provide its slope. As it is described earlier, slope of the regression line is found by the step points of calibration. Following equation represents the rate of change along the line stating reaction force change divided by the calibration force.

$$s_{ij_k} = \frac{\sum\left(R_{ij_k} - \overline{R_{\iota J_k}}\right)\left(C_{i_k} - \overline{C_{\iota_k}}\right)}{\sum\left(C_{i_k} - \overline{C_{\iota_k}}\right)^2} \tag{2.14}$$

i= x, y or z j= x, y or z k= c or t (compression or tension)

Eq. 2.14 generates 15 slopes according to 5 calibration axis-state corresponding to each three individual axis. It is obvious that, the measuring load cells can be in compression or tension state arbitrarily in actual test run depends on TVC position, therefore the slopes of compression and tension states are averaged to determine single slope for every axis readings. Following matrix represents 9 slopes for each reading and as an example first row-column stands the slope of x axis reaction force-x axis calibration force or second row-column stands the slope of sum of y axis reaction force-sum of y axis calibration force. The rest can be found by analogy. Here, the important parameters are S_{xx}, S_{xy} and S_{xz} as the other slopes indicates the interaction between axes and ideally they should be zero. [Wright et. al., 2013]

$$[S] = \begin{bmatrix} S_{xx} & S_{xy} & S_{xz} \\ S_{yx} & S_{yy} & S_{yz} \\ S_{zx} & S_{zy} & S_{zz} \end{bmatrix} \tag{2.15}$$

As it can be seen clearly, Eq. 2.15 indicates the relation between reaction forces and calibration forces. If it is multiplied by calibration matrix, it would provide the reaction forces and inverse of the slope matrix is the calibration matrix which will bring the calibrated readings [Yen and Bräuchle, 2000]. This statement also can be found in Eq. 2.16 and Eq. 2.17. Calibration method constituted here on defining a calibration matrix is a standard application and it is used for even a spacecraft attitude testing as camera calibration matrix [Cho, Jung and Tsiotras, 2009].

$$[S][C] = [R] \tag{2.16}$$

$$\left[M_{coef}\right][R] = [R_{calibrated}] \tag{2.17}$$

$$[S]^{-1} = \left[M_{coef}\right]$$

In the following section, methodology of test stand validation and how the calibration matrix and calibrated readings are important to find the accuracy of the test stand will be explained.

2.2.3 Multi-axis Test Stand Validation Procedure

Validation of a test stand is required to have the knowledge about the inaccuracy of readings as the objective reading should be well above the error margin so that the measurement can be meaningful. Nonetheless, the validation process can be conducted by various approaches where there is not any standard; commonly, analysis on hysteresis, non-linearity and repeatability is enough to determine the accuracy. [The Institute of Measurement and Control, 2013] According to given information about the calibration of test stand in previous section, the validation procedure for this study based on these three error sources will be explained.

The calibration procedure provides the calibration matrix [M_{coef}] to acquire corrected readings from the measured outputs of the load cells. To ensure a healthy data gathering, it is valued to have at least three consecutive calibration processes which will provide three slopes for five different states leading to averaged slopes for multiple calibrations. From this viewpoint, there will be three corrected outputs of test stand to be examined for hysteresis, non-linearity and repeatability.

2.2.3.1 Hysteresis

Hysteresis is an error type which is interested in difference between the outputs under same load. From the descent loading and increment loading sides which they are rated to

span of the measurement, the hysteresis can be determined by percentage of full scale. A simplified representation of hysteresis can be seen in Figure 2.26.

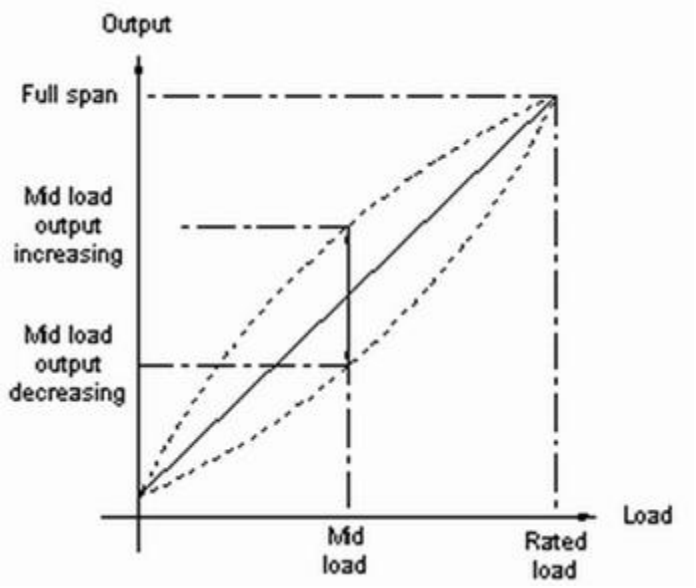

Figure 2.26: Hysteresis [Novatech Measurements Limited, n.d.]

$$Hysteresis = \left| \frac{50\%\ of\ R_{calibrated_{descent}} - 50\%\ of\ R_{calibrated_{increment}}}{span} \right| x100 \qquad (2.18)$$

The hysteresis formula is presented in Eq. 2.18. Here, 50% of calibrated reaction force means the half load output of the span. Hysteresis is applied by doing so as the output of a measuring instrument shows Gaussian distribution on its span which means the absolute difference occurs at mid-range. At every state of test stand, hysteresis amount is calculated for only primary axis where the actual loading is applied. It is obvious that, 15 hysteresis parameters will be found in total and every three consecutive calibration for five states will be averaged among the group to have final hysteresis value for each state.

2.2.3.2 Nonlinearity

Non-linearity is an error type that presents the difference between the output of a load and the linearized output for full scale. Again, since the outputs have a Gaussian distribution, maximum deviation on this matter occurs at mid-range. In Figure 2.27 the non-linearity is defined graphically. As it can be seen clearly, the vertical change on output on half loading is proportioned to the span. At every state of test stand, non-linearity is calculated for only primary axis with respect to Eq. 2.19 where the actual loading is applied, as same in the hysteresis case. Additionally, the procedure for every state is conducted likewise.

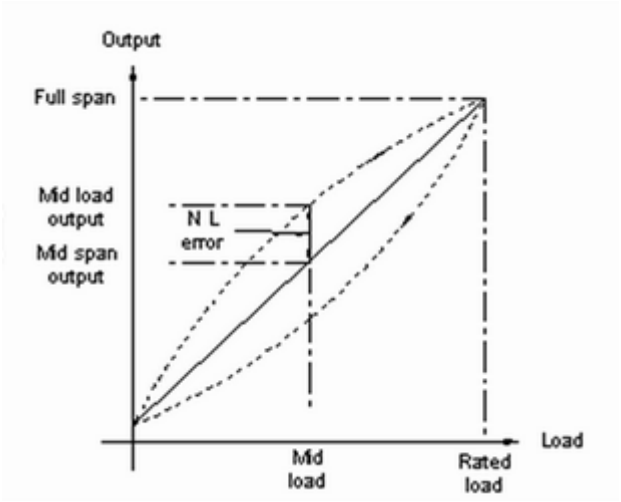

Figure 2.27: Non-linearity [Novatech Measurements Limited, n.d.]

$$Non-linearity = \left| \frac{50\%\ R_{calibrated_{increment}} - \left(\frac{span}{2}\right)}{span} \right| x100 \qquad (2.19)$$

2.2.3.3 Repeatability

Repeatability is an error type that investigates consistency of measurements. As usual, it is impossible to have the same output on every test however; outputs have to fall in to a narrow band to ensure the calibration procedure is conducted properly [Hawkins, 2014] To acquire repeatability information on three consecutive calibration processes, standard deviation of each calibration steps of them has to be calculated. As an example, x-axis calibration is conducted by ten steps increment and ten steps descent, therefore 20 individual repeatability values can be found. The maximum value of this group is the state based repeatability of the test stand. The mathematical expression of this statement can be found in Eq. 2.20.

$$Repeatability = \sqrt{\frac{(R_{calibrated} - \overline{R_{calibrated}})^2}{N}}\ , N = 3 \tag{2.20}$$

2.2.3.4 Total inaccuracy of the test stand

So far, the hysteresis, non-linearity and repeatability computation has been explained for 5 states and from this moment on, the combination of these error parameters has to be settled in order to have single inaccuracy value. For this matter, RSS methodology is adopted as mentioned error parameters are not correlated. Moreover, 5 state of this stand is also not correlated since they are executed part by part in calibration such that every state requires their own calibration load cells' equation. Thus, following Eq. 2.21 and Eq. 2.22 are used to determine the total inaccuracy of the test stand.

$$RSS_{state_i} = \sqrt{(Hysteresis_i)^2 + (Non - linearity_i)^2 + (Repeatability_i)^2} \tag{2.21}$$

$$RSS_{test\ stand} = \sqrt{\sum \left(RSS_{state_i}\right)^2} \tag{2.22}$$

The next section will explain the deterministic errors of the test stand and how to correct each error source.

2.2.4 Sources of Error on Measurement

In section 2.2.3, the methodology of test stand calibration has been explained and it is obvious that the process has reduced the amount of uncertainty of test stand. There are many error sources on multi-axis measuring test stand where an uncertainty analysis on such a test stand requires extensive work [Davidian, 1987]. Since repeating error parameters (bias) such as data acquisition error, ground noise error, test stand imperfection errors (include test stand manufacturing, load cells, actuators etc.) are reduced to desired level and evaluated with the calibration, there are three main sources of error to be considered related to accuracy of the measurement.

First of all, the ambient temperature is a significant parameter; the calibration and validation procedure must be conducted in a stable environment. To be able to determine how much precision on temperature is required, several pre-tests shall be executed in order to see the test stand behavior against temperature. Secondly, the calibration procedure has to be validated by comparing it with the previous standard tests. That will provide the knowledge whether the thrust axis measurement is correct and how much error on side axes occurs. Lastly, the other sources of error that can be controlled created by the test engine itself. For each test, the engine nozzle runout and centerline direction on test stand have to be deterministic. These parameters are unique to each test engine, thus they have to be known prior to captive firing.

2.2.4.1 Temperature effect on test stand

As in any of measurements, the ambient temperature has substantial effect on the accuracy. [Keller and Kordig, 1971] It is clear that every component on the test stand has a respond to temperature variation: the solid frame of test stand elongates in increased temperature, the load cells have correction factor to temperature oscillation

and the data acquisition instrument has signal noise on temperature fluctuation. To investigate whether there is a temperature trail, 18 hours of data collection with thermocouples on test stand has been conducted while the test stand positioned in open plane. It can be seen in Figure 2.28 the main x-axis (thrust axis) force measurement has been changed approximately 1500 N when sun light is directly hit on the stand. In this condition, the test stand can not be accounted for having a certain inaccuracy value that will lead to an unsure data set collection. Since the desired measurement of lift of TVC can not be deduced because of this reason, the test stand has to be placed indoor. All calibration and validation steps are executed in enclosed building conditioned ±2°C.

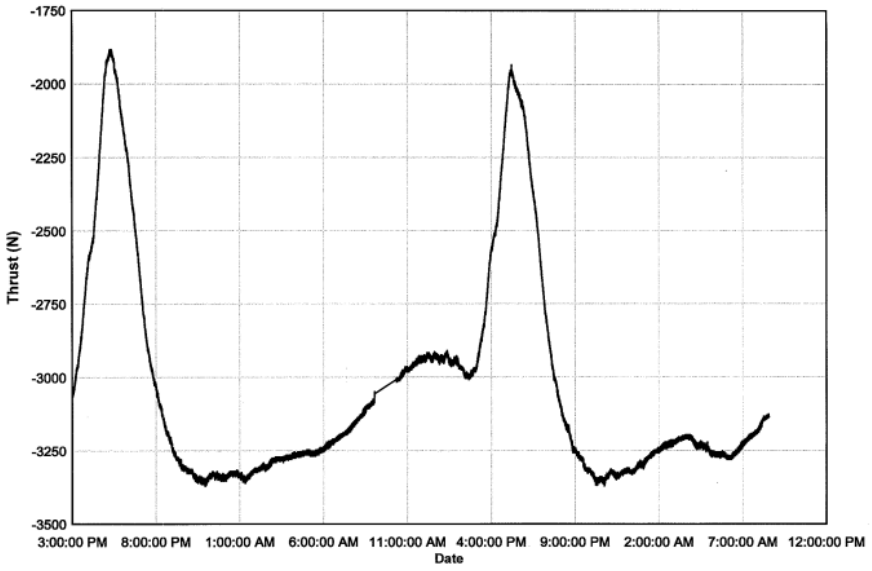

Figure 2.28: Temperature distribution on test stand in open plane

2.2.4.2 Captive firing effect on test stand

Resolved temperature instability provides a solid reference while concerning this study's test stand validity. It is important because the jet vane based TVC can create untrue readings in each axis and the temperature fluctuation would make the interpretation impossible. To be able to determine whether the captive firing affecting the

measurement, especially on thrust axis, comparison between firings on a regular test stand and this study's test stand can be made. That comparison can reveal the precision of thrust generation and the error margin of it which this test stand must lie within.

In order to understand how this comparison is made, calibration procedure has to be reviewed since the calibrated readings will be used for this purpose. As it is obvious that the calibration procedure is simulating the actual test, result of the Eq. 2.17 presents the thrust and side forces as a simulation. As an example of calibration procedure on x axis, the calibration load cell is generating the actual thrust values and these values measured by the reaction load cells on every axis. Previously obtained calibration matrix is multiplied by the readings on every axis which is stated Eq. 2.17. The result has to present ideally the calibration load cell value in x axis and zero force in y and z axis which will not be in such case. The values will definitely divert from this ideal case and diverted thrust axis values must match its counterparts on standard static firing test stand.

The test engine that has been used in the force measurement testing of TVC has also been tested on standard test stand for multiple times, therefore the test engine can provide a thrust consistency. To calculate how much thrust is diverted because of being on multi-axis test stand requires a correlation between the previous firings and the calibration loads. The previous firings have been checked to get the maximum and minimum boundaries within equal time interval. These thrust values are used to correlate with the calibration steps (calibration load cell forces) so that the calibrated readings can lie between these maximums and minimums. Selected thrust values are not always same with calibration steps therefore; a linear interpolation is executed to construct in-between data as it is given in Eq. 2.23.

$$R_{c_{i+1}} = \frac{\left(R_{p_i} - R_{p_{i-1}}\right)\left(R_{c_{i+1}} - R_{c_{i-1}}\right)}{\left(R_{p_{i+1}} - R_{p_{i-1}}\right)} + R_{c_{i-1}} \tag{2.23}$$

By Eq. 2.23, the calibration load cell forces are equal with the selected actual thrust values and calibrated reaction forces on x axis must be lower than the upper boundary and upper than the lower boundary. The other axes have already read undesired forces as a result of calibration. If the thrust axis is in the limit, these axes show the amount of error that has to be considered and omitted. If it is not, that means the test stand is not calibrated correctly.

2.2.4.3 Misalignment effect on measurement

Testing on different platforms has been investigated in previous article and provided insight knowledge about the difference between the calibration procedure and the static firing condition. It enables figuring out the errors on side force axis with reference of previous tests. So far, the calibration procedure is evaluated by this reference however there will be some alignment responses of actual firing that should be taken into account as it is stated in literature [Keller and Kordig, 1971]. For that reason, two misalignment of test engine will be examined in this article.

- The test engine is not a single solid part which has flanged connections onto it where it will ultimately has diverged centerline when it is placed onto test stand. This situation creates unmatched thrust measurement axis on the test stand thus moment and force generation on the side axes will be occurred.
- Another error source is the thrust vector misalignment to engine centerline. The cone starting from the nozzle throat to nozzle exit forms the thrust vector direction and it constitutes moment and force generation on the side axes as it is previously.

The misalignment of the test engine and test stand causes not directly transferring the thrust on x axis but also to the side axes leading to a moment and force generation. To overcome this problem, a laser tracker has been used to ensure the alignment. Since measuring with this equipment contains an error too, there can not be a perfect

alignment. Because of this fact, a square plane that forms the maximum measuring error boundary of laser tracker is used to calculate this alignment error. While laser tracker measures the test engine orientation, maximum error of 0.15 mm in both y and z axis can be occurred. The engine has an anchor point in front where it can be supported by the test stand. Therefore a three dimensional angle φ has been constituted between engine centerline and test stand's centerline. This situation is illustrated via CAD image in Figure 2.29.

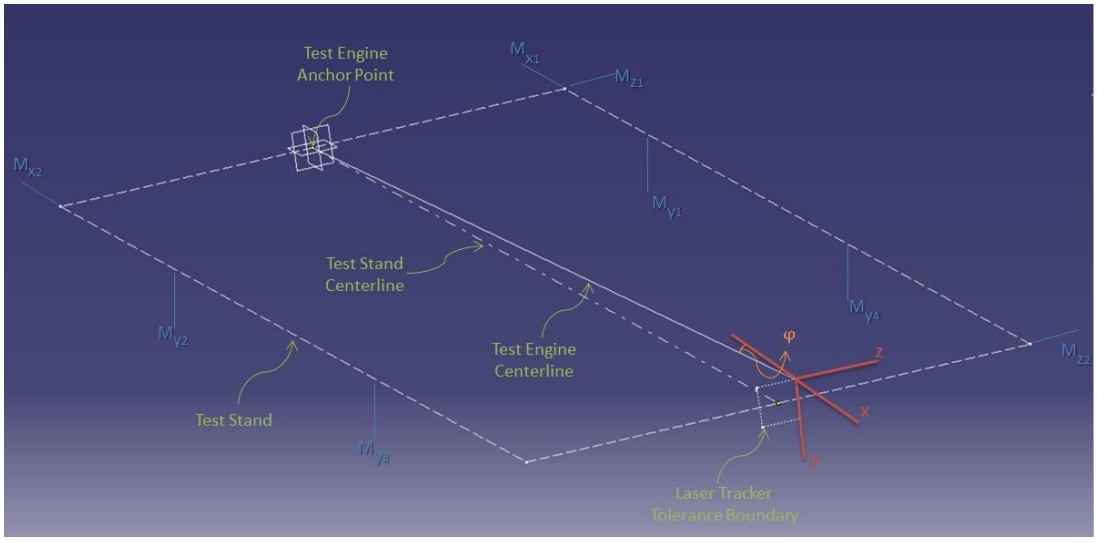

Figure 2.29: Illustration of test engine misalignment

To be able to understand the three dimensional vector passing through the engine centerline, an analogy is presented in Figure 2.30. Imagine that vector A represents the engine centerline which is diverted from the ideal z axis. The angle between vector A and z axis is defined as φ, same as before. The plane formed by x and y axis is the laser tracker measuring tolerance boundary which is a square 0.15x0.15mm in dimensions. Therefore the angle θ becomes 45° for this case. The aim is to find the undesired side forces generated by vector A which they are A_x and A_y clearly.

The forces are generated at the rear section of test stand, opposite site of the anchor point, since the engine nozzle is already positioned at this section. Due to this fact, the thrust vector has to be moved onto anchor point. That will allow the force transform into force-moment couple around it. Then the couple can be transformed back again into forces on center of gravity of the test stand where these forces will create additional loads in y and z direction.

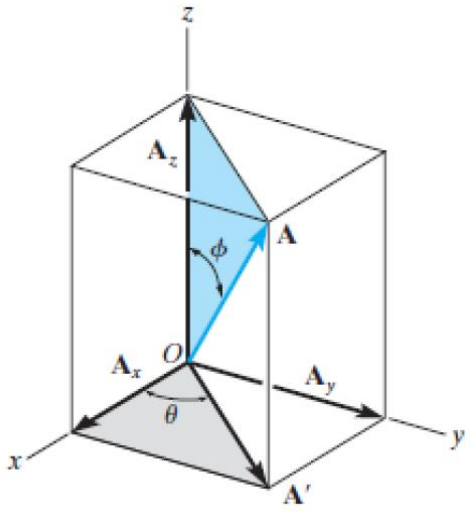

Figure 2.30: 3 dimensional vector in Cartesian coordinates [Hibbeler and Fan, 2011]

As it is stated, the moment generated by the misalignment can be transported to the center of gravity by Eq. 2.24 and three dimensional vector can be transformed into its components by Eq. 2.25, Eq. 2.26 and Eq. 2.27. R_{p_a} represents the reference firing's maximum and minimum values for each respective calibration load. These values are used because the resolution of the error can not be less than the boundaries otherwise it can not be detected.

$$R_{l_m} = \frac{\left(R_{p_a} \sin\theta \; e_{lt}\right)}{d_b} \tag{2.24}$$

$$R_{l_{fx}} = R_{p_a} \cos(\varphi) \tag{2.25}$$

$$R_{l_{fy}} = R_{p_a} \sin(\varphi) \cos(\theta) \tag{2.26}$$

$$R_{l_{fz}} = R_{p_a} \sin(\varphi) \sin(\theta) \tag{2.27}$$

The other important error source is the thrust misalignment of the test engine. Manufacturing of engine is conducted within certain tolerances and it is obvious that the perfect manufacturing of nozzle is impossible. Therefore, the nozzle centerline diverted from its ideal position which would be onto the engine centerline. As it is same with the engine misalignment, the thrust misalignment will implement additional forces on side axis. The CAD image of thrust misalignment is presented in Figure 2.31.

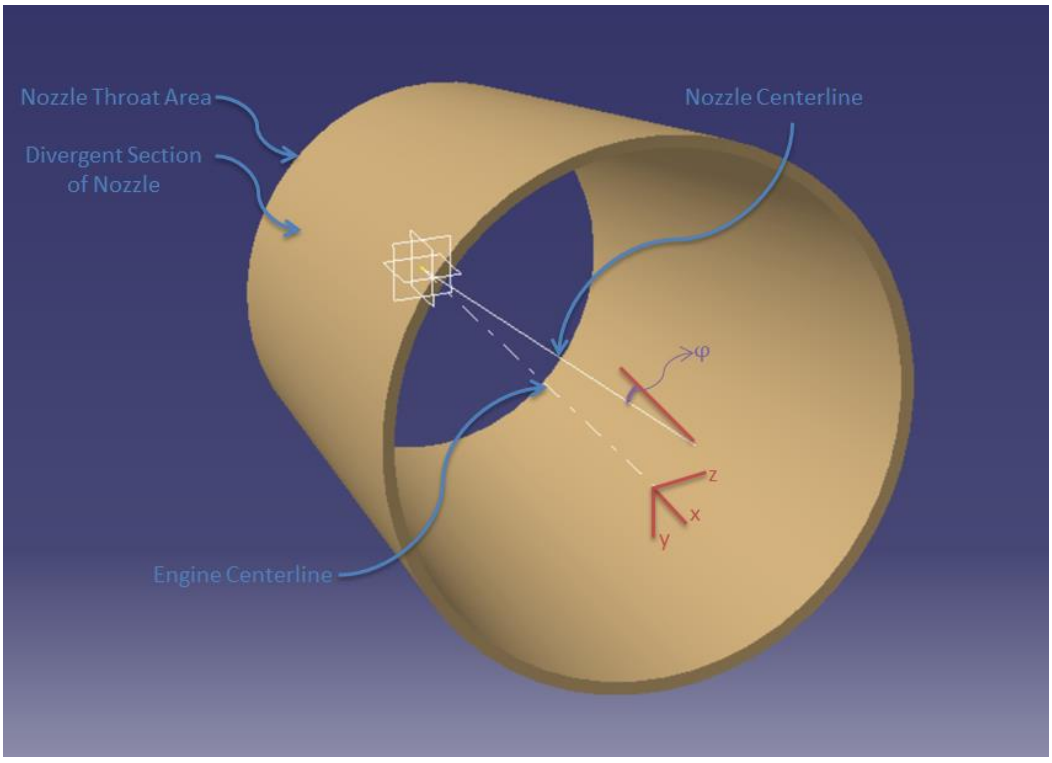

Figure 2.31: CAD image of thrust misalignment

Again, three dimensional vector with an angle (φ) to x axis is formed in this case. Distinctly, the angle between the other axes is not 45° instead the distances from y and z axes are measured by nozzle runout. The distances can be used to find out angle on y-z plane which is θ similar to designation of Figure 2.30. Thus, a trigonometric transformation has been executed to determine θ. That means Eq. 2.25, Eq. 2.26 and Eq. 2.27 are valid for the calculation of the forces in x, y and z axis. There will not be moment of this force since the engine centerline is already aligned and the throat area is positioned inside of the test stand.

Defined error sources up to this point are deemed to be evaluated prior to test and they have to be subtracted from the collected data which will be the last step of the error effect analysis. The actual reaction forces on x axis are constituted by omitting the misalignment errors from test readings. They also have to fall into the boundary that is formed by previous firings on standard test stand. On the other hand, the side forces require to be left out from the error of the test stand in addition to misalignment. These are described mathematically via following Eq. 2.28, Eq. 2.29 and Eq. 2.30 respectively.

$$R_{x_{actual}} = R_{x_{measured}} - R_{l_{fx_{TSM}}} - R_{l_{fx_{TVM}}} \tag{2.28}$$

$$R_{x_{ul}} > R_{x_{actual}} > R_{x_{ll}} \tag{2.29}$$

$$R_{y/z_{actual}} = R_{y/z_{measured}} - R_{y/z_{TS}} - R_{l_{fy/fz_{TSM}}} - R_{l_{fy/fz_{TVM}}} \tag{2.30}$$

2.2.4.4 Data acquisition and data reduction techniques for test stand

Data acquisition is an important parameter of testing where the quality of the data is determined. Moreover, favorable data reduction technique has to be applied on measurements which will conduct noise canceling, another essential procedure of testing. From that view; the load cells, DAQ equipment and data processing are joint parts of a single unit.

For a start, it is essential to measure both calibration stage and firing stage with single DAQ equipment and same load cells since altering on data collection will provide unforeseen inaccuracies.

Load cells have been used to convert thrust force to electrical signals for thrust measurements. Load cell selection has been made by accounting maximum and minimum load planned to measure by system. Furthermore extra loads may be encountered during tests. If a precaution is not applied, system could exceed maximum operational load and combined stress adversely affect the system which results in fatigue and decrease in system performance. Mounting kits are designed to reduce measurement errors, to protect the load cells and to simplify the mounting process.

DAQ component shall be selected and shall be acquired data such that it can be operated with load cells properly considering their sensitivity and rate of voltage output. For this matter, the suitable choice is IMC Chronos CRFX-400 because of its noise pre-filtering and multiple load cell reading features; moreover it has maximum 10V acquisition with 4mV sensitivity which is same with the load cell and sampling rate up to 100 kHz/sec digital input. By the help of this instrument, it is enabled to record data and analyzed it therefore, it provides user interface to apply calibration equation or unit conversion to be able to not conduct such task on post-processing. Additionally such features can be embedded into the instrument to be used for consecutive tests. Even though the DAQ instrument is precise on data collection, a noise filtering algorithm is always a must as an effective filtering requires multiple methods to be applied.

To accurately eliminate the noise level on readings requires Fast Fourier Transform of the signal to be able to acquire dominant frequency of the system and canceling all frequencies above that. FFT is known as a solid approach to noisy signal by transforming the data to frequency domain which enables to examine it properly [McAmis, 1991] [Brimhall et. al., 2008]. Eq. 2.31 represents the definition of FFT that is used in this study.

$$Y(k) = \sum_{j}^{n} X(j) e^{\left(\frac{-2\pi i}{n}\right)(j-1)(k-1)} \tag{2.31}$$

Here, Y presents the transferred frequency domain of X which consists of the time stamps and related readings. It is necessary to have the amplitude spectrum of Y(k) against frequency domain to pinpoint the frequency peaks, therefore following Eq. 2.32, Eq. 2.33 and Eq. 2.34 state these aspects.

$$AS_2(k) = \left|\frac{Y(k)}{L}\right| \tag{2.32}$$

$for\ k = 1\ to\ \frac{L}{2} + 1$

$$\left[AS_p\right] = [AS_2]_{(k,*)}[AS_1] = 2\left[\left[AS_p\right] - \left[AS_p\right]_{(1,1)} - \left[AS_p\right]_{(k,1)}\right] \tag{2.33}$$

$for\ k = 0\ to\ \frac{L}{2}$

$$f(k) = \frac{F_s * (k)}{L} \tag{2.34}$$

Here, AS_2 and AS_1 are two sided and one sided amplitude spectrum respectively. F_s and L are the sampling frequency and length of data array respectively. From that point, F_s versus AS_1 plot can be gathered for the peaks. Apart from the initial peak which represents the valuable data for measurement, there will be another peak which is for the dominant frequency (i.e. natural frequency value) of the system that rest of the frequency domain will be noise. To be able to determine the eliminating reference for the signal is one step of this process and the other step will be constitution of accurate filtering algorithm with respect to keeping meaningful data.

The filter design has considerable effort in data reduction process since captive firing contains important data such as ablation of insulation material creates sudden pressure increment or a multiple stage engine has a transition sequence which generates pressure increment due to deliberate stage separation. As a result of this, an accurate filtering has desired upmost, therefore a 4^{th} order Runge-Kutta Method for a second order filtering has been chosen. The reason behind this logic is the amount of collected data that has to be filtered. Higher order Runge-Kutta methodology is found to be effective in forward-backward filtering in 3-dimensional space or enormous data set. [Murray and Storkey, 2011] [Šoltészová et. al., 2012]

This method is using the four approximations to the slope technique which their mathematical representations are given below.

$$y_{t+h} = y_t + h\sum_{i=1}^{s} a_i k_i + R(h^{s+1}) \tag{2.35}$$

$$k_i = f\left(y_t + h\sum_{j=1}^{s} \beta_{ij} k_j, t_n + a_i h\right) \tag{2.36}$$

For s=4;

$$k_1 = f(y(t_0), t_0) \tag{2.37}$$

$$k_2 = f\left(y(t_0) + k_1\frac{h}{2}, t_0 + \frac{h}{2}\right) \tag{2.38}$$

$$k_3 = f\left(y(t_0) + k_2\frac{h}{2}, t_0 + \frac{h}{2}\right) \tag{2.39}$$

$$k_4 = f(y(t_0) + k_3 h, t_0 + h) \tag{2.40}$$

Here, k_1 through k_4 shows the halfway step on the slope which will estimate at the midpoint since they provide a higher order estimation, because of the k_2 and k_3 the outcome will be more accurate. To find the next step y_{t+h} as defined in Eq. 2.35 weighted sum of these slopes will be calculated. The residual R term is found via Taylor series which leads to Eq. 2.41 weighted sum coefficients. For this study, all driving equations are not presented and can be found in Reference section. [Carnahan, Luther and Wilkes, 1969]

$$y(t_0 + h) = y(t_0) + \frac{k_1 + 2k_2 + 2k_3 + k_4}{6} h \tag{2.41}$$

Filtering by 4^{th} order Runge-Kutta method requires a loop solver that makes the data reduced by a certain degree which then it will be inversed by same technique to constitute a new set of data and so on. That means, the loop will be use a dominant frequency which is found via FFT method, a damping ratio which depends on the sampled data and time step of the data which is also a parameter of collected samples. According to these inputs, the loop configuration will damp out the noise from the data and inverse it to form the new data set. The constructed loop function of this approach is given in Appendix B.

The following chapter covers the experimental results of TVC and test stand design which they present the validation of jet vane performance.

2.3 Experimental Results in Static Firing

In section 2.2, the design aspects of a multi-axis test stand, its calibration and validation procedure, additionally the sources of error on measurement are defined. In order to validate the jet vane design that is stated in section 2.1, calibration matrix, amount of inaccuracy of the test stand and bias errors of test stand has to be calculated. True validation can only be conducted by ensuring accuracy of the collected data. Moreover, the experimental approach helps to make a comparison with CFD results and the best

practice of CFD analysis can be determined which is stated in chapter 3. To summarize this section, following steps is performed to make the experiment.

- Initially the calibration matrix is constituted via analyzing the three consecutive calibration processes.
- According to these calibration processes, the inaccuracy of the test stand has been found and the test stand is validated with respect to desired criteria.
- The inaccuracy that been produced by the test engine (sources of error) is also evaluated and kept aside to be used in data reduction process.
- As it is stated earlier, y axis is the gravitational axis. In order to have the accurate lift reading on this axis, solid propellant weight decrement has to be accounted for.
- The final step consists of eliminating the test engine noise from the data. This data reduction process will be executed by Runge-Kutta methodology.

After these steps, the readings from y and z axis can be plotted onto each other to investigate the inconsistencies of experiment. It can be made due to selected test scenario which also has a dedicated article in this section.

2.3.1 Calibration Matrix

The calibration procedure is applied with respect to section 2.2.2. Calibration steps comprise great number of calculations, therefore it is given in Appendix-A. For an example, x axis calibration in cycle 1 - step 1 presented 99.5% of the actual value in x axis, 0.005% error in y axis and 0.24% error in z axis. The z axis has the weakest load cells thus; it produces greater error than the y axis. With same principle, each step in each cycle in every axis has been loaded by calibration load cells and measured by the reaction load cells. As a result, the Eq. 2.14 provided the slope matrix which is stated below. The Eq. 2.17 then presents the calibrated reaction force where $[M_{coef}]$ matrix is used. Calibrated reaction forces are also stated in Appendix-A with analogy. As it can be

seen clearly, the calibration matrix is approximately an identity matrix which means the loads that are applied in axis based are also read by related axis which is an indication of desired accuracy. All partial axis errors (i_{12}, i_{13}, i_{21}, i_{23}, i_{31}, i_{32} in matrix element definition) set below 0.007%.

$$[S] = \begin{bmatrix} 0{,}99410 & 0{,}00193 & 0{,}00633 \\ 0{,}00250 & 0{,}99794 & -0{,}00278 \\ 0{,}00519 & 0{,}00023 & 0{,}99799 \end{bmatrix}$$

$$[M_{coef}] = \begin{bmatrix} 1{,}00598 & -0{,}00194 & -0{,}00638 \\ -0{,}00253 & 1{,}00207 & 0{,}00280 \\ -0{,}00523 & -0{,}00022 & 1{,}00204 \end{bmatrix}$$

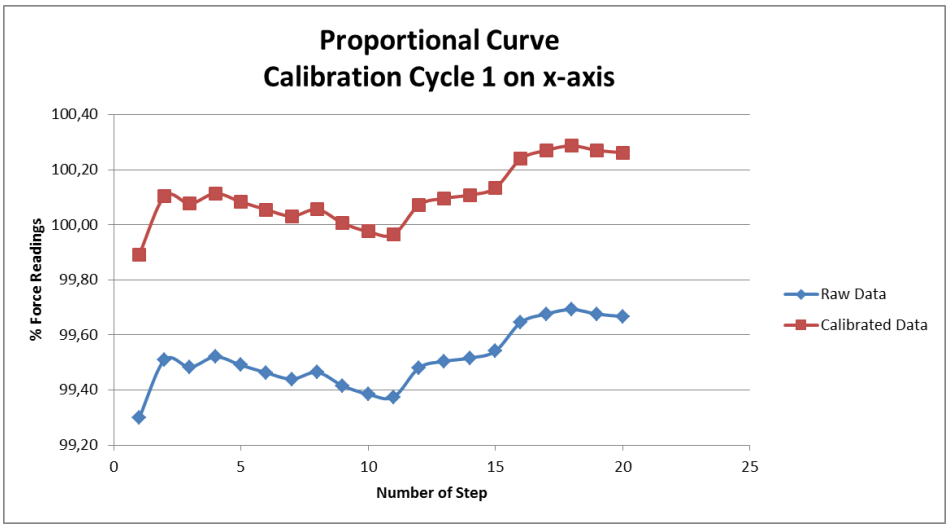

Figure 2.32: Comparison of raw and calibrated data on x-axis calibration

Figure 2.32 provides a graphical comparison between raw and calibrated data in x axis cycle 1 for an example. As a result of calibration procedure, measured reaction forces get closer to the actual values. 100% line indicates the true value of each step, read out from the calibration load cell.

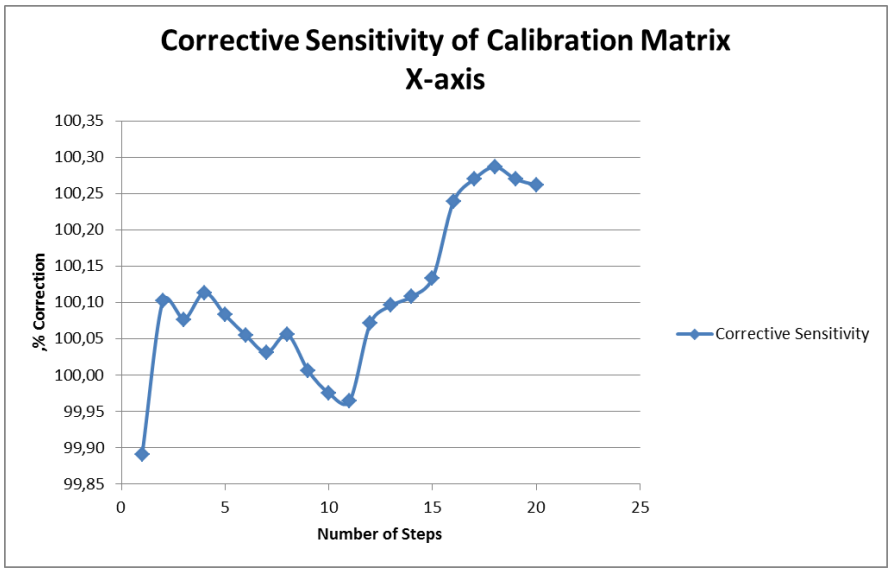

Figure 2.33: Corrective sensitivity on x-axis with comparison of actual and calibrated data

The calibrated reaction forces also demonstrate the success of the calibration matrix. For a closer look, Figure 2.33 is presented. The matrix is able to calibrate readings between 99.9% and 100.3% with respect to the actual values.

2.3.2 Validation of Test Stand

Being closer to the actual values is the indication of test stand accuracy, as it is stated in previous section however the overall accuracy (or inaccuracy of the test stand) requires to be looked at in each cycle and compression-tension state of the test stand for every axis. To do so, the procedure in section 2.2.3 has been executed.

The hysteresis, non-linearity and repeatability analysis results are found as in Table 2.4. They are derived the total inaccuracy value by RSS approach which has to comply with 0.5%. This value is selected because the minimum amount of error is generated by load cell and its error is 1% FS. The rule of thumb is to put the inaccuracy half of the minimum in order to safely operate under error resolution. It is obvious that 0.5% value

is quite conservative since the corrective sensitivity of calibration matrix ensures that outcome. The total inaccuracy is calculated as 0.38% despite most of the non-linearity and repeatability on each state elevated comparing to other parameters. It can be deduced that great inertia of the test stand generates proportionally increased reaction force on load cells which tends to yield in non-linear form.

Table 2.4: Inaccuracy parameters and total inaccuracy level of test stand

State	Hysteresis (%)	Non-linearity (%)	Repeatability (%)	RSS at States (%)	Total Inaccuracy (%)
X-axis	0,01958	0,13140	0,13140	0,18686	0,38059
Y-axis in compression	0,07849	0,09564	0,05863	0,13692	
Y-axis in tension	0,04226	0,02391	0,11408	0,12398	
Z-axis in compression	0,01985	0,26404	0,03831	0,26754	
Z-axis in tension	0,05428	0,01670	0,03185	0,06511	

2.3.3 Test Stand-Test Engine Coupling Errors

Errors on each axis due to test stand and engine coupling have to be deterministic since there is still test stand error after calibration procedure and there are misalignment errors that are related to test engine. The calibration procedure does not ensure y and z axis to become zero reading with direct thrust in x axis therefore; by the help of reference firings, these extra measurements are omitted effectively. The alignment errors are also calculated by the approach stated in section 2.2.4. These methodologies present upper and lower boundaries of errors due to the reference captive firings' thrust deviation. In order to precisely match with the minimum required lift, the upper boundary values will be treated as the maximum amount of error that can be experienced on test phase.

In Table 2.5, the first column represent the ultimate difference created by test stand under test engine firing alone condition, the second column represent the centerline

misalignment of test engine with the aspect of moment and force deviation and the third column represents the thrust misalignment of test engine that caused by the imperfection of nozzle manufacturing. As it can be seen clearly, the total amount is around 38 N in y axis and 74 N in z axis. The total amount of error on x-axis is negligible since the value is under 5 N and it has not been shown in Table 2.6. To have clear view about how the boundaries are changing in time, portion of static firing can be found in Figure 2.35. For x-axis, the reference thrust margin is shown proportional to maximum thrust in Figure 2.34.

Table 2.5: Corrective factors for forces on y and z axes in amount of error

Corrective Factor	Test Stand (N)	Centerline Misalignment (N)	Thrust Misalignment (N)	Total (N)
Y-axis at max	13,32027	25,35519	19,88094	38,42437
Y-axis at min	12,72836	24,24935	19,01386	37,89557
Z-axis at max	21,98956	24,97548	48,14915	74,60249
Z-axis at min	20,16577	24,70125	46,04919	74,05210

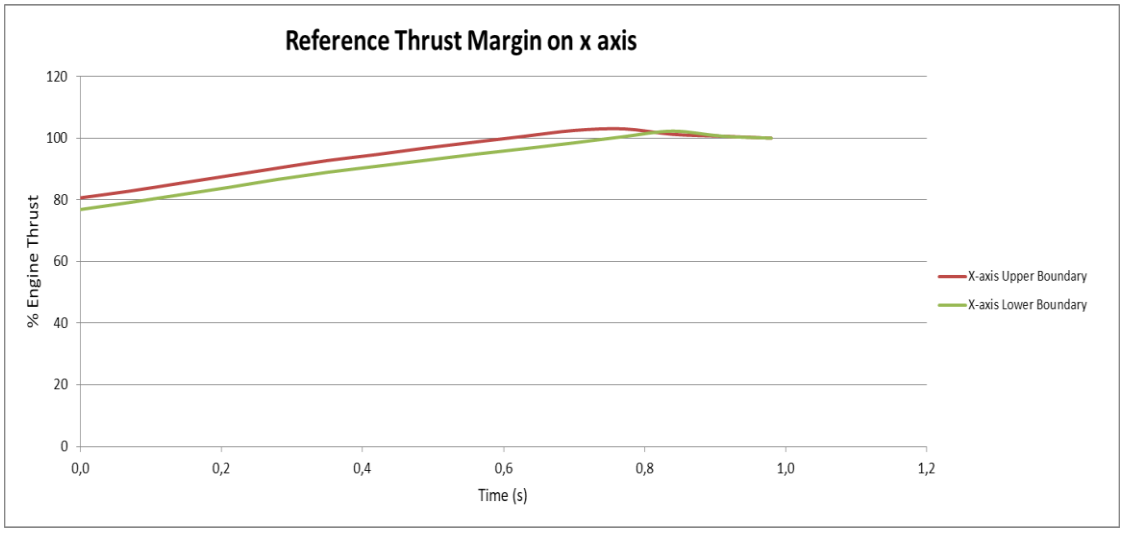

Figure 2.34: Reference thrust margin on x-axis

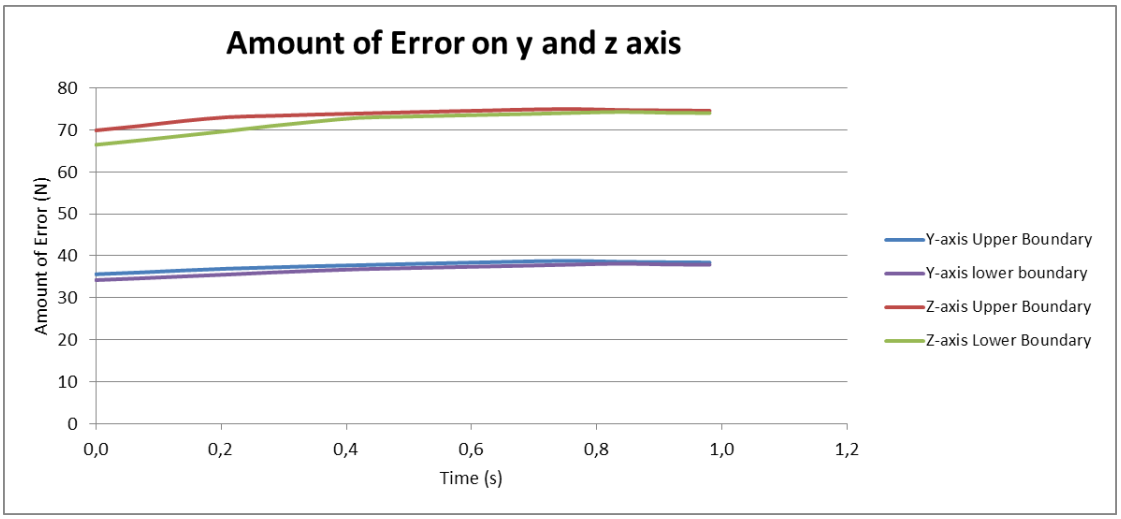

Figure 2.35: Amount of error on y and z axis

2.3.4 Correction of Readings due to Engine Weight

Another correction is mandated in y-axis as this axis measures the propellant weight consumption during the captive firing. If the test phase begins with a zero reference in y axis, the last reading from y axis will be exactly less amount of propellant weight while jet vanes are in zero AoA. Due to this fact, the propellant consumption in time has to be added into y axis measurements. The consumption rate is evaluated by the pressure readings on test engine which will present the burn rate of the propellant. Burning area of the propellant is a known parameter therefore the consumption rate can be found against time. Consumption rate is conservative as the manufacturing of the propellant is a process that involves testing it prior to application on test engine in a manner of determining burning rate. Therefore the consumption rate is accurate and omitted from being a constant shift on y-axis measurement. Figure 2.36 presents this consumption rate against normalized time of the test.

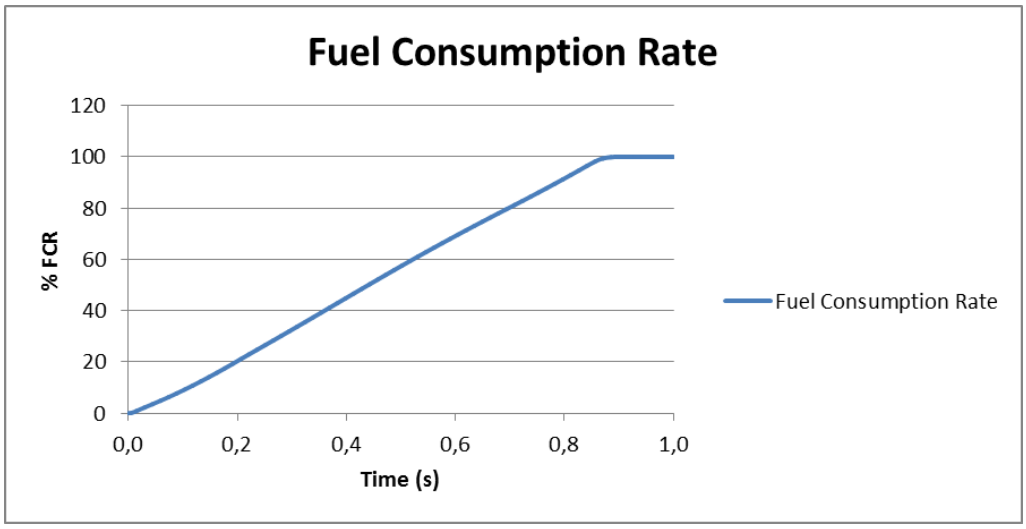

Figure 2.36: Fuel consumption rate of test engine

2.3.5 Results of Data Reduction Process

Data reduction process is required due to significant noise on any measurement. It is obvious that the noise canceling has to be executed while keeping the useful data. To be able to do that, the dominant frequency of the noise has to be determined, which is done by the methodology described in Section 2.2.4. (Fast Fourier Transform) In Figure 2.37, it can be seen that the 30.25 Hz and above in frequency domain shall be filtered. The rest of the graphic does not present any other significant amplitude therefore it indicates that the filtering process will be ended with well outcome.

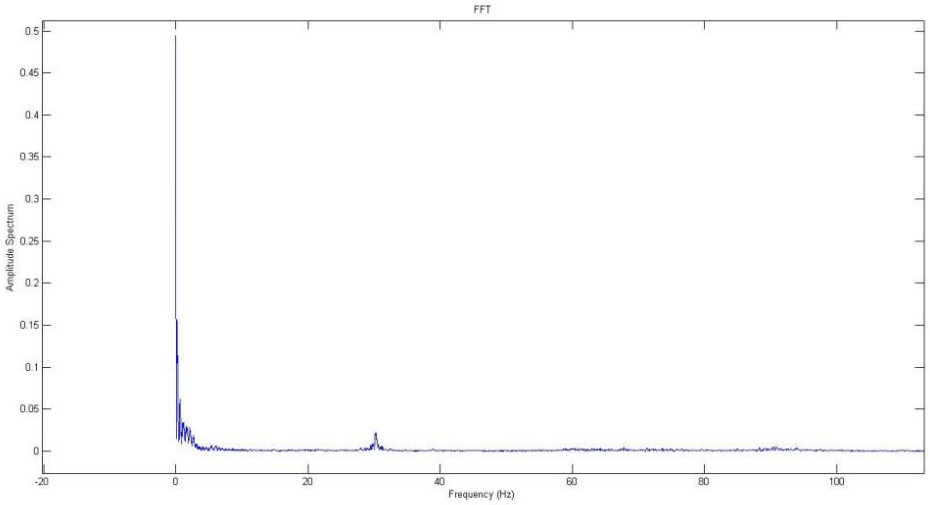

Figure 2.37: FFT of test data

By previously determined Runge-Kutta technique, the raw data that collected by DAQ instrument is filtered with the least valuable data loss as both can be seen in Figure 2.38. The data is gathered on y-axis which also measures the gravitational change by the burning propellant; thus the reading does not end with zero lift as it should be. This data is intentionally chosen to indicate how much measurement noise has been introduced in captive firing and the validity of the noise removal application as the consumed propellant is deterministic and does not pose any problem on filtering. The axis labels and quantities are hidden due to privacy considerations. Figure 2.39 is separately given in order to show the match quality of jet vane deflection scenario which will be presented in following article. It presents that despite the level positions of the jet vanes are found as descending if the repositioning of them takes less than 0.1 seconds; the valuable lift output requires more than this duration for a tactical missiles, therefore the difference is neglected.

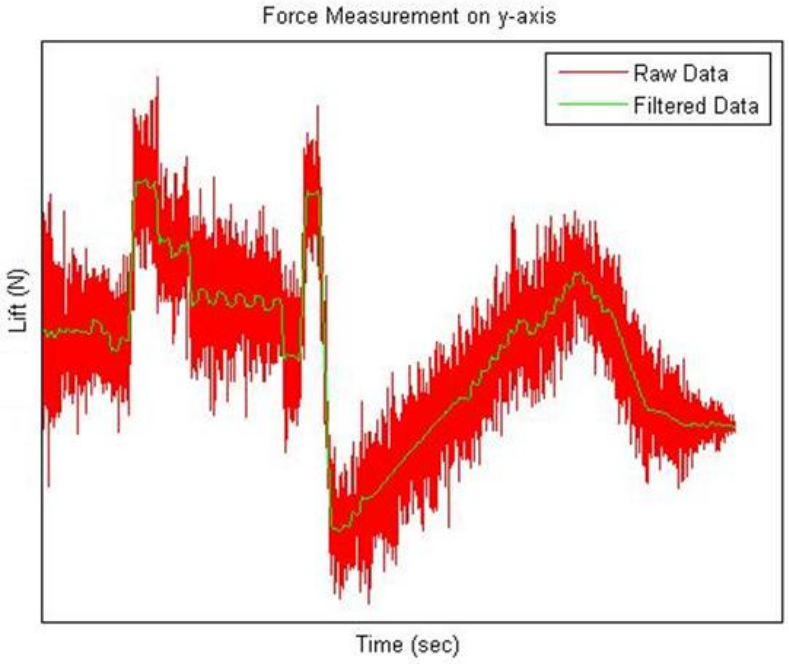

Figure 2.38: Noise filtering with 4thorderRunge-Kutta method

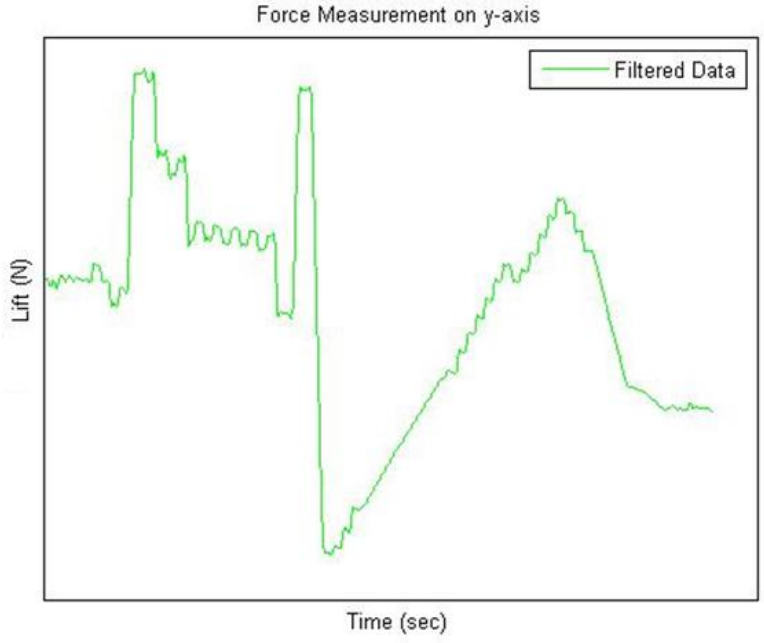

Figure 2.39: Filtered data of y axis

2.3.6 Applied Test Scenario and Results of the Experiment

The test scenario of 4 jet vane based TVC coupled with engine is presented in Figure 2.40. TVC is positioned in (+) formation at rear section which enables direct lift measurements by related axes. As an example, the pitch maneuver is generated by horizontal jet vanes which will be measured by gravitational y-axis. The half of the total force reading will present the single vane lift output.

As it can be seen clearly, the scenario investigates numerous AoA which is essential to get a performance analysis. There are three important findings will be acquired with the test as the effect of ablation on lift generation, response time of the vanes which is the actual lift generation after command and of course the lift versus AoA.

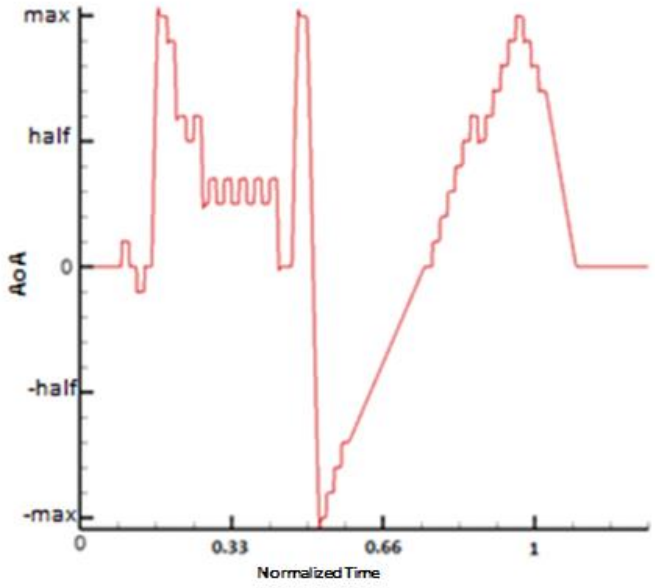

Figure 2.40: Test scenario of the study

According to test procedure that has been stated in this chapter has been conducted and lift on y and z axes has been found as in Figure 2.41. Ideally, these two axes have to present identical outputs and trend shall be matched with predetermined test scenario. As

it is also stated that the error amount of axes are eliminated due to applied calibration and corrective procedures therefore readings are valid to deduce.

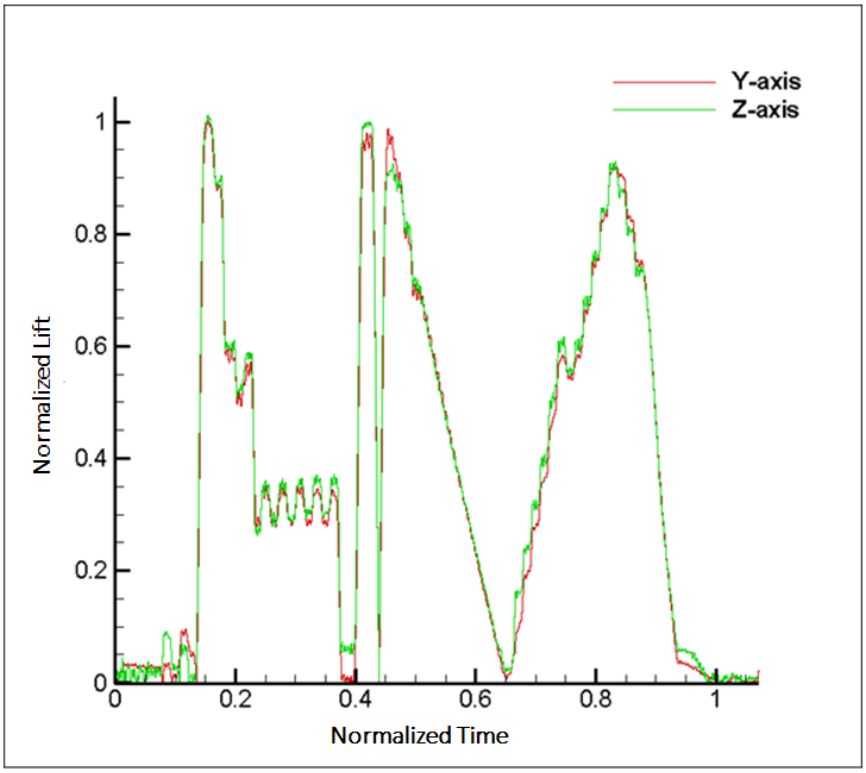

Figure 2.41: Experimental normalized lift measurements on y and z axis

Figure 2.41 shows both y and z axis thrust proportioned lift as normalized values since the amount of percentage is hidden due to privacy concerns. Additionally, the negative angles are reversed to compare the generated lift in different time on testing. Overall, the trust stand provided coherent readings on both axes, though there are minor differences.

- Around time of 0.1, there is inconsistency on lift reading which is caused by the inaccuracy of the load cells for too low measurement demand. As it can be seen in error analysis of test stand, these lowest readings falls into the maximum error amount that generated by the coupled testing. Additionally, the intended lift force

is quite lower too. As an example, the maximum lift is over 10 times larger and it is the minimum calibration level for the test stand. Clearly, the methodology presented in this chapter misses the lower levels of lift and misjudging the amount of error leading to considerable percentage of difference between axes. Therefore, it is concluded as there is a minimum lift generation measurement limit.

- Over time 0.2, the surface ablation provides losses on lift. The maximum variation can be seen on lift in maximum angle between the time of 0.5 and 0.85 The operational duration of jet vane based TVC is lower than 0.85, by the time the tail fins that placed outer surface of the missile is in effect. The valuable information is how much lift loss is occurred due to this effect and it is around 10%
- Considerable difference between y and z axis can be seen around time of 0.5 which can be explained by the implementation of fuel consumption rate assumption. On that particular time burn rate of the fuel can be different from the ideal case; even the generated lift is equal between both axes in previous step, error on summation of the fuel consumption onto y-axis will cause such an effect.

To add up, the multi-axis test stand trials provides valuable inside knowledge on lift for various AoA, therefore it is found to be comparable with a CFD effort aiming to have solid approach to analyze geometries beforehand without conducting tests.

CHAPTER 3

COMPUTATIONAL FLUID DYNAMICS PHASE

3.1 Meshing & Mesh Specifications

For the scope of this study ANSYS meshing tool has been employed extensively. Full model of the thrust vectoring vanes are generated with the CAD software and then imported to ANSYS media. Unstructured mesh has been preferred since its relative easy application for dirty (geometries with sharp edges and small patches) CAD models. Global sizing controls have been determined first, then refinements and local sizing have been performed, following the utilization of inflation option for boundary layer flow near the vanes. Lastly, assigned mesh has been evaluated with the help of quality control parameters such as skewness, aspect ratio and expansion ratio.

3.1.1 Structured and Unstructured Mesh

There are mainly two types of mesh algorithms which are defined as structured and unstructured. They differ in terms of memory usage, therefore CPU time cost for the same application also there are differences concerning flexibility required by the problem.

The definition is generally given as follows for a structured mesh; it will only store node location in 3D space in the format of i, j, k where consecutive cells' nodes will be defined as i+1, j+1 and k+1 or i-1, j-1 and k-1 depending on the chosen global axis. Therefore, there will be no need to store the connectivity of the cell nodes since it is already known because of the algorithm it utilizes.

Some problems including complex geometries may need to be divided into sections which it goes by the name “blocks” in terminology. These blocks can be defined with different size controls. Apart from that, there are known adaptive algorithms in some commercial software such as ANSYS that includes multi-zone approach, which utilizes tetrahedral elements within the same problem that defined with hexagonal elements dominantly. On the downside, some problems with steep gradients of curvatures or sharp edges are really hard to model as blocks and must be modeled with unstructured algorithms.

Unstructured algorithms utilize node numbers and connectivity table instead of node indices. This method requires more memory however, it grants more flexibility to user in case of problems with complicated geometries.

For this study, patch conforming unstructured mesh with tetrahedral elements have been used because its ease of application. Also patch conforming tetra mesh method allows for utilization of 3D inflation for boundary layer calculation or modeling depending on whether wall function is used or not. Inflation will be explained in the following sections.

3.1.2 Mesh Elements

There are 4 types of mesh elements generally utilized through the literature whose names are tetrahedral, quadrilateral prism, triangular prism and hexahedral. Short definition of the elements will be given in this section with the advantages and disadvantages of using them.

Tetrahedral mesh element has been widely known for its reduced setup time and it does not require surface mesh to be assigned beforehand. Option to be used together with hexahedral or prism elements is present for boundary layer calculations. This issue is critical since the meshes with this type of element; capturing shear physics is not

effective. Also the cells are never fully aligned with the flow, causing reduced accuracy compared to meshes compromised of hexagonal elements.

Quadrilateral prism element is known to be utilized between hexagonal boundary layer meshes and tetrahedral mesh elements for smooth transition. In Figure 3.1, shape of the element is shown. Triangular prism element (wedge) is also similar to the quadrilateral one however; triangular prism element may be used in boundary layer directly unlike the quad, since it is known to yield satisfactory results.

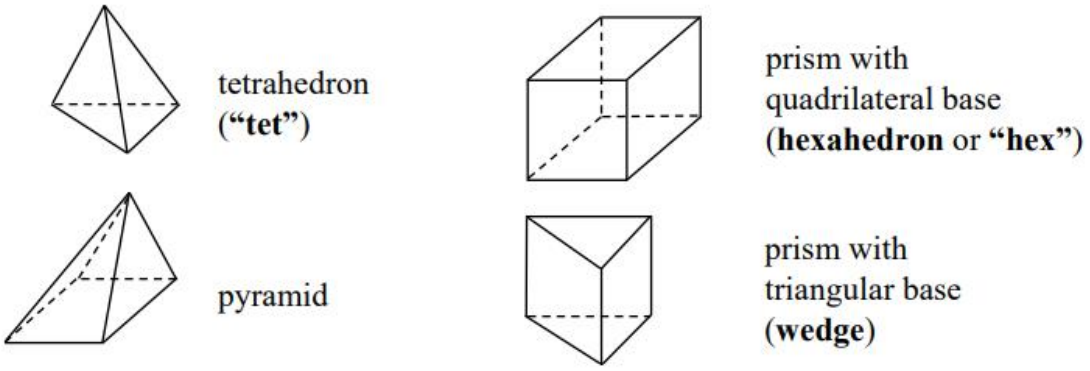

Figure 3.1: 3D Mesh elements

As for the hexahedral element which is essentially a topological cube or sometimes referred as brick, solver accuracy is the highest for a decent mesh. Being stated that, one must also pay attention to the flow direction relative to the element faces which may result in reduced accuracy if it is not properly aligned with the flow. Even though higher accuracy is achievable with hex, complex geometries is harder to mesh with hex compared to tet, thus hybrid meshing techniques and multi-block meshing options are available for the most commercial meshers.

3.1.3 Sizing

ANSYS size controls may be inspected in two parts which are global controls and local sizing controls. Both of these controls affect the solution convergence, convergence rate and accuracy of the solution dramatically.

3.1.3.1 Global sizing

Global sizing is the first step to determine the mesh size. It has been chosen so that, there is not any large cell compared to control domain. Also, there are not many small cells present in the fluid domain excluding the vane faces in order not to increase the element number enormously. Thus, there are bigger cells and global size controls dominate where the flow is thought to be developed fully. There are smaller cells where the curvature gradients are steep and size is controlled by local sizing controls.

Active assembly seed control has been chosen for the initial mesh sizing. This option bases the initial seeding, depending on the measure of the diagonal of bounding box that encloses the unsuppressed assembly parts.

3.1.3.2 Local Sizing and Refinements

Proximity and curvature sizing control has been utilized for the mesh. This sizing function, unites the two different sizing controls which are expectedly named as proximity size function and curvature size function.

Proximity size function determines the element size depending on the internal volumetric region between two faces and area between two opposing boundary edges of a face and results in refined the mesh in these areas which are defined as “gap”.

Curvature size function changes the local size considering the allowed curvature change between consecutive cells over a face. The function divides the curved sections until an allowable span angle is reached and a new mesh cell is created. Curvature function also

affected by the relevance center option which provides general control over the full domain. If the relevance center is chosen as fine, the resulting element number will be high and solution accuracy increases in expense of CPU time and vice versa.

Apart from those, there has been another sizing imposed on the vane faces to increase calculation accuracy. For the vane faces 1 mm element size has been found suitable.

3.1.4 Inflation

Prediction inside the boundary layer is very important since it is closely related with the drag and lift calculations. However in order to reduce the time and cost, sometimes wall functions which don't require fine mesh inside the boundary layer may be utilized instead of calculating the boundary layer flow. It is the case for this study for some turbulence models (k-e and Spalart-Allmaras) and standard wall function option has been chosen to model boundary layer.

For the inflation option one of the most critical points is the y+ value selection since it indicates the height of the sub-layers inside the boundary layer normal to the wall. There are 3 sub-layers named as viscous sub-layer, buffer layer and logarithmic-law layer. Viscous sub-layer is where the viscous effects dominate the flow, logarithmic-law layer is the location of strong turbulent effects and the buffer layer is located between them that show the viscous and turbulent effects simultaneously. If calculation inside the boundary layer is desired, first layer height must be closer to the wall to be able to calculate the flow inside the boundary layer. If wall function is going to be used for modeling the flow inside boundary layer, there is no need for a fine mesh adjacent to the wall and y+ value is chosen accordingly.

There is a best practice regarding the meshing of the flow domain near the wall which states that y+ value must be between 1- 5 for full calculation near vanes and must be between 30 – 200 in case of wall function utilization as shown in Figure 3.2.

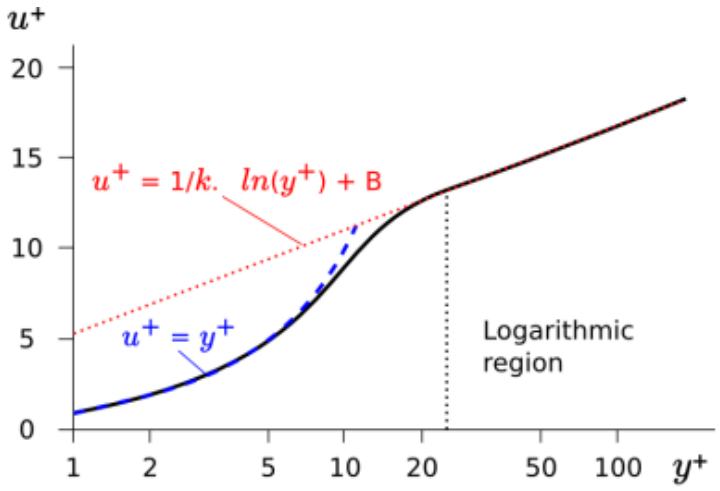

Figure 3.2: Law of wall

For this study, first layer thickness option has been preferred, since it maintains the inflation layer constant for the defined areas with the help of maximum layers and growth rate options. It is useful for keeping the y+ values under control which is vital for the accuracy of the solution.

Meshing has been performed utilizing pre algorithm, 5 layers for inflation with 1mm element size and 1.1 growth rate.

3.1.5 Boundary Conditions & Flow Domain

Flow domain of the problem includes the full nozzle geometry, thrust vectoring 4 vanes, far field for simulating the open atmosphere along lateral area of the extended portion in the direction of nozzle's longitudinal axis. Outlet condition has been defined as face that encloses the extended part. All of the employed boundary conditions have been explained in remainder of this section. Overall flow domain is shown in Figure 3.3.

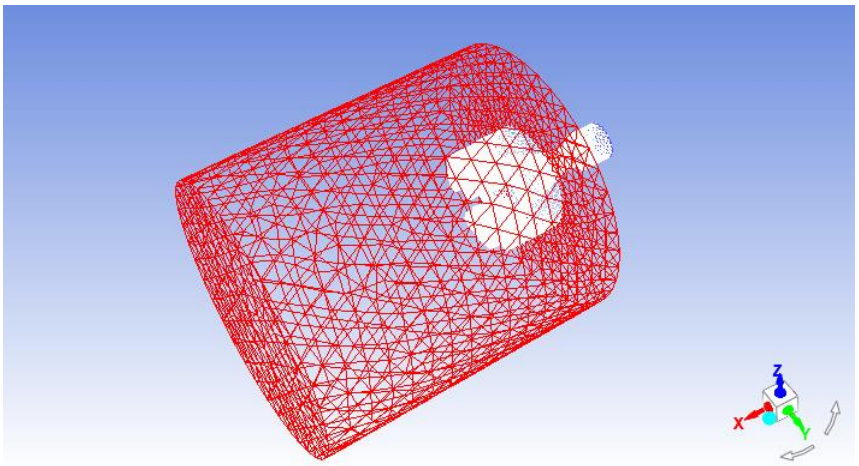

Figure 3.3: Fluid domain

Wall condition has been utilized extensively for the TVC and nozzle surfaces. This type of boundary used for bounding fluid and solid regions. Since the flow is viscous for this case no slip condition has been applied. No slip condition states that fluid particles touching the wall boundaries have no velocity. This situation has been explained in Figure 3.4 below.

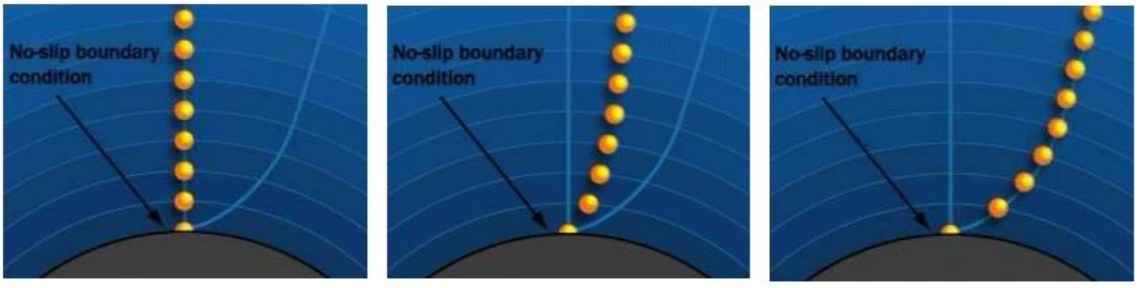

Figure 3.4: No Slip Condition

Farfield condition has also been employed for the analysis of TVC. This type of condition is available to the user only when density calculation is performed via ideal gas law. Free stream Mach number and static conditions are needed to be specified in

order to use this condition. It is employed for modeling free stream conditions for compressible flows at infinity as the name suggests.

In the meantime, pressure inlet condition is utilized when exact details of the flow are not known at the boundaries. In order to define this kind of boundary condition one must be familiar with the gauge/static pressure concept. Definitions of the absolute pressure and gauge pressure are given in Figure 3.5.

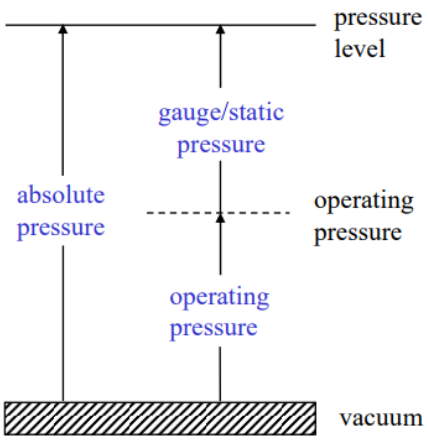

Figure 3.5: Absolute and Gauge Pressure

Pressure inlet boundary condition is suitable for both incompressible and compressible flows. The definition of the pressure inlet boundary condition for compressible flows is simply given as,

$$P_{total} = P_{static}\left(1 + \frac{k-1}{2}M^2\right)^{\frac{k}{k-1}} \tag{3.1}$$

In the Eq. 3.1, k specifies the ratio of specific heats (C_p/C_v) and M is Mach number. For this type of boundary condition flow direction must be specified in order not to get unphysical results. For compressible flows, total temperature must be also defined.

Pressure outlet model must be utilized whenever pressure inlet boundary is defined as inlet condition. This type of condition works with defined static pressure at the outlet. Static pressure can be defined in several ways such as specifying a radial equilibrium pressure distribution at the outlet boundaries for strongly swirling flows. Backflow can also occur during calculations. In that case, flow variables are inherited from inside of the flow domain.

All of the nozzle and vane faces have been modeled as wall. Pressure inlet and outlet have been defined in order to simulate engine exhaust gas and atmosphere conditions respectively. Pressure values for the inlet portion directly inherited from the test results and pressure value for the outlet has been obtained from atmosphere characteristics.

Periodic conditions might have been used in expense of interaction between the thrust vectoring vanes however it has been concluded that CPU power and memory is not that much of an issue, hence all four vanes have been included in the calculations. All of the nozzle and vane faces have been modeled as wall. Pressure inlet and outlet have been defined in order to simulate engine exhaust gas and atmosphere conditions respectively. Pressure values for the inlet portion directly inherited from the test results and pressure value for the outlet has been obtained from atmosphere characteristics.

Periodic conditions might have been used in expense of interaction between the thrust vectoring vanes however it has been concluded that CPU power and memory is not that much of an issue, hence all four vanes have been included in the calculations.

3.1.6 Mesh Quality & Specifications

Mesh quality is critical for the accuracy of the calculations. Therefore mesh element number is not an indication solely for a mesh to be eligible for an accurate calculation. Mesh elements themselves must satisfy some geometrical parameters for quality evaluation. These geometrical parameters can be names as skewness, expansion ratio and aspect ratio.

3.1.6.1 Skewness

Skewness of a mesh element is one of the main quality statistics and measures how close the element shape to the ideal is. In ANSYS, skewness value 1 indicates that the element is ideal and value 0 specifies the element as degenerate.

Skewness can be defined in two ways, one by equilateral volume of the cells and one based on the deviation from the normalized equilateral angle.

Equilateral volume based skewness can be defined as the ratio of difference between ideal and present cell size divided by ideal cell size. Schematic of the equilateral volume based skewness is given in Figure 3.6.

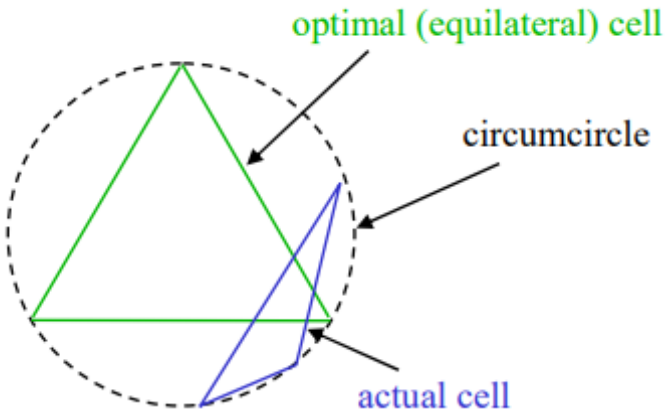

Figure 3.6: Equilateral Skewness Definition

While equilateral volume based skewness is very useful for triangular and tetrahedral elements, it is more suitable to use derivation from the normalized equilateral angle for the rectangular or hexahedral mesh elements. This kind of skewness is defined as in the Eq. 3.2;

$$max\left[\frac{\theta_{max}-90}{90}, \frac{90-\theta_{min}}{90}\right] \quad (3.2)$$

Schematic of the definition is also shown in Figure 3.7.

Figure 3.7: Skewness Definition via Normalized Equilateral Angle

Skewness values of the mesh that have been utilized in study have been shown in Figure 3.8.

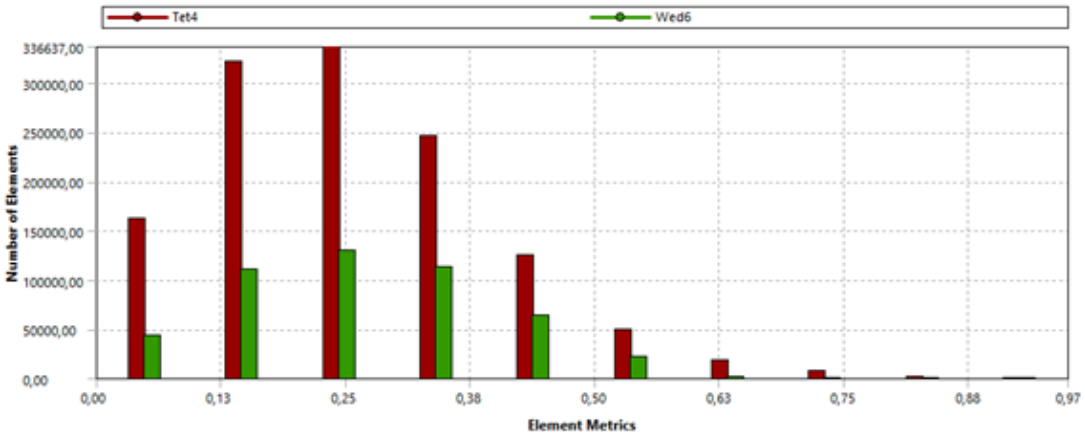

Figure 3.8: Skewness distribution

3.1.6.2 Expansion ratio (Smoothness)

Expansion ratio can be explained as the volume ratio of the adjacent elements. If the volume change rate between the cells is high, it may result in higher truncation errors therefore reduced accuracy. Schematic explanation is given in Figure 3.9.

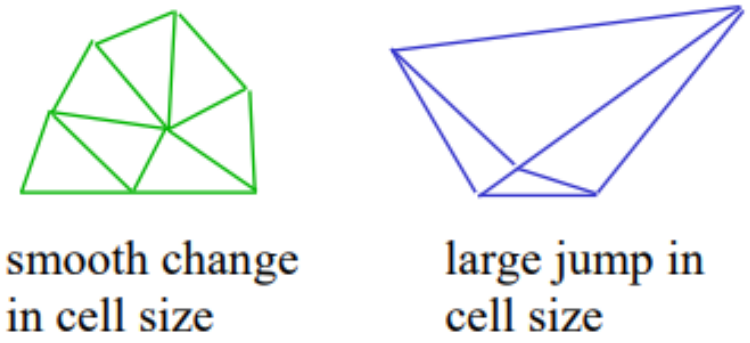

Figure 3.9: Expansion ratio

Unfortunately, there is no mesh quality control in ICEM regarding the expansion ratio. However, volume adaption method is present ANSYS ICEM CFD which gives the user the freedom for keeping the expansion ratio at desired levels. Volume adaption control has been employed via selecting the smoothing option to medium under the sizing group.

3.1.6.3 Aspect ratio

Aspect ratio is defined as indication of the cell stretching. Ratio of the longest edge to shortest edge gives the aspect ratio value of a mesh element. It is advised that, aspect ratio must be close to 1 as much as possible with the flows that have strong gradients. Schematic explanation of the aspect ratio is shown in Figure 3.10.

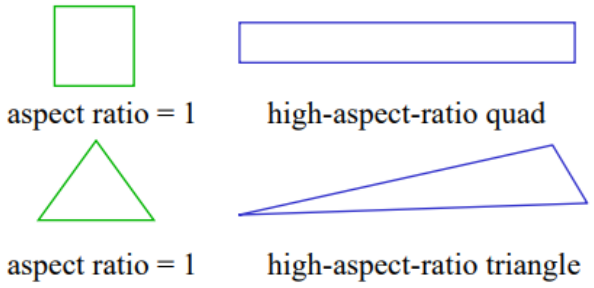

Figure 3.10: Aspect ratio

For this study, aspect ratio distribution of the cells has been given in Figure 3.11. Mesh is evaluated to be satisfactory in terms of aspect ratio.

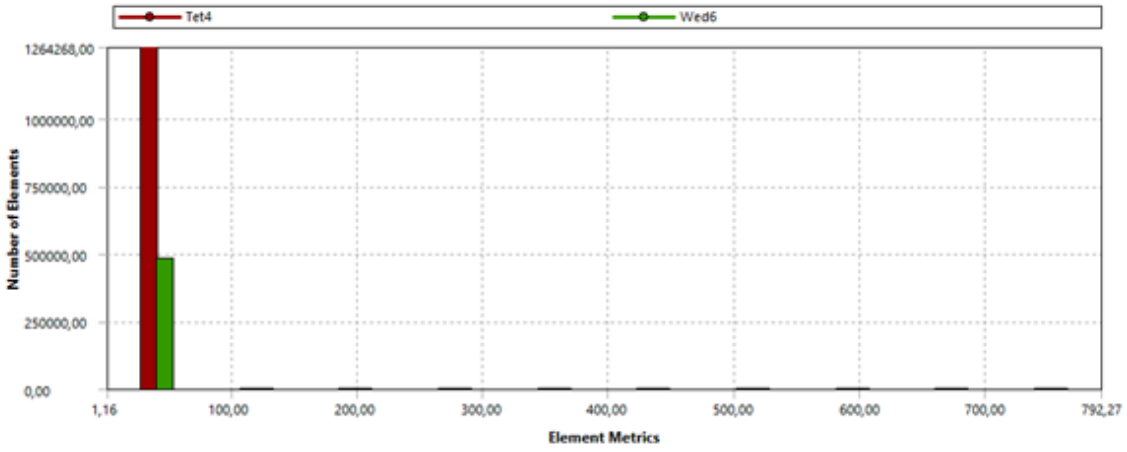

Figure 3.11: Aspect ratio distribution

3.2 Numerical Solution Scheme

There are two different main approaches to a CFD problem in terms of the numerical solution scheme which can be categorized as explicit and implicit. These two approaches differ in solving speed and accuracy however; there are cases that one is more advantageous than the other. For this reason, explicit and implicit approaches are closely studied before taking the problem head on.

For the implicit approach, equations for all of the nodes in the domain end up in a tri-diagonal matrix which is solved simultaneously for each time step. Thus, it requires more computational power and CPU time compared to explicit scheme generally. On the other hand explicit scheme usually is less stable and may not converge where implicit scheme converges without any problems.

Implicit approach utilizes the current state information of the problem to solve the current state while explicit approach uses the current state information of the problem

for solving the problem at the next time step, meaning for explicit approach, boundary conditions are lagging one step behind. If the problem has constant boundary conditions in time; then disadvantage of utilizing the explicit approach disappears.

Implicit approach generally utilized for its capability to solve problems with large time steps or in other words low frequency problems (e.g. steady state problems). Hence, disadvantage of numerical computations required for one step is compensated by dividing the problem into less time steps.

For all the reasons listed above, implicit solution scheme has been preferred for this study. All of the CFD calculations performed use the implicit solution scheme.

3.3 Solver Type

There are two types of solvers in Fluent which are known as density based and pressure based solvers. Developed algorithms of these solvers targeted for different Mach Number ranges which are 0-0,3 range for pressure based and 0.3 being the lower limit for density based solver. Even though, Mach number range for both have become widened with the support of developed corrections over the years, density based solver is still the sensible choice for compressible fluid flows.

There are a few differences regarding calculation methods and utilized equations between these solvers. In the density based approach, momentum, continuity and energy equations solved simultaneously while other scalars or turbulence model parameters are calculated at a later step. For this solver, explicit and implicit schemes are available to use whereas pressure based solvers are only implicit.

Pressure based solvers are split into two branches which are segregated and coupled solvers. These solvers perform calculations on pressure correction equation to solve flow field which is derived from mass and momentum equations.

For this work, density based coupled solver has been preferred since it is stated that "The density-based coupled solver (DBCS) is applicable when there is a strong coupling, or interdependence, between density, energy, momentum, and/or species." by the ANSYS user manual which covers the case in this study. Detailed information about this matter can be found in ANSYS user manual.

Flow charts of the density based and pressure based solvers have been shown in Figure 3.12.

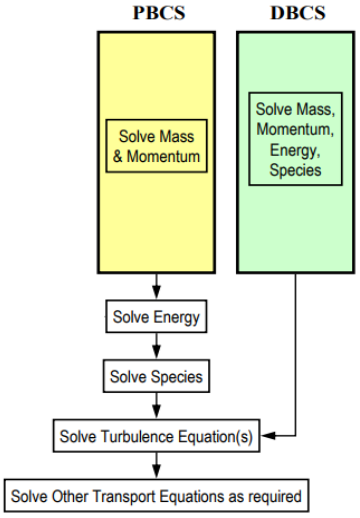

Figure 3.12: Density and pressure based solution algorithms [Introductory Fluent Training, n.d.]

Density based solver convective flux setting has been chosen as AUSM (advection upstream Splitting Method) which actually is a hybrid flux convection scheme consisting of Flux Vector Splitting and Flux Difference Splitting methods. It has taken the best of both worlds in terms of accuracy and reliability. For this reason AUSM has been utilized for the analyses in the scope of this study.

3.4 Flow Model

Flow model selection has been carried out beforehand in order to reduce computing time avoiding trial and error type approach. The options have been narrowed down to Reynolds Averaged Navier Stokes (RANS) and Unsteady Reynolds Averaged Navier Stokes (URANS) calculations. Large Eddy Simulation (LES) or Direct Numerical Simulation (DNS) obviously require much more computing power than what is affordable for this study. RANS calculations performed for different turbulence models and grid quality to determine the setup for URANS calculations.

Before performing the calculations, RANS theory and limitations must be known in order not to jump to wrong conclusions. RANS basically decomposes the variables in the instantaneous Navier Stokes Equation to mean and fluctuating values. Substituting this decomposed terms into instantaneous NS equations and continuity equations gives the ensemble (time) averaged equations for a CFD calculation. However substituting also results in a stress tensor named as Reynolds Stress Tensor producing more unknown variables for 3D calculations. That is the point where turbulence models come into play. Closure of RANS model is possible with Bousssinesq approach or solving the transport equations in the Reynolds Stress Tensor with an added transport equation for scale determination. Even though Boussinesq Approach reduces the computing cost in a great manner, isotropic turbulence assumption does not perform well for free shear flows like jet flows or mixing layers as opposed to the Reynolds Stress Models (RSM).

Turbulent 3D URANS is also one of the models that have been evaluated before choosing the flow model. URANS calculations are very similar to RANS calculations with only one exception: Time dependent terms exist in the momentum and continuity equations. They are not omitted from these equations unlike the RANS calculations. Thus, if a mean velocity is time dependent, the effects of this velocity on the fluid domain can be predicted with URANS approach.

URANS is not a very accurate unsteady flow solver; however it may show the implications of an unsteady behavior in the fluid domain and predict the mean variable changes making this approach better choice than RANS if sufficient computational power exists.

All of above considered thoroughly and turbulent 3D RANS flow model has been chosen to be the primary performance prediction tool of the thrust vectoring vanes for this study. At the end of the day, 3D RANS model is determined to satisfy required accuracy while maintaining affordable time cost of analysis.

3.4.1 Theory of Reynolds Averaged Navier-Stokes

Reynolds Averaged Navier-Stokes equations obtained via time averaging Navier-Stokes equations. To be able to perform the time averaging, momentary values in the equation are decomposed into the mean and fluctuating values. Graphical description of the mentioned decomposition has been given in Figure 3.13.

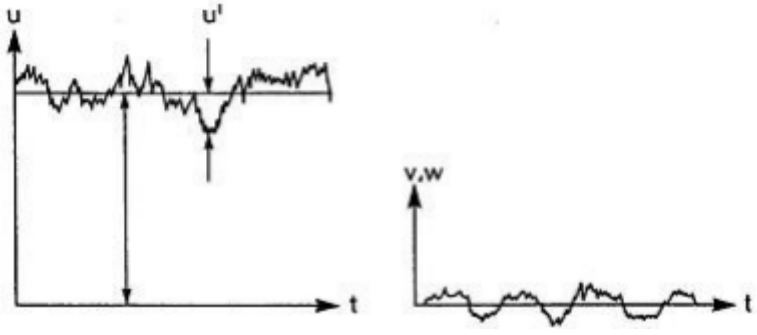

Figure 3.13: Decomposition of mean and fluctuating velocity

Decomposition of the momentary velocity in the x direction which is denoted as u will be performed as an example. Time averaged value of the u is shown with $\bar{u}$ and the fluctuating term is written as u'. Same principle is utilized for all of the terms in the Navier Stokes equation which results in Eq. 3.3 for continuity is shown below.

$$\frac{\partial \bar{u}}{\partial x}+\frac{\partial u'}{\partial x}+\frac{\partial \bar{v}}{\partial y}+\frac{\partial v'}{\partial y}+\frac{\partial \bar{w}}{\partial z}+\frac{\partial w'}{\partial z}=0 \tag{3.3}$$

Time averaged version of the Equation above has been given in Eq. 3.4.

$$\overline{\frac{\partial \bar{u}}{\partial x}+\frac{\partial u'}{\partial x}+\frac{\partial \bar{v}}{\partial y}+\frac{\partial v'}{\partial y}+\frac{\partial \bar{w}}{\partial z}+\frac{\partial w'}{\partial z}}=0 \tag{3.4}$$

After time averaging has been performed on continuity equation, it transfers into equation given below.

$$\frac{\partial \bar{u}}{\partial x}+\frac{\partial \bar{v}}{\partial y}+\frac{\partial \bar{w}}{\partial z}=0 \tag{3.5}$$

Note that the averaging method takes the mean values at a fixed place in space. Additionally time span of the averaging is assumed to be long enough for mean values to be independent of it. This situation has been formulated as,

$$\bar{u}=\frac{1}{\Delta t}\int_{t_0}^{t_0+t_1} u\,dt \tag{3.6}$$

The same procedure applied to the momentum equation. In order to summarize the idea only momentum equation in the x direction is given below;

$$\overline{\rho\left\{\frac{\partial(\bar{u}+u')}{\partial t}+\frac{\partial(\bar{u}+u')^2}{\partial x}+\frac{\partial(\bar{u}+u')(\bar{v}+v')}{\partial y}+\frac{\partial(\bar{u}+u')(\bar{w}+w')}{\partial z}\right\}}$$
$$=\overline{F_x-\frac{\partial(\bar{\rho}+p')}{\partial x}+\mu\left(\frac{\partial^2(\bar{u}+u')}{\partial x^2}+\frac{\partial^2(\bar{u}+u')}{\partial y^2}+\frac{\partial^2(\bar{u}+u')}{\partial z^2}\right)} \tag{3.7}$$

Which result in three directions as,

$$\rho\left(\frac{\partial \bar{u}}{\partial t}+\bar{u}\frac{\partial \bar{u}}{\partial x}+\bar{v}\frac{\partial \bar{u}}{\partial y}+\bar{w}\frac{\partial \bar{u}}{\partial z}\right)=F_x-\frac{\partial \bar{\rho}}{\partial x}+\mu\Delta\bar{u}-\rho\left(\frac{\partial\overline{u'u'}}{\partial x}+\frac{\partial\overline{u'v'}}{\partial y}+\frac{\partial\overline{u'w'}}{\partial z}\right) \tag{3.8}$$

$$\rho\left(\frac{\partial\bar{v}}{\partial t}+\bar{u}\frac{\partial\bar{v}}{\partial x}+\bar{v}\frac{\partial\bar{v}}{\partial y}+\bar{w}\frac{\partial\bar{v}}{\partial z}\right)=F_y-\frac{\partial\bar{\rho}}{\partial y}+\mu\Delta\bar{v}-\rho\left(\frac{\partial\overline{u'v'}}{\partial x}+\frac{\partial\overline{v'v'}}{\partial y}+\frac{\partial\overline{v'w'}}{\partial z}\right) \quad (3.9)$$

$$\rho\left(\frac{\partial\bar{w}}{\partial t}+\bar{u}\frac{\partial\bar{w}}{\partial x}+\bar{v}\frac{\partial\bar{w}}{\partial y}+\bar{w}\frac{\partial\bar{w}}{\partial z}\right)=F_z-\frac{\partial\bar{\rho}}{\partial z}+\mu\Delta\bar{w}-\rho\left(\frac{\partial\overline{u'w'}}{\partial x}+\frac{\partial\overline{v'w'}}{\partial y}+\frac{\partial\overline{w'w'}}{\partial z}\right) \quad (3.10)$$

Or in tensor form, these equations can be written as,

$$\rho\frac{D\overline{u_\iota}}{Dt}=F_i-\frac{\partial\bar{\rho}}{\partial x_i}+\mu\Delta\overline{u_\iota}-\rho\left(\frac{\partial\overline{u_i^{'}u_j^{'}}}{\partial x_j}\right) \quad (3.11)$$

The last term in Eq. 3.11 named as Reynolds stress term and can be written as,

$$\mu\Delta u_i-\rho\left(\frac{\partial\overline{u_i^{'}u_j^{'}}}{\partial x_j}\right)=\mu\frac{\partial}{\partial x_j}\left(\frac{\partial u_i}{\partial x_j}\right)-\rho\frac{\partial}{\partial x_j}\left(\overline{u_i^{'}u_j^{'}}\right)=\frac{\partial}{\partial x_j}\left(\mu\frac{\partial u_i}{\partial x_j}-\rho\overline{u_i^{'}u_j^{'}}\right) \quad (3.12)$$

Expression in the brackets is known as total shear stress. If tensor forms of the original Navier-Stokes equation and time averaged version are compared it can be seen that terms in the brackets arise due to time averaging. Navier-Stokes without time averaging is given for comparison in Eq. 3.13.

$$\rho\frac{D\overline{u_\iota}}{Dt}=F_i-\frac{\partial\rho}{\partial x_i}+\mu\Delta u_i \quad (3.13)$$

Reynolds stress term is mostly dominant for a wide range of flow types. In order to complete the model, this arisen term must be solved. This is possible thanks to Boussinesq approach which provided the closure. In tensor form, time averaged equation with Boussinesq approach is given below; Note that, the velocity terms are not shown with superscript from now on for the simplicity.

$$\rho\left(\frac{D\overline{u_\iota}}{Dt}\right)=F_i-\frac{\partial\rho}{\partial x_i}+\frac{\partial}{\partial x_i}\tau_{ij} \quad (3.14)$$

where;

$$\tau_{ij} = \mu \frac{\partial u_i}{\partial x_j} + \rho \left(v_T \left(\frac{\partial u_i}{\partial x_j} + \frac{\partial u_j}{\partial x_i} \right) - \frac{2}{3} k \delta_{ij} \right)$$

3.5 Turbulence Models

Different types of turbulence models have been put to use and their performances are compared for the case. All of them are practical and used by the designers around the world often. Their accuracy is compared over different cases and the advantages and disadvantages of these models are closely studied. Despite the fact that, turbulence model determination could be concluded with a literature survey, all of the listed turbulence models have been tested for this study' s case and results are discussed extensively. Note that, all the tested models have employed Boussinesq approach for the sake of reduced CPU power required.

3.5.1 Spalart-Allmaras Turbulence Model

Spalart-Allmaras is a relatively simple, easy to implement and widely utilized model. Because of the advantages, feasibility of using this model is thoroughly evaluated by the writer.

3.5.1.1 Theory of Spalart-Allmaras turbulence model

Spalart Allmaras turbulence model utilizes only 1 transport equation which calculates the transport of turbulent kinematic viscosity$\tilde{v}$. This equation can be seen below.

$$\frac{\partial}{\partial t}(\rho\tilde{v}) + \frac{\partial}{\partial t}(\rho\tilde{v}u_i) = G_v + \frac{1}{\sigma\tilde{v}}\left[\frac{\partial}{\partial x_j}\left\{(\mu + \rho\tilde{v})\frac{\partial\tilde{v}}{\partial x_j}\right\} + C_{b2}\rho\left(\frac{\partial\tilde{v}}{\partial x_j}\right)^2\right] - Y_v + S_{\tilde{v}} \qquad (3.15)$$

The first term on RHS in Eq. 3.13 defines time rate change of turbulent kinematic viscosity, second term describes the transport of the kinematic turbulent viscosity by convection. As for the LHS, G_v is named as generation of turbulent viscosity; Y_v specifies the destruction of turbulent viscosity near walls by blocking and viscous

damping. $\sigma_{\tilde{v}}$ and C_{b2} are modeling constants whereas, *v* is molecular kinematic viscosity and $S_{\tilde{v}}$ user defined source term. G_v can be calculated as;

$$G_v = C_{b1}\rho\tilde{S}\tilde{v} \tag{3.16}$$

where;

$$\tilde{S} \equiv S + \frac{\tilde{v}}{k^2 d^2} f_{v2} \qquad and \qquad f_{v2} = 1 - \frac{X}{1 + X f_{v1}}$$

C_{b1} and *k* are model constants, *d* is the distance from wall and *S* is a scalar measure of deformation tensor which is based on the vorticity magnitude and defined as follows,

$$S \equiv \sqrt{2\Omega_{ij}\Omega_{ij}} \tag{3.17}$$

Ω_{ij} is mean rate of rotation tensor shown in Eq. 3.18.

$$\Omega_{ij} = \frac{1}{2}\left(\frac{\partial u_i}{\partial x_j} - \frac{\partial u_j}{\partial x_i}\right) \tag{3.18}$$

Turbulent viscosity has been obtained as in Eq. 3.19 where; viscous damping function f_{v1} has been used in.

$$\mu_t = \rho\tilde{v} f_{v1} \tag{3.19}$$

where;

$$f_{v1} = \frac{X^3}{X^3 + C_{v1}^3} \qquad and \qquad X \equiv \frac{\tilde{v}}{v}$$

Original model does not take effects of mean strain rate into account for generation of turbulence production however; FLUENT includes a modified version of the model which calculates the deformation tensor as follows,

$$S \equiv |\Omega_{ij}| + C_{prod}\, min\left(0, |S_{ij}| - |\Omega_{ij}|\right) \tag{3.20}$$

where; the prod coefficient and the mean strain rate has been defined respectively as stated below.

$$C_{prod} = 2.0 \qquad |\Omega_{ij}| \equiv \sqrt{2\Omega_{ij}\Omega_{ij}} \qquad S_{ij} \equiv \sqrt{2\Omega_{ij}\Omega_{ij}} \tag{3.21}$$

$$S_{ij} = \frac{1}{2}\left(\frac{\partial u_i}{\partial x_j} + \frac{\partial u_j}{\partial x_i}\right) \tag{3.22}$$

Turbulent destruction Y_v has been provided as follows for this modified version of the model.

$$Y_v = C_{w1}\rho f_w \left(\frac{\tilde{v}}{d}\right)^2 \tag{3.23}$$

where,

$$f_w = g\left[\frac{1 + C_{w3}^6}{g^6 + C_{w3}^6}\right]^{1/6} \qquad g = r + C_{w2}(r^6 - r) \qquad r \equiv \frac{\tilde{v}}{\tilde{S}k^2d^2}$$

$C_{\omega1}$, $C_{\omega2}$ and $C_{\omega3}$ are model constants, and the expression for $\tilde{S}$ has been given before in Eq. 3.16. Values of all model constants as provided by FLUENT have been given below.

$$C_{b1} = 0.1355 \quad C_{b2} = 0.622 \quad \sigma_{\tilde{v}} = \frac{2}{3} \qquad C_{v1} = 7.1$$

$$C_{w1} = \frac{C_{b1}}{k^2} + \frac{(1 + C_{b2})}{\sigma_{\tilde{v}}} \qquad C_{w2} = 0.3 \qquad C_{w3} = 2.0 \qquad k = 0.4187$$

3.5.1.2 Best practice and comments for Spalart-Allmaras

Spalart-Allmaras turbulence model utilizes only one transport equation which calculates the turbulent viscosity to include turbulence effects [Bakker, 2005]. Length scale of the

local shear layer thickness is calculated for this model. Another good aspect of this model is its less sensitive structure to numerical error if non-layered mesh is utilized near walls.

Although this model is not all around purpose model, it gives very reliable results with wall bounded flows or boundary flows with adverse pressure gradients [ANSYS, 2015].

It is also known to be used in turbomachinery field extensively. However this model is not very good at predicting flows with free shear such as jet flows. For the case of this study, Spalart-Allmaras model yielded satisfactory results at low angle of attack however results of high angle of attack were poor.

3.5.2 Realizable K-ε Turbulence Model

In order to evaluate the realizable k-ε model, one must know standard k-e model specifications. Standard version is a two-equation model with assumption of fully turbulent flow and based on calculation of turbulent kinetic energy (k) and dissipation rate (ε) transport equations. Turbulent kinetic energy is mathematically derived however dissipation rate is obtained using empirical data. Hence, standard k-ε model is a semi empirical model.

3.5.2.1 Theory of realizable K- ε turbulence model

The equations defining the standard k-ε model can be seen in Eq. 3.24 and Eq. 3.25 below. Note that this is standard k-e model which does not include all the terms that are found in exact k-ε model equation.

Transport equation for turbulent kinetic energy has been defined as,

$$\frac{\partial(\rho k)}{\partial t}+\frac{\partial(\rho k u_i)}{\partial x_i}=\frac{\partial}{\partial x_j}\left[\frac{\mu_t}{\sigma_k}\frac{\partial k}{\partial x_j}\right]+2\mu_t E_{ij}E_{ij}-\rho\varepsilon \tag{3.24}$$

The transport equation for the dissipation rate has been shown as,

$$\frac{\partial(\rho\varepsilon)}{\partial t}+\frac{\partial(\rho\varepsilon u_i)}{\partial x_i}=\frac{\partial}{\partial x_j}\left[\frac{\mu_t}{\sigma_\varepsilon}\frac{\partial\varepsilon}{\partial x_j}\right]+C_{1\varepsilon}\frac{\varepsilon}{k}2\mu_t E_{ij}E_{ij}-C_{2\varepsilon}\rho\frac{\varepsilon^2}{k} \quad (3.25)$$

E_{ij} is component of rate of deformation. μ_t is turbulent viscosity and expressed as $\mu_t=\rho C_\mu k^2/\varepsilon$. The terms of σ_ε σ_k $C_{1\varepsilon}$ $C_{2\varepsilon}$ C_μ are the empirical constants which have been obtained via data fitting.

The first terms on LHS of the two equations given above specifies the rate of change of the two variables k and e. The second terms defines the transport of k and ε via convection. As for the RHS, last term means the rate of destruction of k and ε. The second and first terms on the LHS state the rate of production and transport by diffusion of k and epsilon respectively.

Realizable k-epsilon model utilizes different terms for the calculation of turbulent kinetic energy and a different transport equation for epsilon. The model is called realizable because it employs a variable C_μ whereas standard model utilizes constant one which means it satisfies variety of mathematical aspects as opposed to the standard model. Transport equations for k and epsilon have been given in Eq. 3.26 and Eq. 3.27.

$$\frac{\partial}{\partial t}(\rho k)+\frac{\partial}{\partial x_i}(\rho k u_i)=\frac{\partial}{\partial x_j}\left[\left(\mu+\frac{\mu_t}{\sigma_k}\right)\frac{\partial k}{\partial x_j}\right]+P_k+P_b-\rho\varepsilon-Y_M+S_k \quad (3.26)$$

$$\frac{\partial}{\partial t}(\rho\varepsilon)+\frac{\partial}{\partial x_i}(\rho\varepsilon u_i)=\frac{\partial}{\partial x_j}\left[\left(\mu+\frac{\mu_t}{\sigma_\varepsilon}\right)\frac{\partial\varepsilon}{\partial x_j}\right]+\rho C_1 S\varepsilon-\rho C_2\frac{\varepsilon^2}{k+\sqrt{\nu\varepsilon}}+C_{1\varepsilon}\frac{\varepsilon}{k}C_{3\varepsilon}P_b+S_\varepsilon \quad (3.27)$$

P_k (G_k) and P_b (G_b) in the turbulent kinetic energy transport equation describe the generation of turbulent kinetic energy because of mean velocity gradients and buoyancy. S_k and S_e terms are source terms that are defined by the user. In addition to that Y_M is utilized for the fluctuating dilation in compressible turbulence which is a part of overall dissipation rate. Production of turbulent kinetic energy G_k, the modulus of mean-rate strain tensor S and generation of turbulent kinetic energy on account of buoyancy G_k have been given in Eq. 3.28.

$$G_k = -\rho\overline{u_\iota{}' u_j{}'}\frac{\partial u_j}{\partial x_i} \qquad S = \sqrt{2S_{ij}S_{ij}} \qquad G_b = \beta g_i \frac{\mu_t}{\mathrm{Pr_t}}\frac{\partial \mathrm{T}}{\partial \mathrm{x_i}} \tag{3.28}$$

As for the epsilon transport equation, the first term on the RHS specifies diffusion of epsilon; second term is for the generation of epsilon whereas third and fourth terms are used for destruction of epsilon and buoyancy effects respectively. S_ε is the user defined source term. Calculation of turbulent viscosity is performed as follows;

$$\mu_t = \rho C_\mu \frac{k^2}{\varepsilon} \tag{3.29}$$

where;

$$C_\mu = \frac{1}{A_0 + A_s\frac{kU^*}{\varepsilon}} \qquad U^* = \sqrt{S_{ij}S_{ij} + \widetilde{\Omega_{\iota j}}\widetilde{\Omega_{\iota j}}} \qquad \widetilde{\Omega_{\iota j}} = \overline{\Omega_{\iota j}} - \varepsilon_{ijk}\omega_k - 2\varepsilon_{ijk}\omega_k$$

$\overline{\Omega_{\iota j}}$ is the mean rate of rotation tensor observed in rotating reference frame with angular velocity ω_k. The constants in Eq. 3.29 are defined as;

$$A_0 = 4.04 \qquad A_s = \sqrt{6}\cos\varphi$$

where;

$$\varphi = \frac{1}{3}\cos^{-1}\left(\sqrt{6}\frac{S_{ij}S_{jk}S_{ki}}{\tilde{S}^3}\right) \qquad \tilde{S} = \sqrt{S_{ij}S_{ij}} \qquad S_{ij} = \frac{1}{2}\left(\frac{\partial u_i}{\partial x_j} + \frac{\partial u_j}{\partial x_i}\right)$$

As mentioned before C_μ is proved to be a function of mean strain and mean rotation rates. The constants belong to this model has been given as follows by previous studies [Shih, 1995].

$$\mathrm{C_{1\varepsilon}} = 1.44 \qquad \mathrm{C_2} = 1.9 \qquad \sigma_\mathrm{k} = 1.0 \quad \sigma_\varepsilon = 1.2$$

3.5.2.2 Best practice and comments for realizable K- ε

Realizable k-ε model is an improved version of the standard k-ε model. As known by many, standard k-ε is a very economical way of predicting performance even though it has limitations. One of those limitations is accurate modeling of the dissipation rate. For this reason realizable k-ε model has been developed. Dissipation rate is reformed over standard model to be based on dynamic equation of the mean-square vortices fluctuation [ANSYS, 2015]. While newly developed dissipation rate equation improves the model, it is still not advised to use realizable k-e model with both rotational and stationary fluid domains instantaneously (rotating sliding mesh, multiple reference frames etc.) since it generates unrealistic turbulent viscosities.

3.5.3 K-ω Turbulence Model

K-ω turbulence model also utilizes two transport equations for the turbulent kinetic energy and dissipation rate, however dissipation rate has been named as specific dissipation rate (ω) and defined as the ratio of "ε" to" k".

3.5.3.1 Theory of K-ω turbulence model

Transport equations for k and ω are given in Eq. 3.30 and Eq. 3.31.

$$\frac{\partial}{\partial t}(\rho k) + \frac{\partial}{\partial x_i}(\rho k u_i) = \frac{\partial}{\partial x_i}\left[\left(\mu + \frac{\mu_t}{\sigma_k}\right)\frac{\partial k}{\partial x_j}\right] + G_k - Y_k + S_k \tag{3.30}$$

$$\frac{\partial}{\partial t}(\rho \omega) + \frac{\partial}{\partial x_i}(\rho \omega u_i) = \frac{\partial}{\partial x_j}\left[\left(\mu + \frac{\mu_t}{\sigma_\omega}\right)\frac{\partial \omega}{\partial x_j}\right] + G_\omega - Y_\omega + S_\omega \tag{3.31}$$

The terms in Eq. 3.30 and Eq. 3.31 can be explained in a similar fashion with the k-epsilon model equations. First and second terms on the LHS are time rate change and transport by convection of the related parameters respectively. First term on the RHS is transport by diffusion whereas G_k and G_w represents generation of the k and omega due

to mean velocity gradients. Y_k and Y_w are the dissipation terms while S_k and S_w being the source terms defined according to the application. In addition to that, α_k and α_w are turbulent Prandtl numbers. The turbulent viscosity has been defined as;

$$\mu_t = \alpha^* \frac{\rho k}{\omega} \tag{3.32}$$

Where α^* is damping coefficient. This coefficient is used for low Reynolds Number flows to damp the turbulent viscosity. Definition of α* is in Eq. 3.33 below.

$$\alpha^* = \alpha^*_\infty \left(\frac{\alpha^*_0 + \mathrm{Re_t}/\mathrm{R_k}}{1 + \mathrm{Re_t}/\mathrm{R_k}} \right) \tag{3.33}$$

Definition of Yk and Yw has been given as;

$$Y_k = \rho \beta^* f_{\beta^*} k\omega \qquad Y_\omega = \rho \beta f_\beta \omega^2 \tag{3.34}$$

where;

$$\mathrm{Re_t} = \frac{\rho \mathrm{k}}{\mu \omega} \quad \mathrm{R_k} = 6 \quad \alpha^*_0 = \frac{\beta_\mathrm{i}}{3} \quad \beta_\mathrm{i} = 0.072$$

α* and α^*_∞ are equal to 1 for high Reynolds number for standard k-omega model and since the case for this study is same, this value can be used in here.

3.5.3.2 Best practice and comments for K- ω

Although there have been improvements for this model, it is still not advised to be used for free shear flows just like k-e model. Moreover, with this model, solution is sensitive to the effects of k and w parameters calculated outside the shear layer [ANSYS, 2015]. K-ω model is also known to be over predicting the flow separation [Wasserman, 2016].

On the other hand k-ω performs very well for complex boundary layers with adverse pressure gradients. This model can also be utilized for the boundary layer flows

eliminating the need for a wall function. However eliminating wall function means more refined mesh must be utilized near walls.

3.5.4 SST k-ω Turbulence Model

3.5.4.1 Theory of SST K-ω turbulence model

SST k-ω model is created utilizing standard k-ω model and a transformed k-epsilon model [Menter, 1994]. The model accounts the effects of principal turbulent shear stresses when calculating the turbulent viscosity. Apart from that, the model also includes a cross diffusion term in w transport equation and blending function to trigger k-epsilon model in free stream and k-ω model inside wall boundary layer. Transport equations of k and omega of this model have been given in Eq. 3.35 and Eq. 3.36 below.

$$\frac{\partial}{\partial t}(\rho k) + \frac{\partial}{\partial x_i}(\rho k u_i) = \frac{\partial}{\partial x_j}\left[\left(\mu + \frac{\mu_t}{\sigma_k}\right)\frac{\partial k}{\partial x_j}\right] + \widetilde{G_k} - Y_k + S_k \tag{3.35}$$

$$\frac{\partial}{\partial t}(\rho \omega) + \frac{\partial}{\partial x_i}(\rho \omega u_i) = \frac{\partial}{\partial x_j}\left[\left(\mu + \frac{\mu_t}{\sigma_\omega}\right)\frac{\partial \omega}{\partial x_j}\right] + G_\omega - Y_\omega + D_w + S_\omega \tag{3.36}$$

All of the terms are nearly same with only modified generation of turbulent kinetic energy term in the k transport equation that is symbolized via $\widetilde{G_k}$ and added term of cross diffusion which is denoted by D_w. $\widetilde{G_k}$ can be obtained as,

$$\widetilde{G_k} = min(G_k, 10\rho\beta^* k\omega) \tag{3.37}$$

G_k term in the equation is calculated as same as the original k-ω model. G_w term is determined by using the equation below,

$$G_w = \frac{\alpha}{v_t} G_k \tag{3.38}$$

Y_k and Y_w terms are calculated in the same fashion with the standard model with the only difference of taking $f_\beta$and f_{β^*} as constant and equal to 1. Eq. 3.39 presents the turbulent viscosity parameter.

$$\mu_t = \frac{\rho k}{\omega} \frac{1}{max\left[\frac{1}{\alpha^*}, \frac{SF_2}{a_1 \omega}\right]} \tag{3.39}$$

S is strain rate magnitude and α^* is the damping coefficient which is given previously in the standard model section. Another difference of the SST model from the standard model is calculation procedure of the Prandtl Numbers which include F_1 and F_2 blending functions to trigger the model equations near wall and free stream.

$$\sigma_k = \frac{1}{\frac{F_1}{\alpha_{k,1}} + \frac{(1-F_1)}{\alpha_{k,2}}} \tag{3.40}$$

$$\sigma_k = \frac{1}{\frac{F_1}{\alpha_{\omega,1}} + \frac{(1-F_1)}{\alpha_{\omega,2}}} \tag{3.41}$$

where;

$$F_1 = \tanh(\phi_1^4) \qquad F_1 = \tanh(\phi_2^4)$$

The cross diffusion term which blends the standard k-e model with standard k-ω model is defined as below.

$$D_w = 2(1 - F_1)\rho\alpha_{w,2} \frac{1}{\omega} \frac{\partial \mathrm{k}}{\partial \mathrm{x_j}} \frac{\partial \omega}{\partial \mathrm{x_j}} \tag{3.42}$$

The constants utilized for SST k-ω can be stated as follows.

$$\sigma_{\omega,1} = 2.0 \quad \sigma_{\omega,2} = 1.168 \quad \sigma_{k,1} = 1.176 \quad \sigma_{k,2} = 1.0 \quad a_1 = 0.31$$

3.5.4.2 Best practice and comments for SST K- ω

Free stream sensitivity of k-w and lack of proper flow separation prediction for k-e model is known problems which are both addressed in the previous sections. In order to overcome these problems, SST k-w model has been created to merge the accuracy of k-w model near walls and the accuracy of k-e model in free stream. SST k-w model is very similar to the standard k-w model from many viewpoints with few differences which include utilization of damped cross-diffusion derivative term in w equation, modified turbulent viscosity term to account for the transport of turbulent shear stress and different modeling constants [Bakker, 2005].

3.5.5 Transition-SST Turbulence Model

Transition SST Model, simply is an improved version of SST k-w model for the transitioning flows. Background of this model is explained below.

3.5.5.1 Theory of transition SST turbulence model

Transition-SST turbulence model utilizes two more equations which are created for intermittency and transition momentum thickness as well as modifying the k equation of SST k-w model. Transport equation for the k for this model has been given below.

$$\frac{\partial}{\partial \mathrm{t}}(\rho \mathrm{k}) + \frac{\partial}{\partial \mathrm{x_i}}(\rho \mathrm{k u_i}) = \frac{\partial}{\partial \mathrm{x_j}}\left[\Gamma_k \frac{\partial \mathrm{k}}{\partial \mathrm{x_j}}\right] + G_k^* - Y_k^* + S_k \qquad (3.43)$$

where;

$$G_k^* = Y_{eff}\tilde{G}_k$$

$$Y_k^* = min\big(max\big(Y_{eff}, 0.1\big), 1.0\big)Y_k$$

Definition of the $\widetilde{G_k}$ and Y_k has been given in section 3.5.4 and 3.5.3 respectively. Note that the omega equation is unaltered, however additional two transport equations for

intermittency and momentum thickness is used in this model. Eq. 3.44 presents the intermittency equation.

$$\frac{\partial}{\partial t}(\rho\gamma) + \frac{\partial}{\partial x_j}(\rho U_j \gamma) = P_{\gamma 1} - E_{\gamma 1} + P_{\gamma 2} - E_{\gamma 2} + \frac{\partial}{\partial x_j}\left[\left(\mu + \frac{\mu_t}{\sigma_\gamma}\right)\frac{\partial \gamma}{\partial x_j}\right] \tag{3.44}$$

And the transition sources are,

$$P_{\gamma 1} = C_{a1} F_{length} \rho S[\gamma F_{onset}]^{C_{\gamma 3}} \tag{3.45}$$

$$E_{\gamma 1} = C_{e1} P_{\gamma 1} \gamma \tag{3.46}$$

F_{length} is a function that determines the transition region length while S is the strain rate and C_{a1}, C_{e2} constants with the value of 2 and 1 respectively. Destruction or delaminarization sources are given as,

$$P_{\gamma 2} = C_{a2} \rho \Omega \gamma F_{turb} \tag{3.47}$$

$$E_{\gamma 2} = C_{e2} P_{\gamma 2} \gamma \tag{3.48}$$

Ω is the vorticity magnitude. Transition onset is controlled by the functions given below.

$$Re_v = \frac{\rho y^2 S}{\mu} \tag{3.49}$$

$$R_T = \frac{\rho k}{\mu \omega} \tag{3.50}$$

$$F_{onset1} = \frac{Re_v}{2.193 Re_{\theta_c}} \tag{3.51}$$

$$F_{onset2} = \min(\max(F_{onset1}, F_{onset1}^4), 2.0) \tag{3.52}$$

$$F_{onset3} = \max\left(1 - \left(\frac{R_T}{25}\right)^3, 0\right) \tag{3.53}$$

$$F_{onset} = \max(F_{onset2} - F_{onset3}, 0) \tag{3.54}$$

$$F_{turb} = e^{-\left(\frac{R_T}{4}\right)^4} \tag{3.55}$$

Where $Re_{\theta c}$ is critical Reynolds Number that intermittency begin to increase inside the boundary layer and y is the wall distance. $R\tilde{e}_{\theta t}$ is the transition Reynolds Number which has been located downstream of $Re_{\theta c}$ and correlation between $Re_{\theta c}$ and $R\tilde{e}_{\theta t}$ obtained via empiric methods. Flength and Reθc are depend on $R\tilde{e}_{\theta t}$.

Constants for intermittency equation are given as follows,

$$C_{a1} = 2 \qquad C_{e1} = 1 \qquad C_{a2} = 0.06 \qquad C_{e2} = 50 \qquad c_{\gamma 3} = 0.5 \qquad \sigma_{\gamma} = 1.0$$

Transport equation of transition momentum thickness Reynolds Number $R\tilde{e}_{\theta t}$ is obtained via,

$$\frac{\partial(\rho\widetilde{Re}_{\theta t})}{\partial t} + \frac{\partial(\rho U_j\widetilde{Re}_{\theta t})}{\partial x_j} = P_{\theta t} + \frac{\partial}{\partial x_j}\left[\sigma_{\theta t}(\mu + \mu_t)\frac{\partial\widetilde{Re}_{\theta t}}{\partial x_j}\right] \tag{3.56}$$

And the source term $P_{\theta t}$ is found using the equations below,

$$P_{\theta t} = c_{\theta t}\frac{\rho}{t}(Re_{\theta t} - \widetilde{Re}_{\theta t})(1.0 - F_{\theta t}) \tag{3.57}$$

where;

$$t = \frac{500\mu}{\rho U^2}$$

$$F_{\theta t} = min\left(max\left(F_{wake}e^{\left(-\frac{y}{\delta}\right)^4}, 1.0 - \left(\frac{\gamma - 1/50}{1.0 - 1/50}\right)^2\right), 1.0\right)$$

$$\theta_{BL} = \frac{\widetilde{Re}_{\theta t}\mu}{\rho U}$$

$$\delta_{BL} = \frac{15}{2}\theta_{BL}$$

$$\delta = \frac{500\Omega y}{U}\delta_{BL}$$

$$Re_{\omega} = \frac{\rho\omega y^2}{\mu}$$

$$F_{wake} = e^{-\left(\frac{Re_{\omega}}{1E+5}\right)^2}$$

Model constants for the transition momentum thickness Reynolds Number are,

$$c_{\theta t} = 0.03 \quad \sigma_{\theta t} = 2.0$$

Transition SST model includes 3 empirical correlations which has been given as follows.

$$Re_{\theta t} = f(Tu, \lambda) \tag{3.58}$$

$$F_{length} = f\left(\widetilde{\mathrm{Re}}_{\theta t}\right) \tag{3.59}$$

$$Re_{\theta c} = f\left(\widetilde{\mathrm{Re}}_{\theta t}\right) \tag{3.60}$$

Tu term in the first correlation is turbulence intensity defined as,

$$\mathrm{Tu} = \frac{100}{\mathrm{U}}\sqrt{\frac{2}{3}\mathrm{k}} \tag{3.61}$$

k is the turbulent kinetic energy and the pressure gradient coefficient of Twaites is obtained via,

$$\lambda_{\theta} = (\theta^2/\mathrm{v})\frac{\mathrm{dU}}{\mathrm{ds}} \tag{3.62}$$

This model includes a correction modification for the separation induced transition which is,

$$\gamma_{sep} = \min\left(C_{s1}\max\left[\left(\frac{Re_v}{3.235Re_{\theta c}}\right) - 1.0\right]F_{reattach}, 2\right)F_{\theta t} \quad (3.63)$$

$$F_{reattach} = e^{-\left(\frac{R_T}{20}\right)^4} \quad (3.64)$$

$$\gamma_{eff} = \max(\gamma, \gamma_{sep}) \quad (3.65)$$

where; Cs1 has a value of 2. γ is zero for wall boundary condition and 1 for the inlet boundary condition.

3.5.5.2 Best practice and comments for SST K- ω

In addition to the SST k-w model, transition-SST model couples the standard SST k-w with two other transport equations which are used for intermittency and transition onset criteria via momentum thickness Reynolds number [Bakker, 2005]. Utilizing two more transport equations, results in a more accurate turbulence modeling in return as stated by previous works [Bulat et. al., 2013].

3.6 Discretization Scheme

Any governing equation regarding the fluid flow must be discretized in order to construct and prepare the data for the computer process. This situation constitutes the fundamentals for CFD analysis. Discretization methods mainly evaluated according to three titles which are named as finite difference, finite element and finite volume methods. FLUENT utilizes finite volume method which is the most suitable for this type of application as also stated by many.

There are also variety of methods in FLUENT regarding spatial discretization such as upwind, central-differencing, QUICK and MUSCL for density based solver option.

Pressure based solver also has various discretization algorithms however, for this study these schemes are not included.

There is an option regarding the selection of the discretization methods of all convection terms in FLUENT. In order to properly determine the discretization of any parameter, effects of order of the scheme and discretization type must be known. For this reason, discretization scheme is studied under two subtopics.

3.6.1 Order of the Scheme

Order of scheme is defined by the order of omitted terms in Taylor Series expansion of the discretized function. Therefore, if the first order derivative and consecutive terms are ignored, the function is said to be first order accurate. Same goes for the higher order derivative terms in the Taylor Series expansion of the discretized function.

3.6.2 Type of the Scheme

Type of scheme determines how the face values of a control volume are calculated for convective parameters. Fluent includes upwind, central differencing, power law, QUICK and MUSCL schemes for density based solver.

Scheme is named as upwind if the cell face value is interpolated using only upstream cell or cells depending on the order of accuracy. Upwind scheme can be used with first or second order accuracy in most commercial CFD codes. First order upwind scheme is the simplest scheme among the aforementioned making it the easiest to implement as well as being stable. However it is also very diffusive resulting smeared out gradients in the flow [Bakker, 2005]. Second order upwind scheme is more accurate than the first order while being fairly stable. Although it is utilized commonly, this scheme may produce cell face values that are outside the range of cell values if strong gradients are present in the flow. For this reason, limiters for cell face values are put to use.

When the cell face value is interpolated utilizing present and upstream cell centroid values, the scheme is called central differencing. Central differencing is better than first order upwind in terms of accuracy however it may cause oscillations in the solution or divergence depending on the local Peclet Number.

Power law scheme works utilizing an exponential function depending on Peclet Number between upstream and present cells. For Peclet Number's bigger than 10, power law scheme produces same results with first order upwind scheme.

QUICK abbreviation stands for quadratic upwind interpolation for convective kinetics. As can be understood from the abbreviation this scheme type interpolates the cell face value by fitting a quadratic curve to two adjacent upstream cell centroid values and the value of present cell centroid. Although this scheme is one of most accurate, over or undershoots may occur when strong gradients are available in the flow.

MUSCL (Monotone Upstream Centered Schemes for Conservation Laws) works by blending central differencing scheme and second order upwind scheme making it the third order accurate however, if flow field has any discontinuation such as shocks, it may undershoot or overshoot the cell face values [Bakker, 2005].

First order upwind scheme has been selected for this study, because of the stability reasons associated with second order upwind scheme.

3.7 Convergence Criteria

Convergence of a solution must be determined thoughtfully in order to not mistakenly guided by an unconverged solution. Therefore some criteria have been established by the author to define a converged solution. Criteria utilized for the analyses that have been conducted in this study are listed below;

- Flow field and scalar fields are not changing with additional iterations.

- Residuals are not decreasing (If monitored variables are not changing, this may be discarded).
- Lift & Drag is not changing.
- Inlet & Outlet mass balance is reached (%0.5 tolerance).

All of the analyses have been terminated and determined as converged if the mentioned criteria are satisfied. Residuals, monitor of lift, drag and thrust have been shown as examples in Figures 3.14 to Figure 3.17.

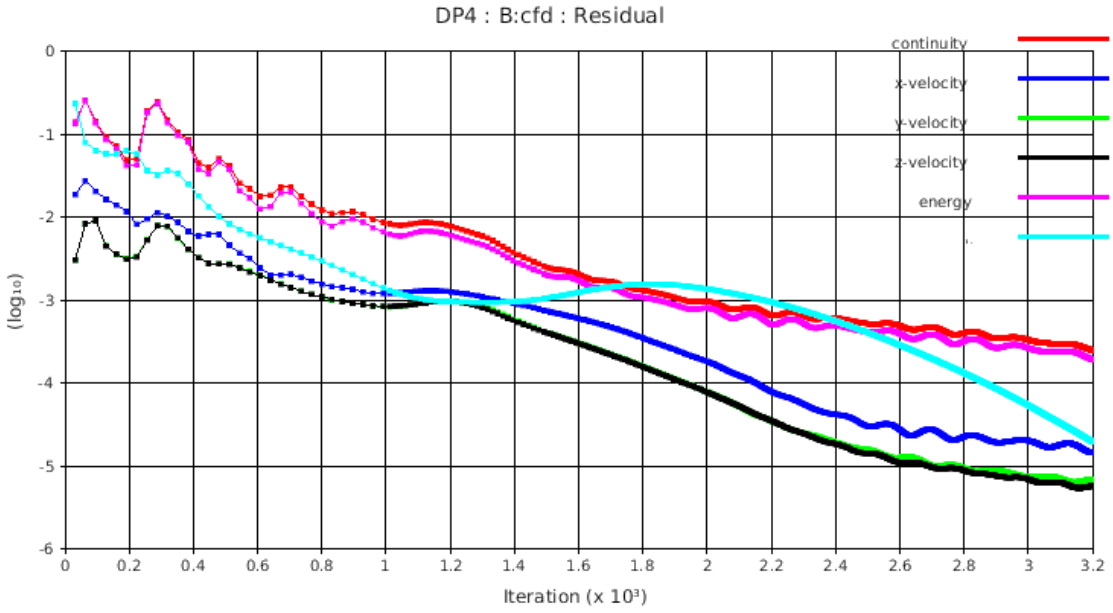

Figure 3.14: Residuals of k-w solution

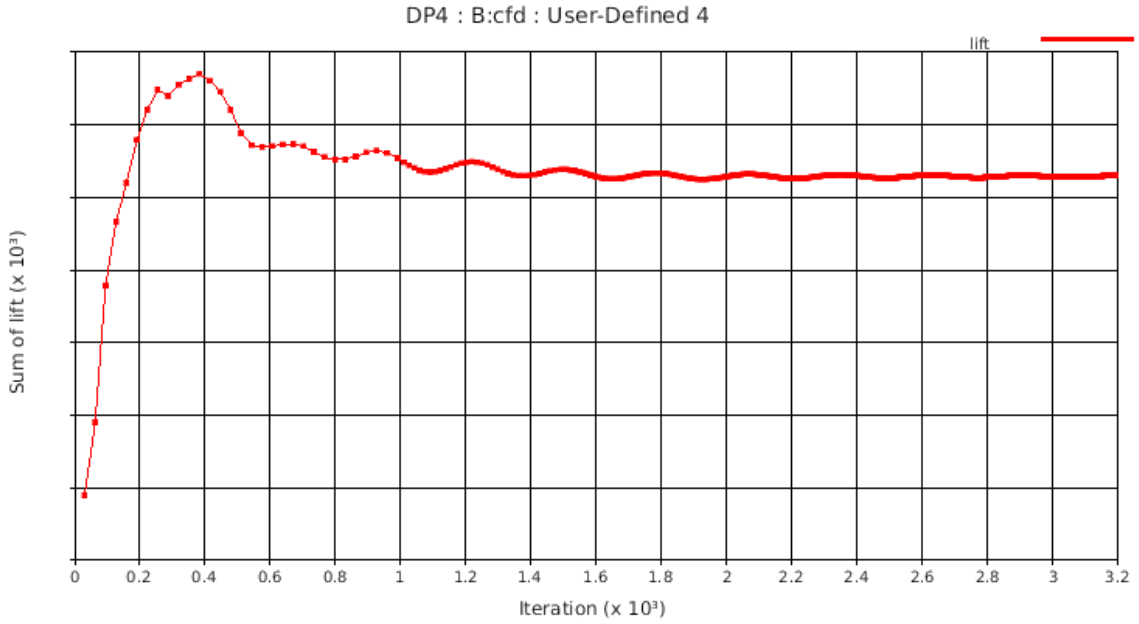

Figure 3.15: Lift monitor

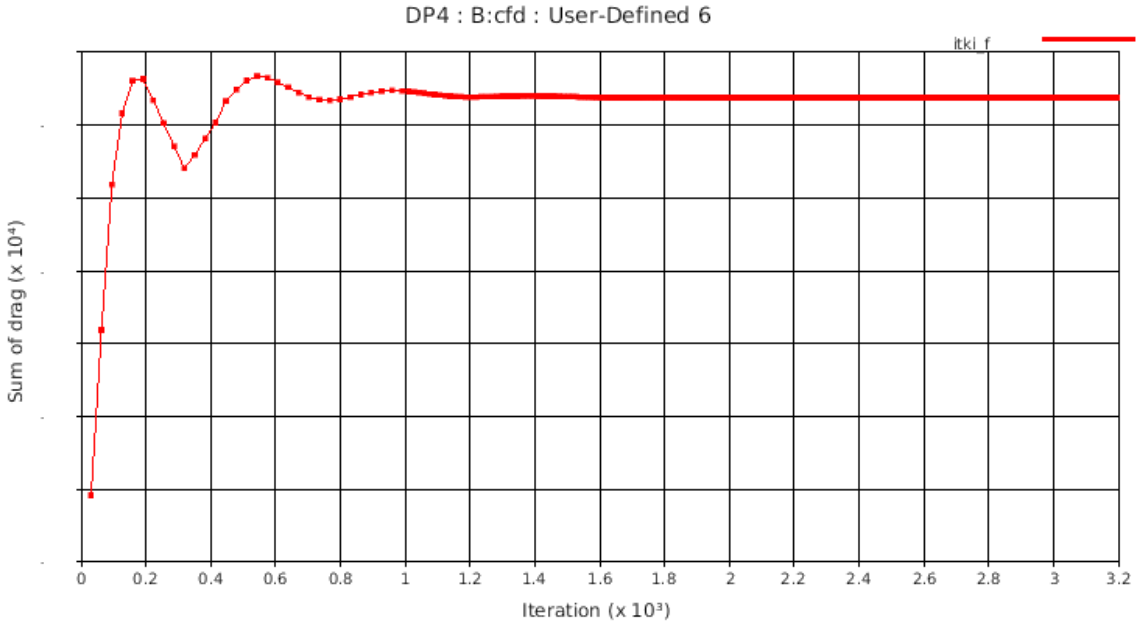

Figure 3.16: Thrust monitor

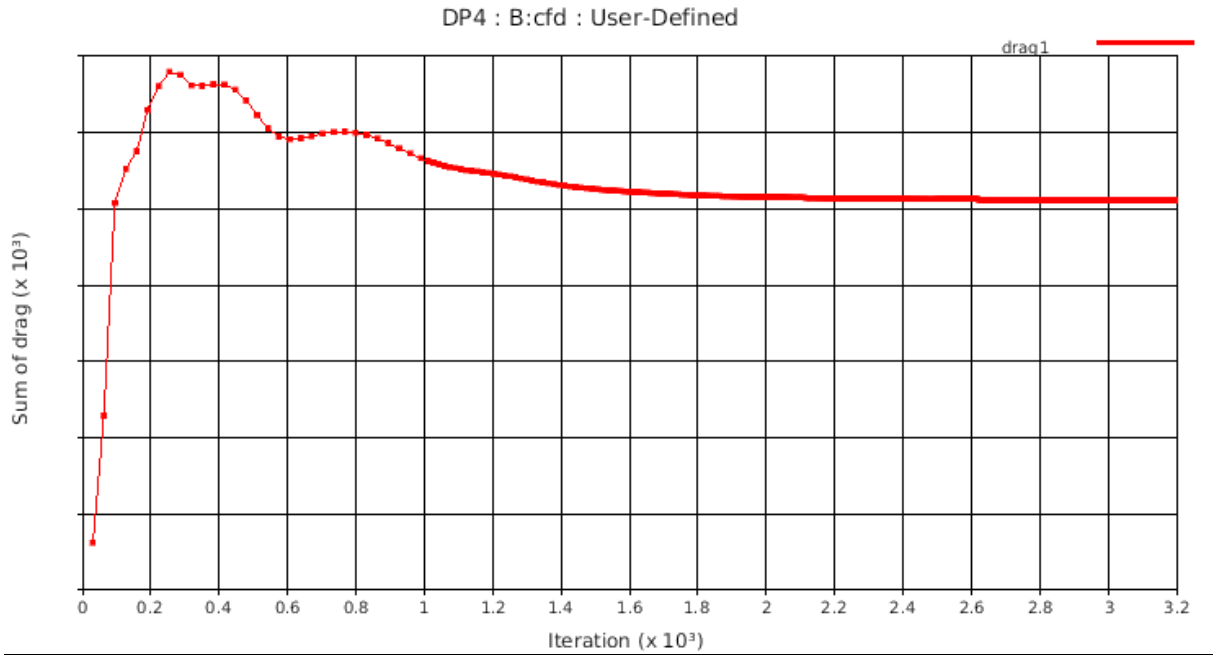

Figure 3.17: Drag monitor

3.8 Computational Fluid Dynamics Results

In order to achieve sufficient accuracy with less CPU time, all of the considered turbulence models have been utilized on the lowest quality grid possible (0.7 million elements) for different angle of attack values. Higher angle of attacks have been observed to result in higher error amount. The results have been listed for low quality grid in Table 3.1.

Table 3.1: Turbulence model performance on coarse mesh

The Lowest Quality Mesh (0.7m)		
	Angle of Attack	**Error (%)**
K-Epsilon	x	4,71
	2x	5,54
	4x	19,52
Standard K-Omega	x	2,62
	2x	6,60
	4x	18,92
K-Omega SST	x	2,94
	2x	7,01
	4x	19,11
Transition-SST	x	2,59
	2x	6,84
	4x	18,63
Spalart-Allmaras	x	3,52
	2x	6,28
	4x	18,90

Taking this into consideration, a low quality mesh with (1.4 million elements) is created and tested for only the highest angle of attack value for different turbulence models.

Table 3.2: Turbulence model performance on low mesh

Low Quality Mesh (1.4m)		
	Angle of Attack	**Error (%)**
K-Epsilon	4x	11,34
Standard-K-Omega	4x	10,84
K-Omega-SST	4x	11,23
Transition-SST	4x	10,61
Spalart-Allmaras	4x	11,95

Transition- SST turbulence model has generated the smallest amount of error for the lift and drag compared to the other evaluated turbulence models. However k- ω model has nearly yielded the same results with 0.2% difference. As mentioned in the previous sections Transition-SST utilizes 4 transport equations while k-ω model only uses 2 transport equations which means k-w turbulence model is more economical in terms of CPU time. Realizable k-ε and Spalart-Allmaras turbulence models are eliminated because of the accuracy concerns leaving the k- ω model to be the best candidate for the solutions. A mid quality mesh with 3 million elements is also applied to the case as improved quality may present a different outcome. Table 3.3 is the results of mid quality mesh for each turbulence model and it is clearly states that a little improvement on amount of error has been obtained.

Table 3.3: Turbulence model performance on medium mesh

Mid Quality Mesh (3m)		
	Angle of Attack	**Error (%)**
K-Epsilon	4x	11,03
Standard-K-Omega	4x	10,53
K-Omega-SST	4x	10,46
Transition-SST	4x	10,38
Spalart-Allmaras	4x	11,51

Best results are again obtained with Transition SST model however this model is computationally more expensive than the other models that have been utilized. Especially k-ω model has nearly given the same results with significantly reduced calculation time. For this reason, only k-ω model has been preferred with high density mesh to save time. Higher quality meshes (7 and 12 million elements) with k- ω model has also been tested to investigate the mesh dependency levels however, error amount of the higher quality mesh (7 and 12 million elements) analysis showed no improvement

over mid quality mesh analysis which did not justify the increased calculation time (210 hours or 355 hours). Results of the high density mesh are given in Table 3.4 below.

Table 3.4: Mesh Dependency Analysis Results

	Angle of Attack	Mesh Count	Calculation Time	Error (%)
Standard K-Omega	4x	0.7	10	18,92
		1.4	22	10,84
		3	85	10,53
		7	210	10,61
		12	355	10,79

Distribution of y+ values that are used for k-omega model is given above. Y+ values are never exceeding 5 over the surface of TVC which is necessary for accurate calculations. Note that this y+ distribution is utilized for k-w. If the same distribution was to be used with k-epsilon model, standard wall function would give erroneous results since standard wall function only works with logarithmic wall law. In that case enhanced wall treatment option must be used. In the scope of this study k- epsilon model is used with coarser mesh near the walls.

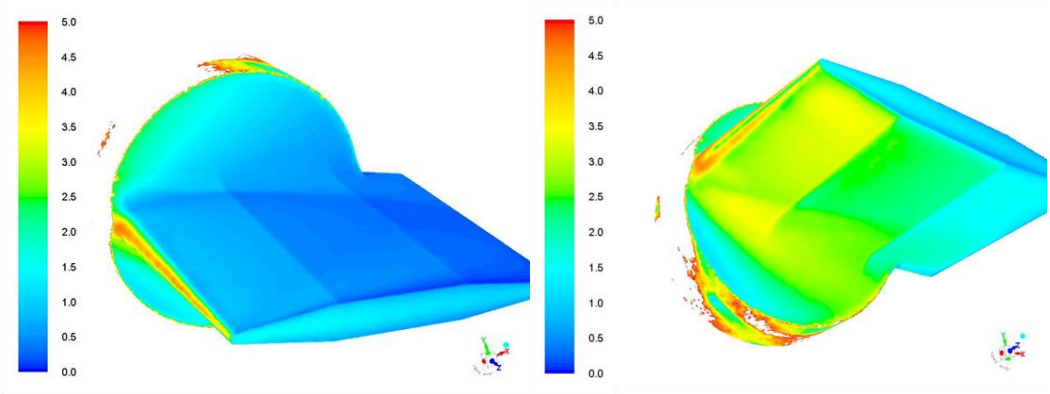

Figure 3.18: Y+ Distribution on the TVC

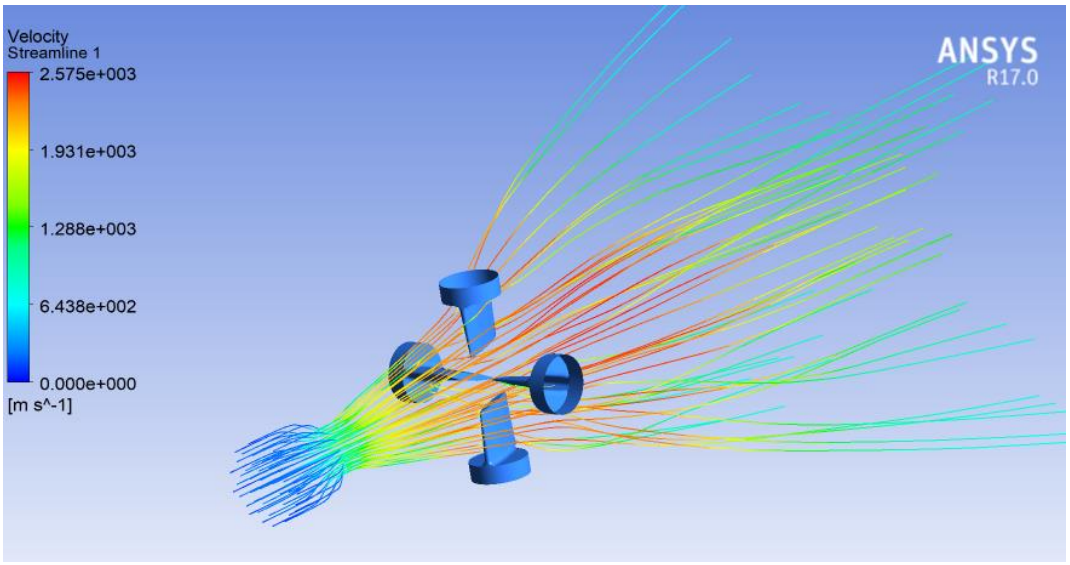

Figure 3.19: Velocity streamlines over TVC

Streamlines of the flow over the thrust vectoring vanes is shown in Figure 3.19 and Figure 3.20 along with the static pressure distribution over the vanes.

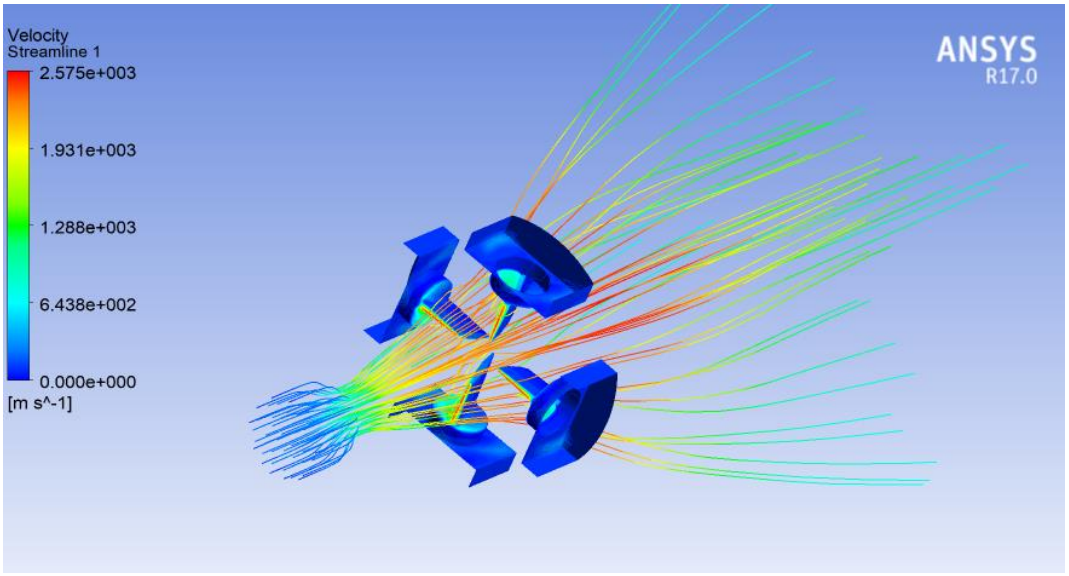

Figure 3.20. Velocity streamlines above TVC with pressure distribution

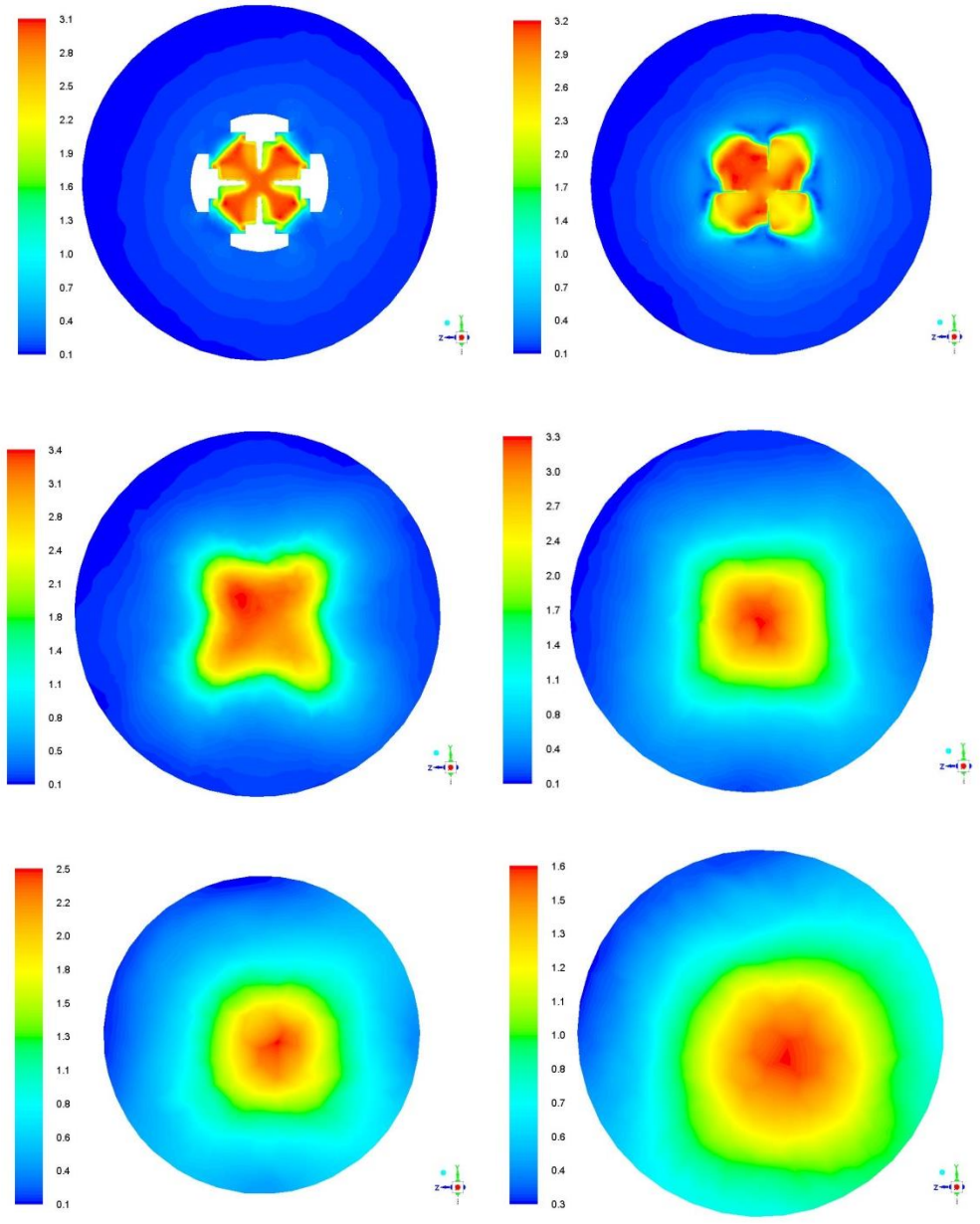

Figure 3.21: Downstream cross-plane mach distributions with 10 cm intervals

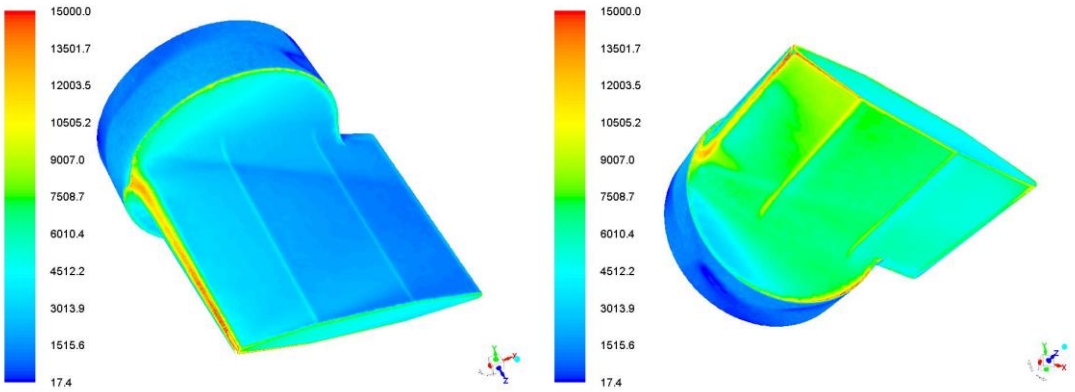

Figure 3.22. Wall Shear Stress Distribution on the TVC

Wall shear stresses along with the Mach number distribution of nozzle exit plane with 10 cm intervals are given in Figure 3.21 and 3.22.

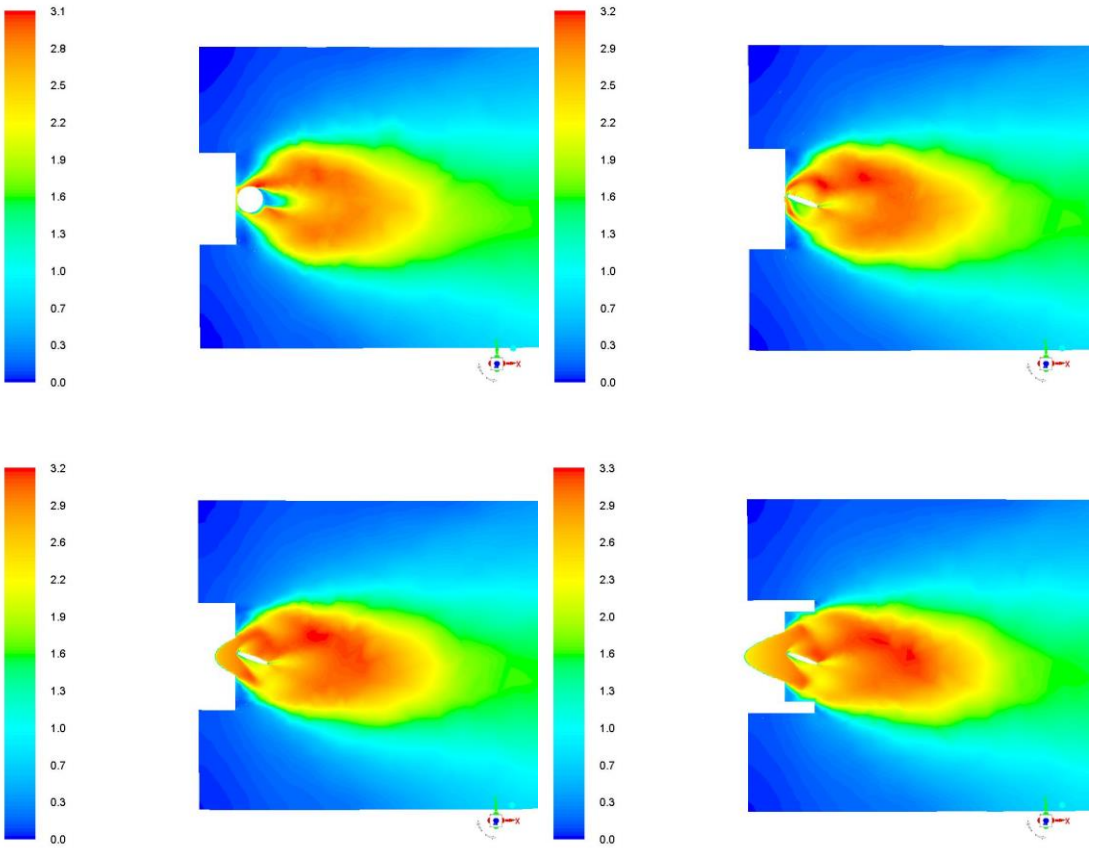

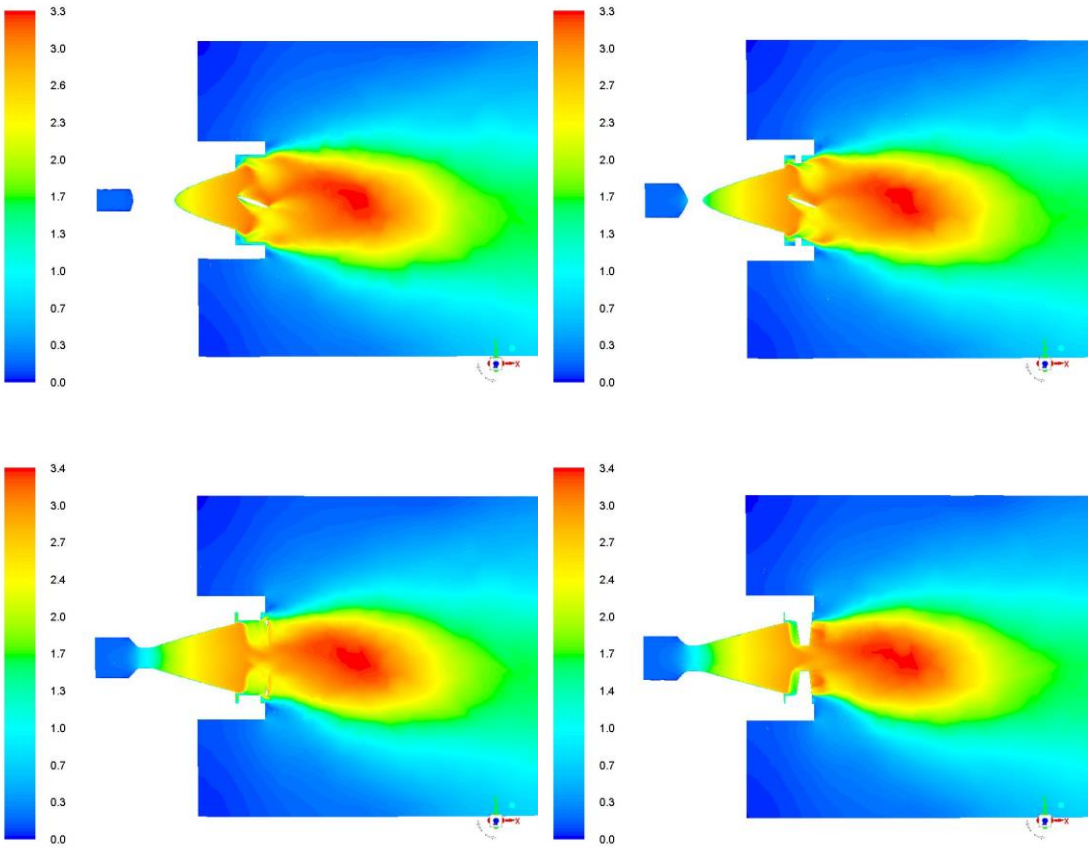

Figure 3.23: Cross-plane mach distributions on TVC with 1 cm intervals

In Figure 3.23 velocity distribution is shown on a cross plane approximately 10 centimeters downstream of the thrust vectoring vanes. Similarly Figure 3.21 shows the velocity distribution on the outlet plane. Since the TVC vanes have no twist Mach number distributions are nearly the same. Differences are observed only due to the nozzle exit Mach number profile. Note that, the locus point of the velocity distribution has been deflected due to the effects of thrust vectoring vanes.

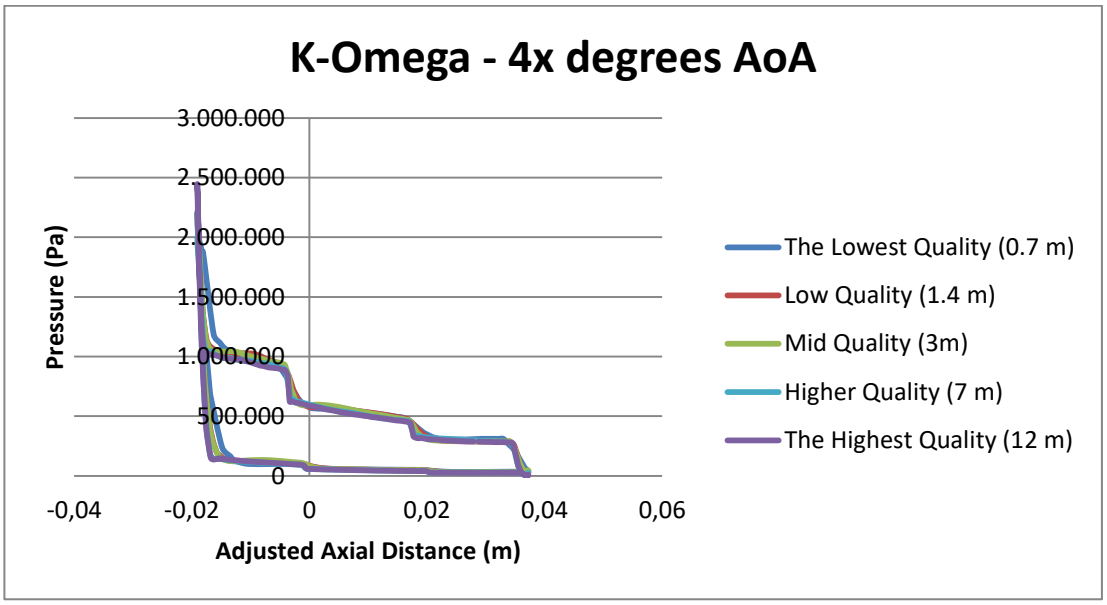

Figure 3.24: Pressure distribution at mean span

Pressure distribution at the mean span of TVC has been given in the Figure 3.24. Note that, with the grid quality changes, difference in pressure distribution get sharper. This situation is expected since the profile of TVC includes sharp corners.

In conclusion, the computational effort with k-omega turbulence model with 3 million elements presents acceptable amount of error in maximum AoA. Stated 10% error approximately related to initial phase of experiment and it has been found that the performance of the TVC vanes differs in time. It is better to examine CFD results in comparison of the test scenario in order to determine whether there is mismatch points.

3.9 Comparison of Computational and Experimental Results

For a conclusive review of the findings, comparison on computational and experimental results is plotted in Figure 3.25. The test measurement and k-omega turbulence model with 1.4M mesh elements CFD result show approximately 10% amount of error at maximum AoA with desirable amount of computational cost. To investigate the entire

scenario with specified CFD approach, steady state analysis for each AoA is applied. At an interval around 0.3, 0.5 and 0.85 provides the most significant variance on comparison as 11%, 7% and 10% error which has an average close to 9%. That amount of error is considered as acceptable start point of a design.

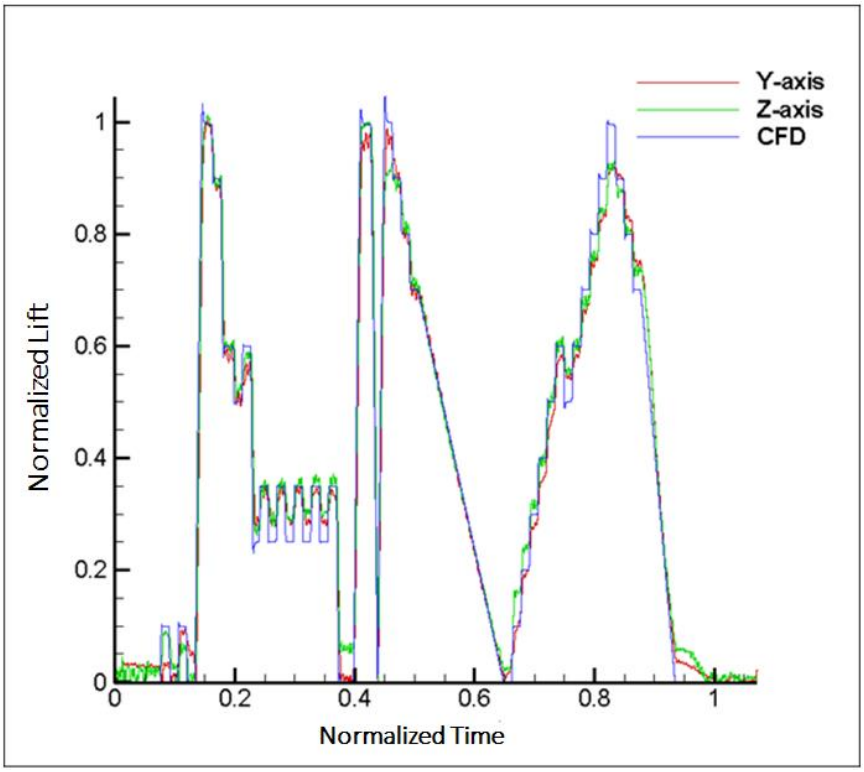

Figure 3.25: Comparison of normalized lifts of test and CFD result

The stated errors for this study are assumed to be generated by such factors given below.

- The surface ablation creates variation on temperature distribution by the heat transfer phenomenon. That leads to a difference on readings between y axis, z axis and CFD results.
- The CFD analysis is conducted by steady state approach instead of a transient analysis which is more suitable for the case. With a transient analysis, the engine performance in time can be evaluated; therefore the CFD results can be more accurate.

- Some obvious and critical inaccuracy parameters of test stand are examined but still there is a residual level of error. Due to load cell capacity, forces with low values presents inconsistency arbitrarily.

CHAPTER 4

CONCLUSION

A novel jet vane based TVC design including mechanical design phase, computational analysis phase and testing phase has been conducted to acquire the best possible option for turbulence model and mesh quality for such task. In the process of this study, several key points are either assumed to be an ideal case or found inadequate to explain the phenomenon. Most significant ones are the computational approach to actual physics occurred on the subject as being a transient event and having surface ablation; additionally less significant ones are the test stand inaccuracy on axis base and low force inputs. Nonetheless, the presented path to design a TVC by mechanical, computational and experimental efforts shows a valid approach to such work.

4.1 Future Works

According to this study, 4 piece of deduction can be expressed for a future work.

- The CFD analysis has no taken into account the thermal outputs instead the temperature distribution on components used to calibrate these outputs. Although it is such an extensive work, the ablation characteristics can be put out not only for computational objective but also for improvement to a better comparison state between test and analysis.
- The CFD study can be executed by means of transient analysis additional to determining the erosion of jet vanes in time. This type of analysis can bring out entire service parameters of test engine such as pressure variance; therefore it will help to reduce amount of error

- The corrective factors on measurement are the fraction of a large study which is called uncertainty analysis. This analysis also requires every aspect of test stand to be known and put on to a data reduction equation with amount of error relation between single components which will be another tiresome work to be done, on the other hand it will help to see total behavior of the test stand
- Significant amount of error due to using the load cell in its limit is generated in test phase. Resolving this problem requires partial measuring with a lower duty load cell and multiple testing which creates uneconomical and infeasible environment for testing. The best improvement can be done in here is calibrating the load cells as close as possible to the maximum measuring value in order to reduce error on the other end limit.

REFERENCES

Ankeney D. P. and Woods C. E. (1963), *"Design Criteria for Large Accurate Solid-Propellant Static-Thrust Stands"*, Navweps Report 8353, China Lake: CA

Ansys. (2006), *"Introductory FLUENT Training"* Retrieved 28 July, 2017, from http://www.engr.uconn.edu/~barbertj/CFD%20Training/Fluent/4%20Solver%20Settings.pdf

Ansys. (2015) *"Realizable k-ε Model"*, Retrieved 28 July, 2017, from https://www.sharcnet.ca/Software/Ansys/17.0/en-us/help/flu_th/flu_th_sec_turb_realizke.html#x1-1180005.4.3

Ansys. (2015), *"Reynolds Averaged Navier-Stokes (RANS) Turbulence Models*" Retrieved 28 July, 2017, from https://www.sharcnet.ca/Software/Ansys/17.0/en-us/help/flu_ug/flu_ug_sec_turb_rans.html

Ansys. (2015) *"Standard k-ω Model"* Retrieved 28 July, 2017, from https://www.sharcnet.ca/Software/Ansys/17.0/en-us/help/flu_th/flu_th_sec_turb_kw_std.html#x1-1280005.5.1

Archer D., (2010), "Pressure Distribution and Calculation of Pressure Cone Angle", Fastener Technology International Magazine

Babu P. S. and Prasad S. S. (2012), *"Thrust Vector Control Studies using Jet Vanes",* International eJournal of Mathematics and Engineering, 3 (5), 1904-1906

Bakker, A. (2005). *"Applied Computational Fluid Dynamics. Lecture"* Retrieved July 28, 2017, from http://conteudo.icmc.usp.br/pessoas/gustavo.buscaglia/cursos/mfc_undergrad2/bakker_05-solv.pdf

Brimhall Z. N., Atkinson J. P., Kirk D. R. and Peebles H. G. (2008), *"Design of a Novel Six Degree of Freedom Solid Rocket Motor Test Stand",* 43th AIAA/ASME/SAE/ASEE Joint Propulsion Conference & Exhibit, Cincinnati: OH

Brimhall Z. N., Divitotawela N., Atkinson J. P., Kirk D. R. and Peebles H. G. (2008), "Design and Validation of a Six Degree of Freedom Rocket Motor Test Stand", 44th AIAA/ASME/SAE/ASEE Joint Propulsion Conference & Exhibit, Hartford: CT

Brown K. H., Morrow C., Durbin S., Baca A. (2008), "Guideline for Bolted Joint Design and Analysis: Version 1.0", SAND2008-0371, Sandia National Lavoratories

Budynas R. and Nisbett K. (2005), "Shigley's Mechanical Engineering Design (8th ed.)", London, UK: McGraw-Hill Education

Bulat, M., & Bulat, P. (2013). "*Comparison of Turbulence Models in the Calculation of Supersonic Separated Flows".* Retrieved July 28, 2017, from https://pdfs.semanticscholar.org/b308/627784a0f4a0807fdf133692d73e0e550932.pdf

Carnahan B., Luther H. A. and Wilkes J. O. (1990), *"Applied Numerical Methods",* Florida, USA: Krieger Publishing Company (Originally published in 1969)

Cho D., Jung D. and Tsiotras P. (2009), *"A 5-dof Experimental Platform for Autonomous Spacecraft Rendezvous and Docking",* AIAA Infotech@Aerospace Conference and AIAA Unmanned Unlimited Conference, Seattle: WA

Çelik T. (2014), *"Dynamic Modeling and Control of a Hybrid Fin Actuation System for an Air-to-Air Missile"*, Middle East Technical University, Turkey

Davidian K. J. (1987), "Pretest Uncertainty Analysis for Chemical Rocket Engine Tests", NASA/TM 89819

Dulke M. F. (1987), *"Heat Transfer Modeling of Jet Vane Thrust Vector Control (TVC) Systems"*, Naval Postgraduate School, California: USA

Facciano A. B., Seybold K. G., Westberry-Kutz T. L. and Widmer D. O. (2002), *"Evolved SeaSparrow Missile Jet Vane Control System Prototype Hardware Development",* Journal of Spacecraft and Rockets, 39 (4), 1-2

Hamel N., Farinaccio R., deChamplain A., Kretschmer D., Fournier É.Y. (2003), *"Pressure and Force Measurements on a Thrust Vector Control Vane",* 39th AIAA/ASME/SAE/ASEE Joint Propulsion Conference and Exhibit, Huntsville: AL

Harrisson V., deChamplain A., Kretschmer D., Farinaccio R. and Stowe R.A. (2003), *"Force Measurements Evaluating Erosion Effects on Jet Vanes for A Thrust Vector Control System"*, 39th AIAA/ASME/SAE/ASEE Joint Propulsion Conference and Exhibit, Huntsville: AL

Hawkins J. (2014), *"Analysis of a Wind Turbine Test Bench Calibration Stand Using the Finite Element Method and Experimental Data"*, Clemson University, USA

Hibbeler R. C., Fan S. C. (2011), *"Mechanics of Materials (8th ed.)",* NJ, USA: Prentice Hall

Keller R.B. Jr. and Kordig J. W. Jr. (1971), *"Captive-fired Testing of Solid Rocket Motors - Space Vehicle Design Vane /chemical Propulsion",* NASA-SP-8041

Lauzon M. (1990), *"5DOF Dynamic Loads on a Jet Vane*, 26th AIAA/ASME/SAE/ASEE Joint Propulsion Conference, Orlando: FL

Mark, H. (2003), *"Encyclopedia of Space Science and Technology*", vol. I, New Jersey: John Wiley & Sons, Inc.

McAmis R. (1991), *"An Analysis Tool for Assessing Dynamic Response of a Rocket Motor"*, 27th AIAA/ASME/SAE/ASEE Joint Propulsion Conference, Sacramento: CA

Miloš P., Davidović N., Jojić B., MilošM.andTodić I. (2015), *"A Novel 6 DOF Thrust Vector Control Test Stand"*, TehnickiVjesnik-Technical Gazette, 22 (5), 1247-1254

Murray L. and Storkey A. (2011), *"Particle Smoothing in Continuous Time: A Fast Approach Via Density Estimation"*, IEEE Transactions on Signal Processing, 59 (3), 2-4

Novatech Measurement Ltd. (n.d.), *"Engineering Application Sheet E007- Measurement Mode"*, Novatech Measurement Ltd., East Sussex: UK

Nunn R. H. (1988), *"TVC Jet Vane Thermal Modeling Using Parametric System Identification",* Naval Postgraduate School, California: USA

Rainville P.A., deChamplain A., Kretschmer D., Farinaccio R. and Stowe R.A. (2004), *"Unsteady CFD Calculation for Validation of a Multi-Vane Thrust Vector Control System"*, 40th AIAA/ASME/SAE/ASEE Joint Propulsion Conference and Exhibit, Indianapolis: IN

Riddle D. B. (2007), *"Design Tool Development for Liquid Propellant Missile Systems"*, Auburn University, USA

Runyan R. B., Rynd Jr. J. P. and Seely J. F. (1992), *"Thrust Stand Design Principles",* 17tg AIAA Aerospace Ground Testing Conference, Nashville: TN

Schaefermeyer M. R. (2011), *"Aerodynamic Thrust Vectoring For Attitude Control of A Vertically Thrusting Jet Engine"*, Utah State University, USA

Simmons F. S. (2000),*"Rocket Exhaust Plume Phenomenology"*, Reston, VG: American Institute of Aeronautics and Astronautics Inc.

Sims J. D. and Coleman H. W. (2003), *"Hysteresis Effects on Thrust Measurement and its Uncertainty"*, Journal of Propulsion and Power, 19 (3), 1

Šoltészová V., Helljesen L. E. S., Wein W., Gilja O. H. and Viola I. (2012), *"Lowest-Variance Streamlines for Filtering of 3D Ultrasound",* Eurographics Workshop on Visual Computing for Biology and Medicine, Norrköping: Sweden

The Institute of Measurement and Control, 2013, *"Guide to the Measurement of Force",* London, UK: The Institute of Measurement and Control (Originally published in 1998)

Yen D. and Bräuchle F. (2000), *"Calibration and Uncertainty Analysis for the UC Davis Wind Tunnel Facility"*, University of California, Davis, USA

Yu M. S., Cho H. H., Hwang K. Y. and Bae J. C. (2004), *"A Study on A Surface Ablation of The Jet Vane System in a Rocket Nozzle"*, 37th AIAA ThermophysicsConference, Portland: OR

Wasserman, S. (2016, November 26). Retrieved July 28, 2017, from *http://www.engineering.com/DesignSoftware/DesignSoftwareArticles/ArticleID/13743/Choosing-the-Right-Turbulence-Model-for-Your-CFD-Simulation.aspx*

Wright A. M., Strickland R., Born T., Wright A., Steadman S. and Tidwell J. (2013), *"Design and Calibration of a Six Degree-of-Freedom Thrust Sensor for a Lab-Scale Hybrid Rocket",* 51st AIAA Aerospace Sciences Meeting including the New Horizons Forum and Aerospace Exposition, Grapevine (Dallas/Ft. Worth Region): TX

Wong K. C. (2003), *"Derivation of the Data Reduction Equations for the Calibration of the Six-Component Thrust Stand in the CE–22 Advanced Nozzle Test Facility",*NASA/TM—2003-212326

APPENDIX A

RAW AND CALIBRATED DATA OF TEST STAND

The raw and calibrated data are given in form of proportional to the related true value in each step. The true values which they are acquired for comparison are the readings from the second output of the calibration load cells.

TABLE A.1: RAW AND CALIBRATED DATA OF X AXIS IN COMPRESSION

		X-axis Raw Data Cycle 1			X-axis Raw Data Cycle 2			X-axis Raw Data Cycle 3			X-axis Calibrated Data Cycle 1			X-axis Calibrated Data Cycle 2			X-axis Calibrated Data Cycle 3		
start	0	0	0	0	0	0	0	0	0	0	0	0	0	0	0	0	0	0	0
increment	Step 1	99,29832	0,05474	0,23958	99,33746	0,04132	0,23367	99,34782	0,05551	0,22660	99,89075	0,24798	0,39400	99,93012	0,23460	0,40013	99,94062	0,24884	0,40732
	Step 2	99,50923	0,02502	0,25135	99,24294	0,00357	0,25307	99,51337	0,01330	0,24057	100,10279	0,21861	0,38346	99,83482	0,18944	0,37996	100,10690	0,18022	0,39418
	Step 3	99,48365	0,00954	0,27933	99,48020	0,00955	0,28353	99,55131	0,03084	0,27489	100,07687	0,20305	0,35522	100,07333	0,18392	0,35094	100,14486	0,16272	0,35990
	Step 4	99,52060	0,02555	0,31405	99,50204	0,03762	0,31897	99,54309	0,03892	0,31612	100,11377	0,16797	0,32056	100,09504	0,15583	0,31549	100,13634	0,15461	0,31852
	Step 5	99,49047	0,05254	0,36410	99,50204	0,05243	0,36072	99,49079	0,05344	0,35665	100,08313	0,14087	0,27015	100,09478	0,14101	0,27361	100,08349	0,13997	0,27763
	Step 6	99,46289	0,09355	0,42448	99,47978	0,08700	0,42018	99,47094	0,01805	0,41315	100,05497	0,09974	0,20935	100,07200	0,10634	0,21378	100,06332	0,17541	0,22095
	Step 7	99,43992	0,12664	0,48030	99,47805	0,12076	0,47098	99,46372	0,11966	0,47213	100,03149	0,06655	0,15317	100,06990	0,07251	0,16278	100,05548	0,07359	0,16151
	Step 8	99,46448	0,14850	0,53536	99,46122	0,14646	0,53115	99,45634	0,15219	0,52674	100,05585	0,04470	0,09811	100,05259	0,04674	0,10231	100,04769	0,04099	0,10669
	Step 9	99,41566	0,17282	0,58802	99,44626	0,16647	0,58066	99,43539	0,16653	0,57945	100,00640	0,02025	0,04496	100,03724	0,02667	0,05254	100,02631	0,02659	0,05369
	Step 10	99,38519	0,20037	0,64452	99,37916	0,19117	0,64335	99,38928	0,20017	0,64027	99,97538	0,00740	0,01193	99,96934	0,00180	0,01078	99,97952	0,00719	0,00764
Highest	Step 11	99,37442	0,19531	0,64653	99,37916	0,19117	0,64335	99,37400	0,20144	0,63977	99,96455	0,00235	0,01400	99,96934	0,00180	0,01078	99,96414	0,00850	0,00725
	Step 12	99,48087	0,16038	0,57505	99,49698	0,15976	0,57677	99,47515	0,16129	0,57192	100,07209	0,03284	0,05840	100,08829	0,03349	0,05678	100,06636	0,03191	0,06150
decent	Step 13	99,50438	0,14327	0,52877	99,48274	0,14508	0,52855	99,52380	0,14660	0,52520	100,09603	0,05002	0,10498	100,07426	0,04817	0,10506	100,11558	0,04672	0,10864
	Step 14	99,51637	0,11889	0,47444	99,52199	0,12856	0,47146	99,49355	0,12147	0,47227	100,10844	0,07447	0,15956	100,11408	0,06478	0,16256	100,08549	0,07184	0,16160
	Step 15	99,54158	0,16446	0,41500	99,55572	0,09148	0,41514	99,46919	0,09575	0,40987	100,13399	0,02883	0,21915	100,14840	0,10199	0,21931	100,06137	0,09754	0,22402
	Step 16	99,64530	0,05646	0,35687	99,61201	0,06348	0,35590	99,64346	0,05821	0,35160	100,23892	0,13724	0,27836	100,20541	0,13014	0,27911	100,23709	0,13549	0,28359
	Step 17	99,67612	0,04297	0,30888	99,66314	0,05731	0,30928	99,67469	0,04536	0,30722	100,27020	0,15081	0,32669	100,25710	0,13642	0,32616	100,26877	0,14842	0,32826
	Step 18	99,69258	0,03387	0,27551	100,13985	0,05394	0,27828	99,70893	0,05182	0,27127	100,28695	0,15996	0,36026	100,73684	0,14072	0,36029	100,30338	0,14200	0,36456
	Step 19	99,67574	0,02925	0,24514	99,59619	0,01498	0,23829	99,72518	0,04254	0,23306	100,27019	0,16455	0,39060	100,19023	0,17869	0,39699	100,31995	0,15132	0,40283
	Step 20	99,66725	0,00851	0,19667	99,76255	0,08104	0,21185	99,71391	0,02363	0,18432	100,26200	0,20236	0,43922	100,35756	0,11281	0,42436	100,30891	0,17024	0,45117
	Step 21	NaN	NaN	NaN	NaN	NaN	NaN	NaN	NaN	NaN	NaN	NaN	NaN	NAN	NaN	NaN	NaN	NaN	NaN

TABLE A.2: RAW AND CALIBRATED DATA OF Y AXIS IN TENSION

		Y-axis in Tension Raw Data Cycle 1			Y-axis in Tension Raw Data Cycle 2			Y-axis in Tension Raw Data Cycle 3			Y-axis in Tension Calibrated Data Cycle 1			Y-axis in Tension Calibrated Data Cycle 2			Y-axis in Tension Calibrated Data Cycle 3		
start	0	0	0	0	0	0	0	0	0	0	0	0	0	0	0	0	0	0	0
increment	Step 1	0,64568	99,31633	-0,05454	0,79462	99,72717	0,18436	0,04940	99,98207	0,27382	0,39812	99,52026	0,21971	0,54758	99,93169	0,08983	0,20227	100,18859	0,00566
	Step 2	0,43839	99,66456	-0,18723	0,41177	99,83615	0,27550	0,02469	99,85279	0,22405	0,18940	99,86964	0,08905	0,16264	100,04166	0,00125	0,22705	100,05907	0,05535
	Step 3	0,29275	99,60895	-0,21657	0,41837	100,00802	0,29872	0,02756	99,65188	0,24046	0,04319	99,81421	0,06042	0,16897	100,21388	0,02158	0,22357	99,85775	0,03835
	Step 4	0,22153	99,79754	-0,23039	0,20800	99,84616	0,27492	0,09441	99,83871	0,27225	0,02887	100,00333	0,04756	0,04237	100,05209	0,00316	0,15663	100,04484	0,00654
	Step 5	0,26750	99,69240	-0,24629	0,29096	99,81942	0,29296	0,19344	99,81314	0,27301	0,01773	99,89789	0,03104	0,04124	100,02514	0,01552	0,05695	100,01902	0,00507
	Step 6	0,22296	99,69822	-0,24555	0,26857	99,83052	0,27856	0,16086	99,82358	0,25777	0,02710	99,90381	0,03208	0,01863	100,03630	0,00092	0,08982	100,02955	0,02059
	Step 7	0,25176	99,70259	-0,26264	0,26774	99,82614	0,28794	0,13769	99,84744	0,26255	0,00196	99,90813	0,01478	0,01785	100,03191	0,01033	0,11316	100,05350	0,01602
	Step 8	0,28207	99,69067	-0,25264	0,27775	99,79155	0,28513	0,17802	99,78609	0,27312	0,03243	99,89612	0,02458	0,02799	99,99723	0,00767	0,07238	99,99195	0,00498
	Step 9	0,29390	99,79004	-0,24341	0,24234	99,82306	0,29270	0,19689	99,82401	0,26329	0,04402	99,99567	0,03403	0,00768	100,02888	0,01494	0,05355	100,02991	0,01483
	Step 10	0,27174	99,85606	-0,24788	0,21821	100,02359	0,29586	0,18809	99,91267	0,25631	0,02158	100,06187	0,02987	0,03244	100,22986	0,01739	0,06266	100,11876	0,02211
Highest	Step 11	0,26502	99,87380	-0,25712	0,21824	100,02948	0,30817	0,18796	99,88996	0,26467	0,01483	100,07967	0,02071	0,03236	100,23577	0,02971	0,06269	100,09601	0,01368
	Step 12	0,25107	99,76137	-0,24969	0,26421	99,85509	0,30961	0,15774	99,85737	0,26332	0,00104	99,96703	0,02793	0,01434	100,06093	0,03194	0,09302	100,06342	0,01513
decent	Step 13	0,22517	99,70317	-0,25149	0,21522	99,82136	0,28885	0,17743	99,84387	0,26202	0,02485	99,90877	0,02612	0,03496	100,02722	0,01092	0,07318	100,04985	0,01627
	Step 14	0,25729	99,66961	-0,24930	0,24604	99,87635	0,29405	0,13839	99,86065	0,27319	0,00753	99,87507	0,02802	0,00408	100,08227	0,01617	0,11245	100,06674	0,00537
	Step 15	0,22368	99,66062	-0,25964	0,28701	99,87333	0,32037	0,08334	99,86252	0,27284	0,02621	99,86612	0,01784	0,03728	100,07917	0,04281	0,16783	100,06872	0,00609
	Step 16	0,26831	99,64526	-0,23956	0,26116	99,90962	0,31294	0,09997	99,89673	0,27595	0,01862	99,85064	0,03764	0,01114	100,11558	0,03510	0,15117	100,10297	0,00296
	Step 17	0,14260	99,70708	-0,23059	0,20120	99,89331	0,29957	0,03446	99,95031	0,31265	0,10804	99,91284	0,04760	0,04920	100,09935	0,02136	0,21701	100,15680	0,03326
	Step 18	0,14090	99,73042	-0,24649	0,26815	99,88733	0,36624	0,13906	99,95437	0,30152	0,10973	99,93623	0,03175	0,01851	100,09324	0,08862	0,39164	100,16120	0,02098
	Step 19	0,21183	99,82388	-0,25868	0,17259	99,95530	0,41239	0,01979	100,02305	0,31540	0,03854	100,02975	0,01935	0,07755	100,16155	0,13406	0,27176	100,22979	0,03545
	Step 20	0,06714	100,09764	-0,19091	0,06447	100,41847	0,49488	0,41643	100,42331	0,35338	0,18515	100,30434	0,08895	0,18706	100,62591	0,21473	0,67158	100,63166	0,06996
	Step 21	NaN	NaN	NaN	NaN	NaN	NaN	NaN	NaN	NaN	NaN	NaN	NaN	NaN	NaN	NaN	NaN	NaN	NaN

TABLE A.3: RAW AND CALIBRATED DATA OF Y AXIS IN COMPRESSION

		Y-axis in Compression Raw Data Cycle 1			Y-axis in Compression Raw Data Cycle 2			Y-axis in Compression Raw Data Cycle 3			-axis in Compression Calibrated Data Cycle			-axis in Compression Calibrated Data Cycle			-axis in Compression Calibrated Data Cycle		
start	0	0	0	0	0	0	0	0	0	0	0	0	0	0	0	0	0	0	0
increment	Step 1	0,46092	100,16129	-0,22024	0,20937	99,76666	0,33123	0,45644	98,95289	0,36433	0,21098	100,36736	0,05722	0,04049	99,97243	0,05349	0,21029	99,15650	0,09057
	Step 2	0,12288	99,84815	-0,22814	0,33367	99,54309	0,30285	0,17020	99,51131	0,27378	0,12825	100,05424	0,05058	0,08496	99,74815	0,02649	0,07955	99,71662	0,00360
	Step 3	0,29473	99,75037	-0,27216	0,52920	99,69874	0,32269	0,28562	99,91109	0,27492	0,04511	99,95593	0,00510	0,28138	99,90375	0,04718	0,03555	100,11700	0,00285
	Step 4	0,27888	99,88268	-0,27496	0,28225	99,74617	0,28923	0,34494	99,94272	0,27762	0,02884	100,08854	0,00277	0,03265	99,95175	0,01194	0,09516	100,14858	0,00016
	Step 5	0,25897	99,76387	-0,27444	0,28927	99,78335	0,29170	0,27559	99,67637	0,27669	0,00911	99,96952	0,00308	0,03964	99,98900	0,01435	0,02607	99,88181	0,00047
	Step 6	0,33572	99,73334	-0,28946	0,21442	99,79292	0,29976	0,27525	99,65757	0,27423	0,08648	99,93879	0,01255	0,03565	99,99873	0,02192	0,02576	99,86297	0,00290
	Step 7	0,26181	99,79217	-0,28131	0,32797	99,78687	0,29293	0,19707	99,74830	0,28768	0,01193	99,99789	0,00374	0,07856	99,99245	0,01582	0,05305	99,95405	0,00984
	Step 8	0,28785	99,74439	-0,28596	0,25583	99,73073	0,29307	0,23072	99,74447	0,29718	0,03828	99,94995	0,00870	0,00614	99,93633	0,01566	0,01913	99,95015	0,01957
	Step 9	0,29812	99,79244	-0,28611	0,27859	99,76975	0,28923	0,22064	99,67895	0,28444	0,04848	99,99808	0,00878	0,02891	99,97539	0,01185	0,02918	99,88450	0,00693
	Step 10	0,30293	99,76596	-0,28729	0,28193	99,75144	0,29003	0,26767	99,68481	0,28351	0,05340	99,97154	0,01007	0,03233	99,95703	0,01272	0,01811	99,89028	0,00629
Highest	Step 11	0,23801	99,79036	-0,28214	0,29456	99,76152	0,29825	0,24514	99,80007	0,28974	0,01200	99,99612	0,00442	0,04505	99,96711	0,02100	0,00481	100,00583	0,01206
	Step 12	0,25554	99,78689	-0,29421	0,22991	99,77176	0,29149	0,25486	99,76333	0,28442	0,00571	99,99261	0,01664	0,02005	99,97749	0,01380	0,00503	99,96900	0,00690
decent	Step 13	0,23634	99,76325	-0,28584	0,25596	99,82933	0,29301	0,28688	99,68823	0,29473	0,01359	99,96896	0,00820	0,00601	100,03513	0,01532	0,03748	99,89368	0,01764
	Step 14	0,26282	99,79400	-0,29390	0,29230	99,79424	0,29564	0,32338	99,47256	0,28760	0,01301	99,99972	0,01636	0,04267	99,99990	0,01829	0,07471	99,67749	0,01133
	Step 15	0,30671	99,79921	-0,28947	0,24624	99,79129	0,29909	0,27063	99,78868	0,28124	0,05713	100,00485	0,01218	0,00363	99,99703	0,02146	0,02081	99,99437	0,00373
	Step 16	0,27639	99,84905	-0,28100	0,25186	99,77208	0,30405	0,27532	99,65899	0,28593	0,02646	100,05485	0,00336	0,00210	99,97777	0,02652	0,02588	99,86441	0,00882
	Step 17	0,34501	99,85836	-0,28747	0,29822	99,79015	0,30822	0,13414	99,39284	0,30079	0,09549	100,06405	0,01026	0,04870	99,99579	0,03095	0,11539	99,59797	0,02356
	Step 18	0,27616	99,87782	-0,27407	0,36209	99,92434	0,29550	0,15281	99,66134	0,30453	0,02611	100,08368	0,00366	0,11255	100,13013	0,01822	0,09727	99,86699	0,02671
	Step 19	0,46152	99,87289	-0,27430	0,33475	99,94293	0,31446	0,22913	99,86632	0,29313	0,21260	100,07838	0,00224	0,08510	100,14882	0,03700	0,02106	100,07225	0,01517
	Step 20	0,25317	99,82176	-0,27283	0,66625	100,08590	0,42189	0,34316	99,31207	0,36382	0,00312	100,02755	0,00489	0,41878	100,29146	0,14636	0,59500	99,51799	0,08395
	Step 21	NaN	NaN	NaN	NaN	NaN	NaN	NaN	NaN	NaN	NaN	NaN	NaN	NaN	NaN	NaN	NaN	NaN	NaN

TABLE A.4: RAW AND CALIBRATED DATA OF Z AXIS IN TENSION

		Z-axis in Tension Raw Data Cycle 1			Z-axis in Tension Raw Data Cycle 2			Z-axis in Tension Raw Data Cycle 3			Z-axis in Tension Calibrated Data Cycle 1			Z-axis in Tension Calibrated Data Cycle 2			Z-axis in Tension Calibrated Data Cycle 3		
start	0	0	0	0	0	0	0	0	0	0	0	0	0	0	0	0	0	0	0
increment	Step 1	1,92480	0,00781	99,84895	0,03566	0,34818	99,79286	1,19160	0,14872	100,30508	1,41442	0,03369	100,04078	0,48662	0,32672	99,99763	0,67406	0,12449	100,28784
	Step 2	1,31684	0,19204	99,68337	0,94057	0,10147	99,79475	1,44586	0,09215	99,82181	0,80416	0,21708	99,87823	0,42432	0,07775	99,99306	0,93298	0,11727	99,95520
	Step 3	0,91397	0,15280	99,81363	0,95615	0,11081	99,78793	1,30710	0,00134	99,94007	0,39810	0,17700	100,01143	0,44001	0,08707	99,98615	0,79253	0,02334	100,07289
	Step 4	0,83150	0,13515	99,85698	0,89505	0,01437	99,82003	0,90087	0,06570	99,82138	0,31487	0,15917	100,05545	0,37868	0,03826	100,01835	0,38433	0,04197	100,01933
	Step 5	0,80822	0,02361	99,78797	0,76545	0,03764	99,83391	1,02218	0,00517	99,83067	0,29153	0,04734	99,98676	0,24830	0,06133	100,03303	0,50647	0,01892	100,02780
	Step 6	0,75455	0,00665	99,82278	0,76909	0,05708	99,87695	0,83516	0,04579	99,83616	0,23731	0,03025	100,02203	0,25149	0,03357	100,07640	0,31820	0,02214	100,02354
	Step 7	0,67678	0,00627	99,84522	0,66051	0,07156	99,86301	0,76664	0,03466	99,86243	0,15896	0,02972	100,04501	0,14230	0,04830	100,06316	0,24916	0,01112	100,05765
	Step 8	0,77340	0,03986	99,83205	0,67683	0,05607	99,81504	0,71293	0,03034	99,94479	0,25611	0,01633	100,03133	0,15901	0,03276	100,01494	0,19472	0,00688	100,09585
	Step 9	0,70439	0,04501	99,82844	0,63092	0,03247	99,79550	0,71314	0,01895	99,90855	0,18669	0,02162	100,02817	0,11298	0,00920	99,99559	0,19514	0,00453	100,04413
	Step 10	0,67836	0,06336	99,82234	0,60842	0,04446	99,80873	0,77133	0,03008	99,83752	0,16049	0,04006	100,02227	0,09025	0,02126	100,00902	0,25402	0,00653	100,00903
Highest	Step 11	0,64164	0,05814	99,79953	0,63897	0,02922	99,77591	0,63949	0,01404	99,85756	0,12368	0,03490	99,99964	0,12120	0,00593	99,97590	0,12141	0,03743	100,00522
	Step 12	0,60987	0,03231	99,82404	0,65059	0,09614	99,80002	0,77775	0,03365	99,86180	0,09166	0,00907	100,02433	0,13259	0,07296	100,00018	0,26034	0,01008	100,00290
decent	Step 13	0,68223	0,03428	99,85221	0,70251	0,04301	99,80516	0,80432	0,04635	99,86214	0,16448	0,05779	100,05190	0,18493	0,01963	100,00485	0,28704	0,02276	100,00923
	Step 14	0,62670	0,04750	99,81402	0,60691	0,07916	99,75456	0,71223	0,04809	99,87400	0,10860	0,02427	100,01422	0,08892	0,05605	99,95485	0,19433	0,02468	100,01811
	Step 15	0,79425	0,00604	99,89649	0,82624	0,05297	99,77376	0,94715	0,10351	99,89642	0,27683	0,01762	100,09567	0,30953	0,02937	99,97262	0,43040	0,07976	100,02994
	Step 16	0,81035	0,06847	99,78377	0,71127	0,08516	99,75260	0,95452	0,07395	99,87967	0,29346	0,04493	99,98280	0,19390	0,06186	99,95224	0,43797	0,05012	99,97335
	Step 17	0,83543	0,05975	99,83172	0,89288	0,08201	99,74200	1,03324	0,04174	99,97504	0,31846	0,03613	100,03066	0,37666	0,05835	99,94045	0,51675	0,01767	100,07544
	Step 18	1,00334	0,05588	99,81088	0,92186	0,01214	99,73893	0,95759	0,04130	99,99900	0,48750	0,03194	100,00869	0,40607	0,03605	99,93692	0,44052	0,01737	100,05850
	Step 19	1,37456	0,02988	99,69841	1,07616	0,17168	99,78904	1,81435	0,01744	100,14883	0,86174	0,05470	99,89338	0,56057	0,14784	99,98667	1,30168	0,00824	100,14686
	Step 20	1,20251	0,00777	99,76065	0,70867	0,17697	99,62534	1,88669	0,24093	100,54209	0,68827	0,03223	99,95691	0,19172	0,15389	99,82499	1,37305	0,26737	100,23623
	Step 21	NaN	NaN	NaN	NaN	NaN	NaN	NaN	NaN	NaN	NaN	NaN	NaN	NaN	NaN	NaN	NaN	NaN	NaN

TABLE A.5: RAW AND CALIBRATED DATA OF Z AXIS IN COMPRESSION

		Z-axis in Compression Raw Data Cycle 1			Z-axis in Compression Raw Data Cycle 2			Z-axis in Compression Raw Data Cycle 3			-axis in Compression Calibrated Data Cycle			-axis in Compression Calibrated Data Cycle			-axis in Compression Calibrated Data Cycle		
start	0	0	0	0	0	0	0	0	0	0	0	0	0	0	0	0	0	0	0
increment	Step 1	1,82294	0,75804	100,28583	2,19516	1,14518	100,24086	2,89035	3,61010	100,36484	1,30773	0,73385	100,48135	1,68142	1,12108	100,43499	2,37388	3,58970	100,38664
	Step 2	0,31969	0,13746	99,86578	1,08675	0,50303	100,12951	1,69250	0,11038	100,11594	0,20074	0,11500	100,06829	0,56860	0,47977	100,32870	1,17904	0,08514	100,17645
	Step 3	0,45283	0,02224	99,74562	0,47130	0,27466	99,84155	0,87387	0,07159	100,11815	0,06577	0,04526	99,94659	0,04844	0,25219	100,04344	0,35561	0,04786	100,21925
	Step 4	0,52004	0,07540	99,79079	0,37667	0,23154	99,79001	0,66922	0,23139	99,81609	0,00136	0,05244	99,99170	0,14326	0,20918	99,99228	0,15091	0,20846	99,98352
	Step 5	0,35855	0,05186	99,78930	0,42323	0,23039	99,89301	0,66474	0,04016	99,79096	0,16103	0,02917	99,99118	0,09696	0,20792	100,09518	0,14702	0,01685	99,96982
	Step 6	0,46394	0,03312	99,76005	0,48998	0,10571	99,89554	0,60158	0,09638	99,79605	0,05481	0,01019	99,96114	0,02951	0,08285	100,09694	0,08331	0,07330	99,98460
	Step 7	0,48298	0,00464	99,77088	0,50943	0,13737	99,82050	0,74534	0,00490	99,81047	0,03562	0,02769	99,97176	0,00963	0,11455	100,02171	0,22811	0,02847	99,98697
	Step 8	0,46234	0,03430	99,80692	0,48895	0,09697	99,83767	0,61608	0,08084	99,85176	0,05667	0,01136	100,00811	0,03022	0,07410	100,03893	0,09764	0,05769	100,02629
	Step 9	0,46948	0,03119	99,81242	0,47538	0,18484	99,84651	0,61022	0,09136	99,83196	0,04951	0,00823	100,01357	0,04413	0,16218	100,04813	0,09182	0,06824	100,01843
	Step 10	0,49306	0,02627	99,76787	0,51828	0,05632	99,78444	0,58622	0,07362	99,77396	0,02554	0,00326	99,96877	0,00033	0,03333	99,98530	0,06802	0,05052	99,97606
Highest	Step 11	0,49589	0,04926	99,77811	0,50073	0,13204	99,77223	0,61089	0,02293	99,79083	0,02280	0,02630	99,97908	0,01811	0,10924	99,97338	0,09288	0,00032	99,97230
	Step 12	0,51179	0,00904	99,81239	0,55826	0,10569	99,82848	0,69335	0,02241	99,82514	0,00689	0,01405	100,01321	0,03953	0,08271	100,02931	0,17566	0,00101	99,98976
descent	Step 13	0,53124	0,00635	99,83230	0,46220	0,17674	99,86561	0,68876	0,03967	99,86447	0,01262	0,02951	100,03300	0,05748	0,15408	100,06733	0,17080	0,01629	100,04692
	Step 14	0,60970	0,09459	99,83462	0,57052	0,10666	99,82915	0,68322	0,13498	99,90037	0,09128	0,07148	100,03510	0,05186	0,08366	100,02990	0,16479	0,11180	100,07394
	Step 15	0,51686	0,04769	99,84105	0,49019	0,23295	99,89210	0,75876	0,07547	99,87710	0,00203	0,02466	100,04201	0,02960	0,21035	100,09385	0,24105	0,05203	100,06248
	Step 16	0,65991	0,05837	99,80543	0,42419	0,26900	99,85044	0,66589	0,05519	99,85268	0,14203	0,03510	100,00543	0,09587	0,24661	100,05263	0,14781	0,03189	100,02221
	Step 17	0,36650	0,09114	99,91073	0,53481	0,24589	99,89156	0,83717	0,05223	99,92234	0,15377	0,06849	100,11291	0,01525	0,22323	100,09306	0,31976	0,02857	100,08498
	Step 18	0,45647	0,00472	99,95522	0,48456	0,34225	99,95766	1,09658	0,05883	100,02425	0,06325	0,02776	100,15665	0,03588	0,31988	100,15989	0,58017	0,03467	100,09892
	Step 19	1,06593	0,01921	100,12417	1,31403	0,38175	100,08187	1,80917	0,30171	100,08502	0,54900	0,04350	100,32201	0,79780	0,35781	100,27916	1,29609	0,27665	100,19926
	Step 20	1,41254	0,12538	100,11284	2,19945	0,84603	100,40392	3,41344	0,14771	100,98497	0,89738	0,10071	100,30885	1,68565	0,82126	100,59753	2,90638	0,17703	101,00842
	Step 21	NaN	NaN	NaN	NaN	NaN	NaN	NaN	NaN	NaN	NaN	NaN	NaN	NaN	NaN	NaN	NaN	NaN	NaN

APPENDIX B

NOISE FILTERING BY 4TH ORDER RUNGE-KUTTA METHOD

```
clc
clear all
load data.dat
inp=data(:,3);
for i=1:8
wc=34;
dr=0.7;
dt=data(2,1)-data(1,1);
[filt]=filt2n(inp,wc,dr,dt);

function [filtered_u_open2]=filt2n(inp,wc,dr,dt)
ui=squeeze(inp')';
u = ui;

nmax=size(u,1);
sB4(1,1)=u(1);
sB4(1,2)=u(2);
for t=1:nmax-1
k1(1)=sB4(t,2);
   k1(2)=(2*pi*wc)^2*u(t)-4*dr*pi*wc*sB4(t,2)-(2*pi*wc)^2*sB4(t,1);
k2(1)=(sB4(t,2)+0.5*k1(2)*dt);
   k2(2)=(2*pi*wc)^2*u(t)-4*dr*pi*wc*(sB4(t,2)+0.5*k1(2)*dt)-...
      (2*pi*wc)^2*(sB4(t,1)+0.5*k1(1)*dt);
   k3(1)=(sB4(t,2)+0.5*k2(2)*dt);
   k3(2)=(2*pi*wc)^2*u(t)-4*dr*pi*wc*(sB4(t,2)+0.5*k2(2)*dt)-...
      (2*pi*wc)^2*(sB4(t,1)+0.5*k2(1)*dt);
k4(1)=(sB4(t,2)+k3(2)*dt);
   k4(2)=(2*pi*wc)^2*u(t)-4*dr*pi*wc*(sB4(t,2)+k3(2)*dt)-...
      (2*pi*wc)^2*(sB4(t,1)+k3(1)*dt);
   sB4(t+1,1)=sB4(t,1)+(k1(1)+2*k2(1)+2*k3(1)+k4(1))/6*dt;
   sB4(t+1,2)=sB4(t,2)+(k1(2)+2*k2(2)+2*k3(2)+k4(2))/6*dt;
end

filtered_u_open1=sB4(:,1);


u=filtered_u_open1(end:-1:1);

nmax=size(u,1);
sB4(1,1)=u(1);
```

```
sB4(1,2)=u(2);
for t=1:nmax-1
k1(1)=sB4(t,2);
   k1(2)=(2*pi*wc)^2*u(t)-4*dr*pi*wc*sB4(t,2)-(2*pi*wc)^2*sB4(t,1);
k2(1)=(sB4(t,2)+0.5*k1(2)*dt);
   k2(2)=(2*pi*wc)^2*u(t)-4*dr*pi*wc*(sB4(t,2)+0.5*k1(2)*dt)-...
      (2*pi*wc)^2*(sB4(t,1)+0.5*k1(1)*dt);
   k3(1)=(sB4(t,2)+0.5*k2(2)*dt);
   k3(2)=(2*pi*wc)^2*u(t)-4*dr*pi*wc*(sB4(t,2)+0.5*k2(2)*dt)-...
      (2*pi*wc)^2*(sB4(t,1)+0.5*k2(1)*dt);
k4(1)=(sB4(t,2)+k3(2)*dt);
   k4(2)=(2*pi*wc)^2*u(t)-4*dr*pi*wc*(sB4(t,2)+k3(2)*dt)-...
      (2*pi*wc)^2*(sB4(t,1)+k3(1)*dt);
   sB4(t+1,1)=sB4(t,1)+(k1(1)+2*k2(1)+2*k3(1)+k4(1))/6*dt;
   sB4(t+1,2)=sB4(t,2)+(k1(2)+2*k2(2)+2*k3(2)+k4(2))/6*dt;
end
filtered_u_open_inversed=sB4(:,1);
filtered_u_open2=filtered_u_open_inversed(end:-1:1);
```